FlowBench: Benchmarking Optical Flow Estimation Methods for Reliability and Generalization

Anonymous authors
Paper under double-blind review

Abstract

Optical flow estimation is a crucial computer vision task often applied to safety-critical real-world scenarios like autonomous driving and medical imaging. While optical flow estimation accuracy has greatly benefited from the emergence of deep learning, learning-based methods are also known for their lack of generalization and reliability. However, reliability is paramount when optical flow methods are employed in the real world, where safety is essential. Furthermore, a deeper understanding of the robustness and reliability of learning-based optical flow estimation methods is still lacking, hindering the research community from building methods safe for real-world deployment. Thus we propose FlowBench, a robustness benchmark and evaluation tool for learning-based optical flow methods. FlowBench facilitates streamlined research into the reliability of optical flow methods by benchmarking their robustness to adversarial attacks and out-of-distribution samples. With FlowBench, we benchmark 57 checkpoints across 3 datasets under 7 diverse adversarial attacks and 23 established common corruptions, making it the most comprehensive robustness analysis of optical flow methods to date. Across this wide range of methods, we consistently find that methods with state-of-the-art performance on established standard benchmarks lack reliability and generalization ability. Moreover, we find interesting correlations between the performance, reliability, and generalization ability of optical flow estimation methods, under various lenses such as design choices used, number of parameters, etc. The open-source code and weights for FlowBench is available in this anonymous GitHub repository.

1 Introduction

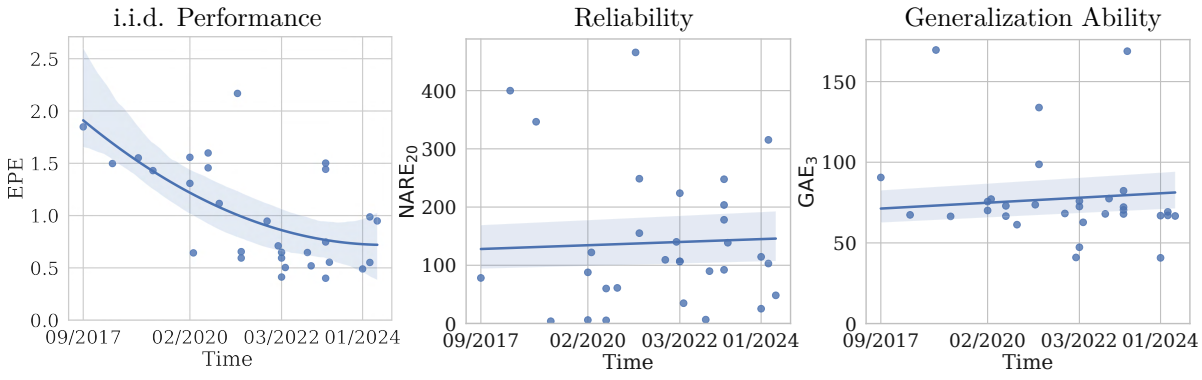

Figure 1: Optical flow estimation methods proposed over time and their reliability and generalization ability. In all three plots, the y-axis represents error, i.e., lower is better. The error of optical flow estimation methods on independent and identically distributed data samples (i.i.d.) has decreased over time, however, their reliability and generalization ability are stagnant if not deteriorating.

The recent growth of Deep Learning (DL) has greatly benefited computer vision, in particular when considering complex tasks such as the estimation of optical flow fields. In optical flow estimation, a method

is supposed to estimate the movement of every pixel between at least two consecutive image frames in a subpixel-accurate manner. This task was earlier performed using model-driven approaches such as Horn & Schunck (1981) and Lucas & Kanade (1981). However, these methods have severe limitations leading to sub-optimal estimations and, consequently, to the predominant use of DL to perform the estimations (Dosovitskiy et al., 2015; Ilg et al., 2017; Jahedi et al., 2024b). The performance of learning-based optical flow estimation methods has improved over the years on independent and identically distributed data samples (i.i.d.), leading to lower validation errors as shown by Fig. 1 (left). At the same time, DL-based methods are known to be unreliable (Geirhos et al., 2018; Prasad, 2022), they tend to learn shortcuts rather than meaningful feature representations (Geirhos et al., 2020), and can be easily deteriorated even by small corruptions. This can become a practical threat, as optical flow estimation is highly relevant in safety-critical applications such as autonomous driving (Capito et al., 2020; Wang et al., 2021), robotic surgery (Rosa et al., 2019) and others. Thus, before deploying DL-based optical flow estimation methods, assessing their vulnerability and generalization ability is of paramount importance. We observe in Fig. 1 that over the years, despite improvement in the performance of learning-based optical flow estimation methods on i.i.d. samples, their reliability under adversarial attacks and generalization ability to distribution shifts are almost unchanged, and far from the performance on i.i.d. sample. Had recent research focused on these factors, the newly proposed methods could have been more reliable and ready for practical use. Our proposed FlowBench facilitates this study, streamlining it for future research to utilize.

Many works have highlighted the importance of such a study by reducing model vulnerability (Xu et al., 2021b; Croce et al., 2023; Agnihotri et al., 2023; Schrodi et al., 2022; Tran et al., 2022; Grabinski et al., 2022), showing that robustness does follow from high accuracy (Tsipras et al., 2019; Schmidt et al., 2018; Schmalfuss et al., 2022b) or improving generalization (Hendrycks et al., 2020; Hoffmann et al., 2021) for various downstream tasks such as image classification, semantic segmentation, image restoration and others. To facilitate this research, robustness benchmarking tools and benchmarks like Croce et al. (2021); Jung et al. (2023); Tang et al. (2021) have been proposed for image classification models. They look into the adversarial and Out-of-Distribution (OOD) robustness of DL models. However, these works are limited to image classification. A similar benchmarking tool and comprehensive benchmark for optical flow is amiss.

To bridge this gap, we propose FlowBench that facilitates robustness evaluations of optical flow models against adversarial attacks and image corruptions for OOD data and provides a unified evaluation scheme and streamlined code. We use white-box adversarial attacks constrained under a Lipchitz continuity bound, to test the stability of an optical flow model's predictions to very small perturbations optimized with malicious intentions. This allows for testing the reliability of the model's predictions. Additionally, FlowBench enables perturbing the input images with unseen synthetic corruptions, which allows to test for testing the generalization abilities of the optical flow models to distribution shifts. Using FlowBench, we benchmark 57 model checkpoints over 3 commonly used optical flow estimation datasets. These model checkpoints include SotA optical flow estimation methods and evaluation methods, including SotA adversarial attacks and image corruption methods. FlowBench is easy to use, and new methods, datasets, metrics, and evaluations, when proposed, can be easily integrated to benchmark their performance. This will help researchers build better models that are not limited to improved performance on identical and independently distributed (i.i.d.) samples and are less vulnerable to adversarial attacks while generalizing better to image corruptions.

The main contributions of this work are as follows:

- We provide FlowBench, a benchmarking tool to evaluate the performance of DL-based optical flow estimation methods over different datasets and make 90 checkpoints over different datasets publicly available for streamlined benchmarking while enabling the research community to add further checkpoints.
- We benchmark 57 of the aforementioned model checkpoints against SotA and other commonly used adversarial attacks and common corruptions that can be easily queried using FlowBench.
- We perform an in-depth analysis using FlowBench, showing that methods that are SotA on i.i.d. are remarkably less reliable and generalize worse than other non-SotA methods.

- We analyze correlations between performance, reliability, and generalization abilities of optical flow methods, under various lenses such as design choices, and the number of learnable parameters.
- We show that the optimization of white-box adversarial attacks for optical flow estimation can be performed without the availability of ground truth predictions, furthering the study of their reliability.

2 Related Work

FlowBench is the first robustness benchmarking tool and benchmark for optical flow estimation methods that unifies adversarial and OOD robustness, taking inspiration from robustness benchmarks for other vision tasks such as image classification. While several previous works provide benchmarking tools for optical flow estimation, they only facilitate benchmarking of either adversarial or OOD robustness and are less comprehensive than FlowBench. FlowBench leverages the individual strengths of prior benchmarking tools, but casts them into a unified and easy-to-use robustness benchmark. Following, we discuss these related works in detail.

2.1 Robustness Benchmarking For Image Classification Methods

Goodfellow et al. (2015) proposed the Fast Gradient Sign Method (FGSM) attack which gave rise to the domain of adversarial attacks on image classification. Complementing adversarial attacks, Hendrycks & Dietterich (2019) proposed 2D Common Corruptions for image classification tasks on the CIFAR-100 (Krizhevsky et al., 2009) and ImageNet-1k (Russakovsky et al., 2015) datasets and their variants. Since then, most adversarial attacks and OOD Robustness works have focused on image classification tasks, warranting a consolidated benchmarking tool and benchmark for robustness. In the case of image classification, this gap was filled by multiple works such as RobustBench (Croce et al., 2021) and RobustArts (Tang et al., 2021). Both works make multiple image classification model checkpoints publicly available, including checkpoints trained for improved robustness. Moreover, RobustBench is a benchmarking tool that facilitates evaluating both adversarial and OOD robustness of image classification models. Other similar benchmarking tools exist, like DeepFool (Moosavi-Dezfooli et al., 2016), Torchattacks (Kim, 2020), and Foolbox (Rauber et al., 2020). Yet, these are merely benchmarking tools and do not provide a comprehensive benchmark - they only facilitate evaluating adversarial robustness but not the OOD robustness of the method. As of now, no benchmarking tool or benchmark exists for optical flow estimation methods' robustness evaluations. Thus, we propose FlowBench which enables benchmarking adversarial and OOD robustness and makes a multitude of model checkpoints available, providing the research community with the much needed tools.

2.2 Benchmarking Optical Flow Estimation Methods

Optical flow estimation has been a problem attempted to be solved for a long time. Over time multiple works have been proposed to streamline research in this direction by providing benchmarking libraries for i.i.d. performance of proposed methods. Such libraries include *mmflow* (Contributors, 2021), *ptlflow* (Morimitsu, 2021), and *Spring* (Mehl et al., 2023). These libraries also provide model checkpoints to facilitate evaluations. *Spring*, also provides a benchmark but the performance evaluations are limited to their proposed Spring dataset. Whereas, both *mmflow* and *ptlflow* do not provide a robustness benchmark but enable benchmarking on multiple optical flow datasets such as FlyingThings3D (Mayer et al., 2016), KITTI2015 (Menze & Geiger, 2015) and MPI Sintel (Butler et al., 2012). Most importantly, the evaluation abilities of these benchmarking tools are limited to i.i.d. data. Thus, we built FlowBench, using *ptlflow* and publicly available model checkpoints to extend method evaluations to adversarial and OOD Robustness, consolidating research towards reliability and generalization ability of optical flow estimation methods. Additionally, FlowBench is the first to provide a comprehensive benchmark on existing optical flow estimation methods over 3 datasets and multiple adversarial attacks and image corruptions. Please note, FlowBench enables evaluations of methods on synthetic corruptions. Agnihotri et al. (2025) show in their work that synthetic corruptions can serve as a reliable proxy for real-world corruptions. However, they additionally discuss that the synthetic corruptions do not accurately represent most real-world corruptions and challenging scenarios.

Thus, to cover such scenarios, we require new datasets, like those proposed by Janai et al. (2017). In this work, we focus on datasets for which we could obtain pretrained checkpoints, and thus do not consider Janai et al. (2017). We anticipate the community to benchmark new methods, trained on new datasets using the open-source FlowBench benchmarking tool.

2.3 Adversarial Attacks

As discussed in Sec. 1, DL models tend to learn shortcuts to map data samples from input to target distribution (Geirhos et al., 2020), leading to the model learning inefficient feature representations. In their work, Goodfellow et al. (2015) showed that this inefficient learning of feature representations can be easily exploited. Goodfellow et al. (2015) added noise to the input data samples which was optimized to increase loss using model information, such that the model was fooled into making incorrect predictions. This demonstrated the vulnerability and unreliability of model predictions as the perturbed input samples still appeared semantically similar to the human eye. They named this attack the Fast Sign Gradient Method (FGSM). This attack led to an increased interest by the research community to better optimize the noise inspiring multiple other works such as Basic Iteration method (BIM) (Kurakin et al., 2018), Projected Gradient Descent (PGD) (Kurakin et al., 2017), Auto-PGD (APGD) (Wong et al., 2020) and CosPGD (Agnihotri et al., 2024) which were direct extensions to FGSM, and other attacks such as Perturbation-Constrained Flow Attack (PCFA) (Schmalfuss et al., 2022b) and Adversarial Weather (Schmalfuss et al., 2023), which are indirect extensions of FGSM.

3 Considered Optical Flow Estimation Methods

Given two consecutive image frames I_t and I_{t+1}, the goal of optical flow estimation is to predict a dense motion field $\overrightarrow{f} : \Omega \to \mathbb{R}^2$, where Ω is the image domain and $\overrightarrow{f}(x, y) = (u, v)^\top$ indicates the sub-pixel accurate horizontal and vertical displacement of the pixel of I_t at location $(x, y) \in \Omega$ to the same point in I_{t+1}, i.e. for non-occluded pixels, $I_t(x, y) = I_{t+1}(x + u, y + v)$. For our analysis, we consider a variety of different methods for which model checkpoints were available. While our benchmark will be continuously extended, our goal is to provide a reasonable coverage across different modes such as to allow for an analysis of properties that are shared between more reliable and generalizable approaches.

While DL-based optical flow estimation methods differ in diverse ways, for example, w.r.t. the model architecture, point matching mechanism or training data, we attempt to structure our analysis by grouping existing models according to their core architecture. We identify four model families, each inspired by one seminal work: FlowNet (Dosovitskiy et al., 2015), PWC-Net (Pyramid, Wrapping, and Cost Volume) (Sun et al., 2018), RAFT (Teed & Deng, 2020), and FlowFormer (Huang et al., 2022). Considering each model in the context of other models with similar working mechanisms allows to better analyze key differences that render a model more reliable. In the following, we briefly discuss the properties of different considered models (please refer to Appendix B for more details). Please also note that there exist obvious similarities of methods across families as discussed in Appendix B, such that there remains some ambiguity regarding their grouping. The following summary should therefore not be understood as a taxonomy but it merely provides a coarse understanding of commonalities across approaches. Overall, we provide evaluations for 57 model checkpoints, including the following, diverse, approaches.

3.1 FlowNet Family

Dosovitskiy et al. (2015) proposed the first end-to-end differentiable DL-based architectures for optical flow estimation, termed *FlowNets*, building on UNet-like architectures. Several works were inspired by FlowNet, and introduced various modifications. Ilg et al. (2017) introduce *FlowNet2.0* that uses a stacked FlowNet architecture including an iterative flow refinement using image warping, and improves the schedule of training data. Many later works follow this schedule.

Compared to FlowNet2.0, *LiteFlowNet* (Hui et al., 2018) introduces a more effective flow inference approach at each pyramid level through a lightweight cascaded network. A flow regularization layer ameliorates the issue of outliers and vague flow boundaries, and feature warping is used instead of image warping.

LiteFlowNet2 (Hui et al., 2020) further improves accuracy and latency by making minor architectural changes to the LiteFlowNet architecture and training schedule. *LiteFlowNet3* (Hui & Loy, 2020) further improve upon the LiteFlowNet2.0 by alleviating the issue of outliers in the cost volume. They amend each cost vector using an adaptive modulation before the flow decoding and replace each potentially inaccurately predicted optical flow with an accurate one from a near position through a warping of the flow field.

3.2 PWC-Net Family

PWC-Net (Sun et al., 2018) and FlowNets share concepts such as employing multi-scale features, warping, and the usage of a cost volume. Both are based on CNN architectures. However, PWC-Net uses the warped features to construct a cost volume at every scale, significantly outperforming FlowNet2.0 on established benchmarks like KITTI2015 (Menze & Geiger, 2015) and MPI Sintel (Butler et al., 2012). *FastFlowNet* (Kong et al., 2021) replaces the dual convolution feature pyramid in PWC-Net with the head-enhanced pooling pyramid (HEPP) for high-resolution pyramid features and reduced model size. A center dense dilated correlation layer (MFC) for constructs a compact cost volume while keeping a large search radius. *DICL* (Wang et al., 2020) introduces displacement-invariant cost learning. The same 2D convolution-based matching net is applied independently on each 2D displacement hypothesis to learn a 4D cost volume and avoid learning a 5D feature volume. *HD3* (Yin et al., 2019) adapts a PWC-Net-like architecture to learn probabilistic pixel correspondences in both optical flow and stereo matching using a pyramid feature extractor with ImageNet1k (Russakovsky et al., 2015)-pre-trained weights. HD3 estimates local matching distributions at each scale conditioned on the matching and warping at coarser scales. *IRR* (Hur & Roth, 2019) take inspiration from classical energy minimization approaches and residual networks to propose an iterative residual refinement. IRR can be combined with both FlowNets and PWC-Net. In our evaluation, we consider their adaptation to PWC-Net because it has better i.i.d. performance.

ScopeFlow (Bar-Haim & Wolf, 2020) improves upon IRR-PWC-Net by improving the data sampling process while testing the regularization and augmentations used to mitigate the bias induced by the training protocols. In *MaskFlowNet*, Zhao et al. (2020) propose an Occlusion-Aware Feature Matching Module (OFMM) and an Asymmetric Occlusion-Aware Feature Matching Module (AsymOFMM) in PWC-Net, to overcome the ambiguity caused due to occlusions. *MaskFlowNetS* (Zhao et al., 2020) was proposed as the first stage of MaskFlowNet, and inherits the network architecture from PWC-Net, but replaces the feature matching modules (FMMs) by AsymOFMMs. *VCN* (Yang & Ramanan, 2019) address the 4D cost volume used by variants of the PWC family by proposing volumetric encoder-decoder architectures that efficiently capture large receptive fields, multi-channel cost volumes that capture multi-dimensional notions of pixel similarities, and separable volumetric filtering that significantly reduces computation and parameters.

3.3 RAFT Family

Teed & Deng (2020) proposed Recurrent All-Pairs Field Transforms (RAFT) to extract per-pixel features and build a multi-scale 4D correlation volume for all pairs of pixels. A recurrent unit is used to perform look-ups on these correlation volumes. The original RAFT uses additional data and fine-tuning compared to FlowNet2.0. *CCMR* (Jahedi et al., 2024a) propose adapting RAFT to use attention-based motion grouping concepts for multi-scale optical flow estimation. CCMR first computes global multi-scale context features and then uses them to guide the actual motion grouping. While iterating both steps over all coarse-to-fine scales, they adapt cross-covariance image transformers to allow for an efficient realization while maintaining scale-dependent properties. *CRAFT* (Sui et al., 2022) inherits the flow estimation pipeline of RAFT and revitalizes the correlation volume with two proposed components: a Semantic Smoothing Transformer on the features from the second frame, and a Cross-Frame Attention Layer to compute the correlation volume. Both components are intended to suppress spurious correlations in the correlation volume. *CSFlow* (Shi et al., 2022) adapts the multi-layer GRU to optical flow. It further proposes a *Cross Strip Correlation module (CSC)* to encode global context into correlation volumes and a *Correlation Regression Initialization module (CRI)*. *Flow1D* (Xu et al., 2021a) proposes 1D attention and correlation operations to compute 3D cost volumes for optical flow regression, where they adopt RAFT's framework to estimate the optical flow iteratively.

GMA (Jiang et al., 2021a) adapts a RAFT architecture to include their proposed global motion aggregation (GMA) module, a transformer-based approach to find long-range dependencies between pixels. This modified RAFT architecture with a GMA further inspired other optical flow approaches. *GMFlow* (Xu et al., 2022) identifies correspondences in image pairs using feature similarities. They use transformer-based modules to enhance extracted features, followed by self-attention modules for feature matching and flow propagation. Their feature extraction and feature upsampling modules are identical to RAFT. *GMFlowNet* (Zhao et al., 2022) adopts the iterative update operator of RAFT as the optimization step. They propose patch-based overlapping attention (POLA) instead of multi-headed self-attention of transformer blocks to extract large context features to improve the matching step. *LCV* (Khairi et al., 2024) proposes a lightweight module for learnable cost volume that adds onto RAFT. *LLA-Flow* (Xu et al., 2023b) proposes local similarity aggregation for 4D cost volumes and presents lightweight operations to diminish the impact of outliers caused by lack of texture within RAFT. *MS-RAFT+* (Jahedi et al., 2024b) adapts RAFT for combining hierarchical concepts at multiple scales. It builds on top of MS-RAFT by exploiting an additional finer scale.

MatchFlow (Dong et al., 2023) proposes a new feature matching extractor (FME) to be used with RAFT and GMA module. *SCV* (Jiang et al., 2021b) adapts RAFT to use a sparse correlation volume instead of a dense one. *SeparableFlow* (Zhang et al., 2021) proposes a separable cost volume module, a drop-in replacement to RAFT's correlation cost volumes, that uses non-local aggregation layers to exploit global context cues and prior knowledge, to disambiguate motions. *SKFlow* (Sun et al., 2022) uses Super Kernels that allow for larger receptive fields allowing it to recover occluded motions. They use the non-local GMA module from GMA for optical flow estimations. *RapidFlow* (Morimitsu et al., 2024a) propose a recurrent feature encoder that uses a single shared block with efficient 1D layers (NeXt1D) to generate feature pyramids of variable levels. Their decoder is similar to RAFT, with a few changes inspired by SKFLow (Sun et al., 2022). *RPKNet* (Morimitsu et al., 2024b) adapts RAFT to use their proposed Partial Kernel Convolution (PKConv) layers and Separable Large kernels (SLK). PKConv is used to produce variable multi-scale features with a single shared block, while SLK is used to capture large context information with low computational cost. *SplatFlow* (Wang et al., 2024) uses splatting for feature matching in architectures like RAFT and GMA. As SplatFlow is proposed as multi-frame optical flow estimation method, it requires three frames at a time for training as opposed to the two frames used by RAFT and GMA. *VideoFlow* (Shi et al., 2023a) proposes a multi-frame optical flow estimation method with an iterative flow refinement module using SKBlocks from SKFlow. For feature extractors, they take inspiration from FlowFormer (Huang et al., 2022) and use ImageNet1k pre-trained Twins-SVT (Chu et al., 2021). They use three and five-image frames during training. *NeuFlow* (Zhang et al., 2024) is inspired by GMFlow and uses transformer-based blocks to implement global cross-attention. They use a very similar upsampling module as GMFlow and RAFT. However, to obtain feature maps with finer details, they directly extract features from the original images using a CNN block, instead of using features for matching at the $\frac{1}{16}^{\text{th}}$ and $\frac{1}{8}^{\text{th}}$ scale like RAFT and GMFlow.

3.4 FlowFormer Family

FlowFormer (Huang et al., 2022) is a transformer-based neural network architecture for optical flow estimation. It tokenizes the 4D cost volume, encodes the cost tokens into a cost memory with alternate group transformer (AGT) layers in a latent space, and decodes the cost memory via a recurrent transformer decoder with dynamic positional cost queries. The two-stage Twins-SVT (Chu et al., 2021) feature extractor is pre-trained on the ImageNet1k dataset. After that, the training procedure of the entire FlowFormer is similar to RAFT's training procedure. *FlowFormer++* (Shi et al., 2023b) is built upon FlowFormer and includes Masked Cost Volume Autoencoding (MCVA). They pre-train the cost-volume encoder with a mask encoding strategy.

DIP (Zheng et al., 2022) and StarFlow (Godet et al., 2021) have significantly different architectures than the above summarized models. We therefore consider them separately in our analysis.

4 FlowBench Usage

In the following, we describe the benchmarking tool, FlowBench. It is built using pltflow (Morimitsu, 2021), and supports 37 unique architectures, for example, RAFT, FlowFormer, FlowFormer++, CCMR, anmd

others (new architectures added to ptlflow over time are compatible with FlowBench) and distinct datasets, namely FlyingThings3D (Mayer et al., 2016), KITTI2015 (Menze & Geiger, 2015), MPI Sintel (Butler et al., 2012) (clean and final) and Spring (Mehl et al., 2023) datasets (please refer Appendix C for additional details on the datasets). It enables training and evaluations on all aforementioned datasets including evaluations using SotA adversarial attacks such as CosPGD (Agnihotri et al., 2024) and PCFA (Schmalfuss et al., 2022b), Adversarial weather (Schmalfuss et al., 2023), and other commonly used adversarial attacks like BIM (Kurakin et al., 2018), PGD (Kurakin et al., 2017), FGSM (Goodfellow et al., 2015), under various Lipshitz (l_p) norm bounds. Additionally, it enables evaluations for Out-of-Distribution (OOD) robustness by corrupting the inference samples using 2D Common Corruptions (Hendrycks & Dietterich, 2019) and 3D Common Corruptions (Kar et al., 2022).

We follow the nomenclature set by RobustBench (Croce et al., 2021) and use "threat_model" to define the kind of evaluation to be performed. When "threat_model" is defined to be "None", the evaluation is performed on unperturbed and unaltered images, if the "threat_model" is defined to be an adversarial attack, for example "PGD", "CosPGD" or "PCFA", then FlowBench performs an adversarial attack using the user-defined parameters. We elaborate on this in Appendix E.1. Whereas, if "threat_model" is defined to be "2DCommonCorruptions" or "3DCommonCorruptions", the FlowBench performs evaluations after perturbing the images with 2D Common Corruptions and 3D Common Corruptions, respectively. We elaborate on this in Appendix E.2. If the queried evaluation already exists in the benchmark provided by this work, then FlowBench simply retrieves the evaluations, thus saving computation.

FlowBench enables the use of all the attacks mentioned in Sec. 2.3 to help users better study the reliability of their optical flow methods. We choose to specifically include these white-box adversarial attacks as they either serve as the common benchmark for adversarial attacks in classification literature (FGSM, BIM, PGD, APGD) or they are unique attacks proposed specifically for pixel-wise prediction tasks (CosPGD) and optical flow estimation (PCFA and Adversarial Weather). These attacks can either be *Non-targeted*, which are designed to simply fool the model into making incorrect predictions, irrespective of what the model eventually predicts, or can be *Targeted*, where the model is fooled to make a certain prediction. Most attacks can be designed to be either Targeted or Non-targeted, these include FGSM, BIM, PGD, APGD, CosPGD, and Adversarial Weather. However, by design, some attacks are limited to being only one of the two, for example, PCFA which is a targeted attack.

In the following we show the basic commands to use FlowBench. We describe each attack and common corruption supported by FlowBench in detail in Appendix E. Please refer to Appendix G for details on the arguments and function calls.

4.1 Model Zoo

It is a challenge to find all checkpoints, while training them is a time and compute exhaustive process. Thus, we gather available model checkpoints from various sources such as ptlflow (Morimitsu, 2021) and mmflow (Contributors, 2021). The trained checkpoints for all models available in FlowBench can be obtained using the following lines of code:

```
from flowbench.evals import load_model
model = load_model(model_name='RAFT', dataset='KITTI2015')
```

Each model checkpoint can be retrieved with the pair of 'model_name', the name of the model, and 'dataset', the dataset for which the checkpoint was last finetuned. In Appendix F we provide a complete overview of all the 90 available pairs of model checkpoints and datasets. Please note, we used checkpoints trained on KITTI 2015 and MPI Sintel for the benchmarking in this work, thus using 57 available pairs (or methods + checkpoints).

4.2 Adversarial Attacks

FlowBench can be used to evaluate models on the discussed adversarial attacks using the following lines of code (please refer Appendix G.1 for details regarding the arguments):

```
from flowbench.evals import evaluate
model, results = evaluate(model_name='RAFT', dataset='KITTI2015',
                    threat_model='CosPGD', iterations=20, alpha=0.01,
                    epsilon=8/255, lp_norm='Linf', targeted=True,
                    optim_wrt='ground_truth', retrieve_existing=True)
```

4.3 OOD Robustness

FlowBench can be used to evaluate models on the 2D and 3D Common Corruptions using the following lines of code, following is an example for the latter (please refer Appendix G.3 (2D Common Corruptions) and Appendix G.4 (3D Common Corruption) for details regarding the arguments):

```
from flowbench.evals import evaluate
model, results = evaluate(model_name='RAFT', dataset='KITTI2015',
                  threat_model='3DCommonCorruption',
                  severity=3, retrieve_existing=True)
```

5 Metrics For Analysis At Scale

Analysis of optical flow estimation methods at the same scale as this work, especially under the lens of reliability and generalization ability has not been attempted before. FlowBench returns evaluations using common metrics. The most commonly (Schrodi et al., 2022; Schmalfuss et al., 2022a; Agnihotri et al., 2024; Dosovitskiy et al., 2015; Teed & Deng, 2020; Ilg et al., 2017; Huang et al., 2022) used metric for evaluating the performance of a method is the mean End-Point-Error (EPE), the mean Euclidean distance between the predicted optical flow $\overrightarrow{f}$ and the ground truth $\overrightarrow{f}_{\text{gt}}$ for all pairs of frames in a given dataset, where lower is better. Additionally, FlowBench also returns 1-px error, 3-px error, 5-px error, and cosine distance between two vectors (see Appendix D for details). The users are free to use one or more metrics for analysis.

However, any single evaluation does not reflect the reliability and generalization ability of a method. Moreover, this work has performed over 4500 experiments in total, such that individual EPE comparison is hardly interpretable. Thus, we aggregate evaluations in our proposed metrics, the Reliability Error and Generalization Ability Error. For reliability and generalization, we look at the maximum possible value of mean EPE across attacks over multiple datasets. That is, we ask the question "What is the worst possible performance of a given method?". An answer to this question tells us about the reliability and generalization ability of a method. In the following, we describe the measures for different scenarios in detail.

5.1 Generalization Ability Error

Inspired by multiple works (Croce et al., 2021; Hendrycks et al., 2020; Hoffmann et al., 2021) that use OOD Robustness of methods for evaluating the generalization ability of the method, we evaluate over every common corruption, that is 2D Common Corruptions and 3D Common Corruptions combined. Then, we find the maximum of the mean EPE w.r.t. the ground truth for a given method, across all corruptions at a given severity and report this as Generalization Ability Error denoted by $\text{GAE}_{severity\ level}$. For example, for severity 3, the measure would be denoted by GAE_3. The less the GAE value, the better the generalization ability of the given optical flow estimation method. These corruptions perturb the images to cause distributions and domain shifts, such shifts often confuse the methods into making incorrect predictions.

For calculating GAE, we use all 15 2D Common Corruptions: 'Gaussian Noise', Shot Noise', 'Impulse Noise', 'Defocus Blur', 'Frosted Glass Blur', 'Motion Blur', 'Zoom Blur', 'Snow', 'Frost', 'Fog', 'Brightness', 'Contrast', 'Elastic Transform', 'Pixelate', 'JPEG Compression', and eight 3D Common Corruptions: 'Color Quantization', 'Far Focus', 'Fog 3D', 'ISO Noise', 'Low Light', 'Near Focus', 'XY Motion Blur', and 'Z Motion Blur'. All the common corruptions are at severity 3. Kar et al. (2022) offers more 3D Common Corruptions, however computing them is resource intensive. Thus, given our limited resources and an overlap in the corruptions between 2D Common Corruptions and 3D Common Corruptions, we focus on generating 3D Common Corruptions that might be unique from their 2D counterpart, require fewer sources to generate,

and are interesting from an optical flow estimation perspective. In Appendix A we show that these synthetic common corruptions can indeed be used as a proxy for possible corruptions when in the wild.

5.2 Reliability Error

An adversarial attack is a perturbation made on the input images to fool a method into changing its predictions while the input image looks semantically similar to a human observer. Most works that focus on the reliability of optical flow estimation methods perform adversarial attacks, however, these works either focus on targeted attacks or on non-targeted attacks, not both at the same time. The objective of targeted attacks is to optimally perturb the input image such that the method predictions are changed towards a specifically desired target, for example, a target can be a $\overrightarrow{0}$ flow i.e. attacking so that the flow prediction at all pixels should become zero. Conversely, non-targeted adversarial attacks do not intend to shift the method's predictions to a specific target, they simply intend to fool the method into making any incorrect predictions. To streamline research into the reliability of these methods, we perform both targeted and non-targeted attacks.

Non-Targeted Attacks. Given the ground truth optical flow field $\overrightarrow{f}_{\text{gt}}$, the objective of a non-targeted attack is to fool the optical flow estimation model into predicting a flow field $\overrightarrow{f}$, such as to maximize the EPE of $\overrightarrow{f}$ w.r.t. $\overrightarrow{f}_{\text{gt}}$. The notation for the metric measuring the EPE under non-targeted adversarial attack is $\text{NARE}_{\text{attack iterations}}$, where NARE stands for Non-targeted Attack Reliability Error, and the subscript indicates the number of attack iterations used for optimizing the attack. For example, when 20 attack iterations were used to optimize the attack, then the metric would be NARE_{20}. The higher the NARE value, the worse the reliability of the optical flow method.

Targeted Attacks. Here, the objective is to minimize the EPE of the predicted flow field $\overrightarrow{f}$ w.r.t. a given target flow field $\overrightarrow{f}_{\text{target}}$. In this work, we consider two targets, $\overrightarrow{0}$, where $\overrightarrow{0}(x,y) = (0,0)^\top \quad \forall (x,y)^\top \in \Omega$ and $\overrightarrow{-f}$, where $\overrightarrow{-f}(x,y) = -\overrightarrow{f_{\text{init}}}(x,y)^\top \quad \forall (x,y)^\top \in \Omega$, with $\overrightarrow{f_{\text{init}}}$ being the initial model prediction before the attack. Note that both targets can be computed without knowledge of $\overrightarrow{f}_{\text{gt}}$. We measure the EPE of $\overrightarrow{f}$ w.r.t. $\overrightarrow{f}_{\text{target}}$. However, to standardize notations, we report the negative EPE in this case, thus, the higher the value, the worse the performance of the optical flow estimation method. The notation for this metric is, $\text{TARE}^{\text{target}}_{\text{attack iterations}}$, where TARE stands for Targeted Attack Reliability Error and the superscript informs about the target used (zero vector or negative of the initial flow prediction) and the subscript informs about the number of attack iterations used for optimizing the attack. For example, when the target is $\overrightarrow{0}$ and 20 attack iterations were used to optimize the attack then the metric would be $\text{TARE}^{\overrightarrow{0}}_{20}$. The higher the TARE value, the worse is the reliability of the optical flow method.

For calculating TARE and NARE values we used BIM, PGD, and CosPGD attack with step size α=0.01, perturbation budget $\epsilon = \frac{8}{255}$ under the ℓ_∞-norm bound, as targeted and non-targeted attacks respectively. We use ℓ_∞-norm bound as we observe in Appendix H that there is a high correlation between the performance of optical flow estimation methods when attacked using ℓ_∞-norm bounded attacks and ℓ_2-norm bounded attacks. We use 20 attack iterations for calculating TARE and NARE as we observe in *Appendix H*, that at a lower number of iterations, the gap in performance of different optical flow estimation methods is small, thus an in-depth analysis would be difficult, and we do not go beyond 20 attack iterations as computing each attack step for an adversarial attack is very expensive, and as shown by (Agnihotri et al., 2024) and (Schmalfuss et al., 2022b), 20 iterations are enough to optimize an attack to truly understand the performance of the attacked method.

In Fig. 2, we visualize a few attack samples to demonstrate what the targets might look like, in case of targeted attacks, and how both attacks optimize the perturbations on the clean inputs to fool the model into predicting incorrect flow fields.

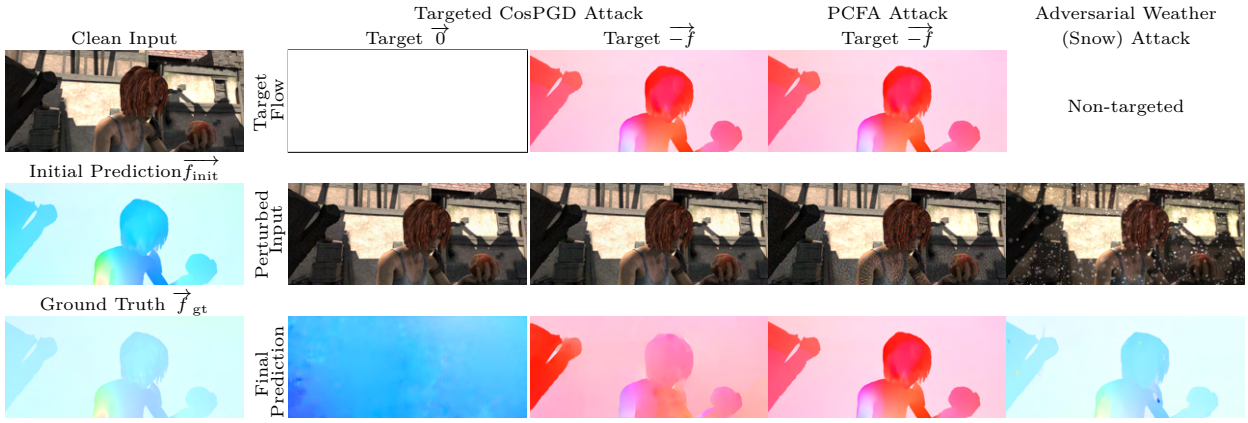

Figure 2: Examples of MPI Sintel images perturbed by adversarial attacks and the optical flow predictions using FlowFormer++. These examples are intended to show the versatility of FlowBench. Here, the first column shows the clean unperturbed input, initial flow prediction $\overrightarrow{f}_{\text{init}}$ and ground truth flow field $\overrightarrow{f}_{\text{gt}}$. The remaining columns show from left to right the CosPGD attack used as a targeted attack with targets $\overrightarrow{0}$ and $-\overrightarrow{f}$, the PCFA attack, proposed as only a targeted attack, with target $-\overrightarrow{f}$, and last, the Adversarial Weather Attack with snow particles optimized as a non-targeted attack.

6 Model Analysis

To demonstrate the potential of FlowBench, we use it to perform multiple analyses, which provide us with a better understanding of many optical flow estimation methods. In the following, we discuss the observations. We benchmark the performance of all prominent DL-based optical flow estimation methods across three datasets, namely KITTI2015, MPI Sintel (clean), and MPI Sintel (final), against SotA and commonly used adversarial attacks such as BIM, PGD, and CosPGD. Tab. 1 provides an overview of all conducted experiments. Please refer to Appendix C for details on the dataset, Appendix D for additional implementation details, and Appendix H for additional results from the benchmarking.

6.1 Analyzing Method Families

We start by analyzing properties of the different optical flow method families as discussed in Sec. 3, by comparing their i.i.d. performance but also their NARE and TARE values. These are reliability error metrics, high values indicate low reliability. Refer to Appendix D for more implementation details.

In Fig. 3a we observe that methods belonging to the FlowFormer-family and RAFT-family and DIP (Zheng et al., 2022) have the best i.i.d. performance, however, given their relatively higher NARE_{20} and TARE_{20} values, some exceeding 100, they appear to not be reliable. Here we observe that IRR (Hur & Roth, 2019) stands out as one of the most reliable methods under adversarial attacks. Given that the primary differences between IRR-PWC and other methods from the PWC family are the classical energy minimization-inspired approach and the use of residual networks to propose an iterative residual refinement, one might hypothesize whether the inclusion of model-driven components will in general lead to more reliable methods.

When considering generalization ability under common corruptions, we observe that all methods have poor performance. Methods such as LLA-Flow (Xu et al., 2023b) and HD3 (Yin et al., 2019) from the RAFT-family and PWC-family respectively, have GAE_3 values over 160. Here, SplatFlow (Wang et al., 2024) yields surprisingly good results. Its primary difference to other RAFT-family methods is the use of splatting for feature matching.

Additionally, we observe in Fig. 3a that compared to other method families, the FlowFormer family is very susceptible to targeted adversarial attacks. Given that the FlowFormer family comprises only transformer-based architectures for optical flow estimation, we note that this contradicts the observations made for

Table 1: Overview of available model checkpoints (model X, trained for dataset Y) in FlowBench and checkpoints used for benchmarking. We benchmarked all available checkpoints for KITTI2015 and MPI Sintel, which are marked in teal. Models for which only FlyingThings3D checkpoints are available were not benchmarked and thus are in gray. FlowBench supports a total of 37 methods and 90 checkpoints (FlyingThings3D + KITTI2015 + MPI Sintel), for which 57 checkpoints were available for KITTI2015 and MPI Sintel that were benchmarked, which are 31 unique methods.

Model	Dataset			Method Family	Time
	FlyingThings3D (Mayer et al., 2016)	KITTI2015 (Menze & Geiger, 2015)	MPI Sintel (Butler et al., 2012)		
CCMR (Jahedi et al., 2024a)	✗	✓	✓	RAFT	January 2024
CRAFT (Sui et al., 2022)	✓	✓	✓	RAFT	March 2022
CSFlow (Shi et al., 2022)	✓	✓	✗	RAFT	February 2022
DICL (Wang et al., 2020)	✓	✓	✓	PWC	October 2020
DIP (Zheng et al., 2022)	✓	✓	✓	Deep Inverse Patchmatch	April 2022
FastFlowNet (Kong et al., 2021)	✓	✓	✓	PWC	March 2021
Flow1D (Xu et al., 2021a)	✓	✓	✓	RAFT	April 2021
FlowFormer (Huang et al., 2022)	✓	✓	✓	FlowFormer	March 2022
FlowFormer++ (Shi et al., 2023b)	✓	✓	✓	FlowFormer	March 2023
FlowNet2.0 (Ilg et al., 2017)	✓	✗	✗	FlowNet	December 2016
GMA (Jiang et al., 2021a)	✓	✓	✓	RAFT	April 2021
GMFlow (Xu et al., 2022)	✓	✓	✓	RAFT	November 2021
GMFlowNet (Zhao et al., 2022)	✓	✓	✓	RAFT	March 2022
HD3 (Yin et al., 2019)	✓	✓	✓	PWC	December 2018
IRR (Hur & Roth, 2019)	✓	✓	✓	PWC	April 2019
LCV (Khairi et al., 2024)	✓	✗	✗	RAFT	July 2020
LiteFlowNet (Hui et al., 2018)	✓	✓	✓	FlowNet	May 2018
LiteFlowNet2 (Hui et al., 2020)	✗	✓	✓	FlowNet	February 2020
LiteFlowNet3 (Hui & Loy, 2020)	✗	✓	✓	FlowNet	July 2020
LLA-Flow (Xu et al., 2023b)	✓	✓	✓	RAFT	April 2023
MaskFlowNetS (Zhao et al., 2020)	✓	✗	✓	PWC	March 2023
MaskFlowNet (Zhao et al., 2020)	✗	✓	✓	PWC	March 2023
MS-RAFT+ (Jahedi et al., 2024b)	✓	✓	✓	RAFT	October 2022
MatchFlow (Dong et al., 2023)	✓	✓	✓	RAFT	March 2023
NeuFlow (Zhang et al., 2024)	✗	✗	✓	FlowNet	March 2024
PWC-Net (Sun et al., 2018)	✓	✗	✓	PWC	September 2017
RapidFlow (Morimitsu et al., 2024a)	✓	✓	✓	RAFT	May 2024
RAFT (Teed & Deng, 2020)	✓	✓	✓	RAFT	March 2020
RPKNet (Morimitsu et al., 2024b)	✓	✓	✓	RAFT	March 2024
ScopeFlow (Bar-Haim & Wolf, 2020)	✓	✓	✓	PWC	February 2020
SeparableFlow (Zhang et al., 2021)	✓	✓	✓	RAFT	October 2021
SKFlow (Sun et al., 2022)	✓	✓	✓	RAFT	November 2022
SplatFlow (Wang et al., 2024)	✗	✓	✗	RAFT	January, 2024
STaRFlow (Godet et al., 2021)	✓	✓	✓	SSRFlow	July 2020
Unimatch (Xu et al., 2023a)	✓	✗	✗	RAFT	November 2022
VCN (Yang & Ramanan, 2019)	✓	✗	✗	PWC	December 2019
VideoFlow (Shi et al., 2023a)	✓	✓	✓	RAFT	March 2023

transformer-based methods for image classification (Mahmood et al., 2021; Kim et al., 2024). However, this lack of generalization ability can also be attributed to the use of dynamic positional cost queries by both FlowFormer and FlowFormer++. Interestingly, when considering the NARE metric, NeuFlow (Zhang et al., 2024), which is a RAFT-like method using transformer blocks, also performs marginally worse than similar methods.

6.2 Impact Of The Number Of Learnable Parameters and the Point Matching Mechanisms

Several works for classification have shown that Deep Neural Networks with more parameters and less vulnerable to adversarial attacks, and generalize better to common corruptions (Liu et al., 2022; Ding et al., 2022; Hoffmann et al., 2021). In Fig. 3b, we therefore analyze the effect of the number of model parameters for optical flow estimation methods. While the number of learnable parameters has an impact on the performance of the methods to some extent (other than the exceptions of MaskFlowNet and HD3), the same does not hold for reliability and generalization ability in general. Methods such as FlowFormer, FlowFormer++ (FlowFormer-family), and VideoFlow (RAFT-family) have more parameters than other methods, however, they are less reliable and have a poor generalization ability. Conversely, methods like CSFlow and SplatFlow (both RAFT-family) have significantly fewer parameters but are more reliable under attack and generalize better than the other methods to distribution shifts. Within the PWC-family, the correlation between the number of parameters and the reliability is strongest, with a Kendall tau rank correlation of only 0.24 for NARE (the second plot in Fig. 3b). It is obvious from the low correlation, even in this example, that further aspects, such as the employed point-matching mechanism, matter at least equally.

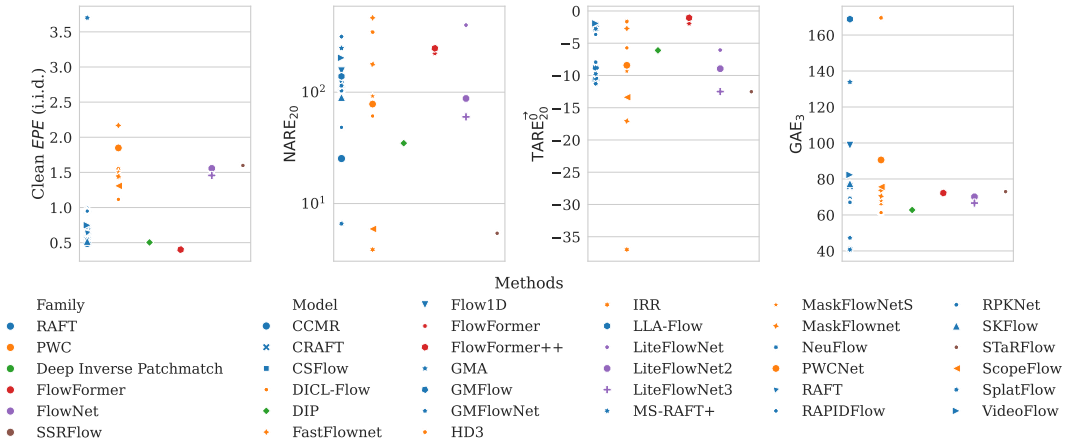

(a) Analyzing correlations between the method family to which the optical flow estimation method belongs and its corresponding performance, reliability, and generalization ability.

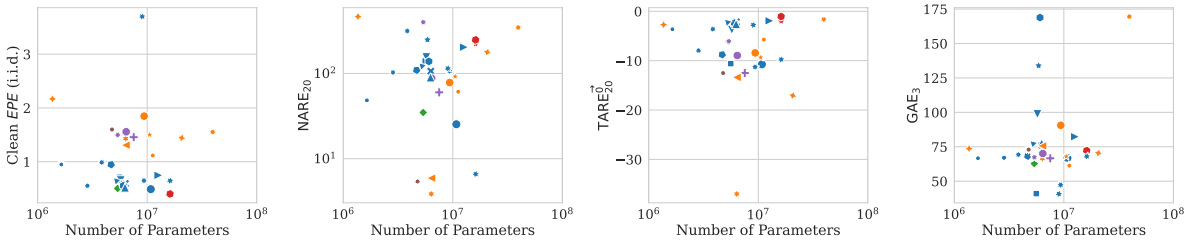

(b) Analyzing correlation between the number of learnable parameters in a DL-based optical flow estimation method and its performance, reliability, and generalization ability. Colors show the different optical flow methods, while marker styles show the method family to which they belong.

Figure 3: We observe that the performance of methods, especially families is independent of the number of parameters. This observation is contrary to known literature that shows methods in which a larger number of parameters perform better (Liu et al., 2022; Ding et al., 2022; Hoffmann et al., 2021). Additionally, we observe methods from the FlowFormer family lack robustness despite good i.i.d. performance. This contradicts the observations made for transformer-based methods for image classification (Paul & Chen, 2022; Hoyer et al., 2022) and semantic segmentation (Xie et al., 2021). Thus, we gather that optical flow methods are unique and need to be studied independently of other vision tasks as many known observations do not translate from other tasks to optical flow estimation.

Even within our considered model families, the models' approach to estimating, for example, cost volumes for point matching, differs significantly. While methods such as CCMR, CRAFT, Flow1D, NeuFlow or FlowFormer employ attention, most other methods employ convolution/correlation cost volumes. When considering attention-based methods, CCMR stands out with a rather low NARE and GAE. One key difference is their employed coarse-to-fine attention scheme, originally conceived to improve efficiency. When considering Multi-Scale approaches in general, we can further observe that MSRAFT+ performs even more reliably than CCMR. This follows the intuition that coarse-to-fine matching has a positive effect on prediction stability. Furthermore, approaches that mainly focused on improving the cost volume computation, such as DICL-Flow or LiteFlowNet3, tend to improve in terms of generalization over their respective predecessors.

6.3 Targeted v/s Non-targeted Adversarial Attacks

Next, we compare the NARE and TARE values (introduced in Sec. 5.2) and find correlations in their performance. We observe in Fig. 4a that there is a very high correlation between the $\text{TARE}^{\overrightarrow{0}}$ and $\text{TARE}^{\overrightarrow{-f}}$ values of every optical flow estimation method. This shows that evaluating either one of the values can serve as a reliable proxy for the other. We use this finding in the later analysis. Additionally, in Fig. 4a we observe

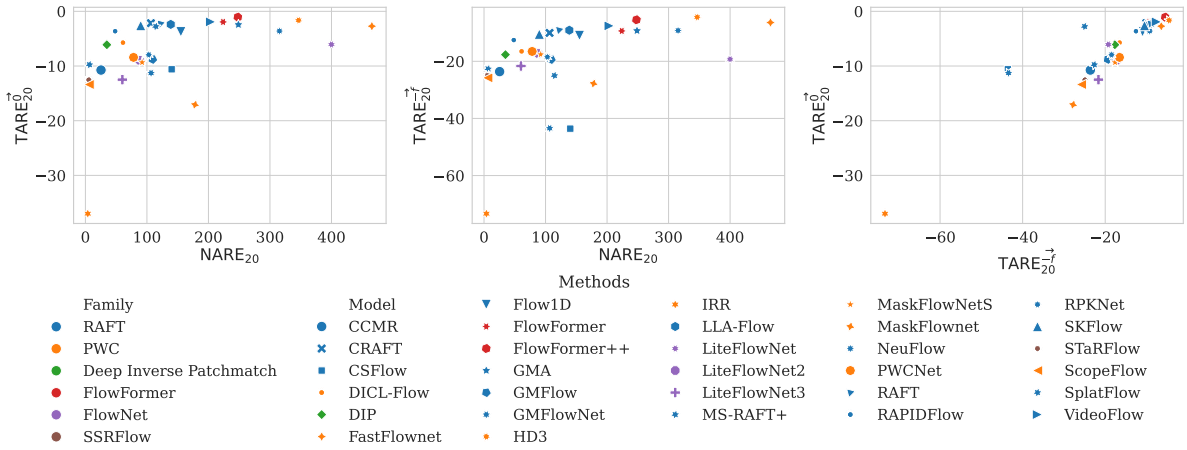

(a) Analyzing correlations between Targeted and Non-targeted adversarial attacks. A model is more reliable if it has a low NARE value and a low TARE value.

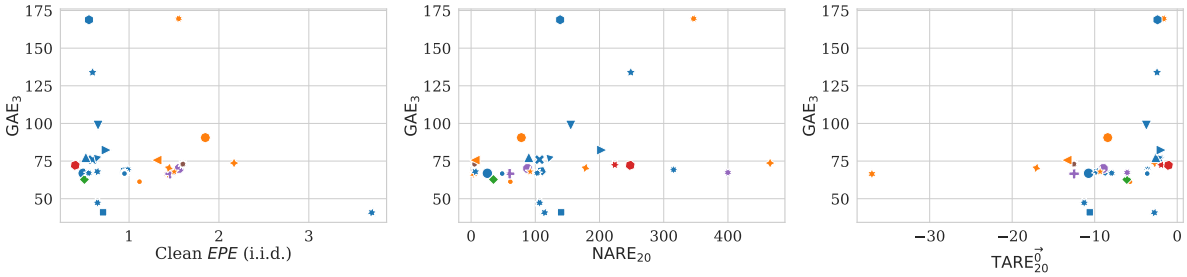

(b) Analyzing correlations between reliability and generalization ability of optical flow estimation methods.

Figure 4: We observe a strong positive correlation in the performance of optical flow estimation methods against targeted attacks with different targets ($\vec{0}$ and $\vec{-f}$), thus evaluating one serves as a good proxy for another. However, we do not find a strong positive correlation between generalization ability against common corruption and reliability under adversarial attacks. This hints that solutions for these problems might need to be with independent evaluations as the measures provide distinct information.

that most optical flow estimation methods like ScopeFlow (Bar-Haim & Wolf, 2020), MS-RAFT+ (Jahedi et al., 2024b) and StarFlow (Godet et al., 2021) are relatively more susceptible to targeted attacks than they are to non-targeted attacks. On the other hand, some methods are highly susceptible to both and thus very unreliable, these include SKFlow (Sun et al., 2022), FastFlowNet (Kong et al., 2021), HD3 (Yin et al., 2019) and some SotA methods like FlowFormer (Huang et al., 2022) and FlowFormer++ (Shi et al., 2023b). Interestingly, IRR (Hur & Roth, 2019) stands out as the most reliable optical flow estimation method as it is robust to both targeted and non-targeted adversarial attacks. While ScopeFlow (Bar-Haim & Wolf, 2020), GMFlowNet (Zhao et al., 2022) and MaskFlowNet (Zhao et al., 2020) are less reliable than IRR but more reliable than the other methods.

6.4 Reliability v/s Generalization

Following, we analyze if there is a correlation between the reliability and generalization ability of optical flow estimation methods. We observe in Fig. 4b, that most methods that have a good performance on i.i.d. samples also generalize better to distribution shifts as measured by GAE$_3$. However, methods like FlowFormer++, while having good i.i.d. performance, have a relatively poor generalization ability. As observed in Sec. 6.3, HD3 (Yin et al., 2019) stands out as having poor performance and poor generalization ability. Interestingly, as shown by Fig. 4b, there is a correlation between the generalization ability (GAE$_3$ values, introduced in Sec. 5.1, higher GAE value indicates lower generalization ability) and reliability when measured using non-targeted adversarial attacks (NARE$_{20}$ values). Additionally, most methods identified

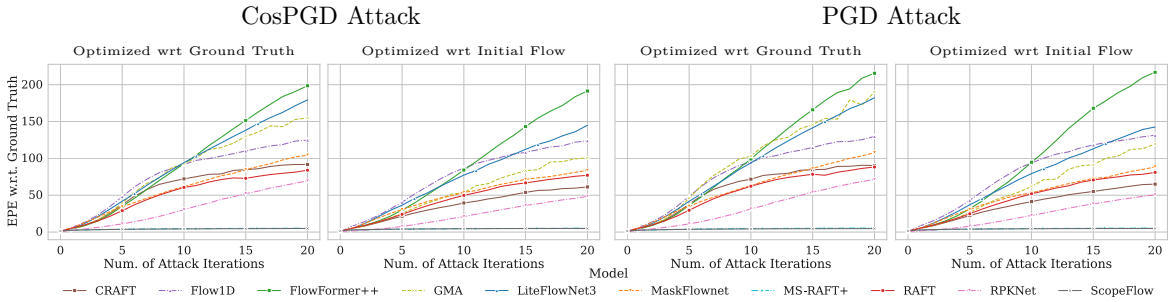

Figure 5: Performance of selected optical flow estimation methods under different non-targeted adversarial attacks optimized using initial flow predictions on the KITTI2015 dataset.

in Sec. 6.3 to be reliable, for example, CSFlow, MaskFlowNet, also have considerable generalization ability compared to the other methods. However, IRR, which stood out as the most reliable method, has low generalization abilities. It is interesting to note that CCMR (Jahedi et al., 2024a) offers a good trade-off as it has reasonably good performance, reliability, and generalization abilities.

6.5 Optimizing Targeted Attacks using Initial Flow Predictions

Based on the observation in Sec. 6, we identify several interesting methods whose performance warrants additional analysis and discussion. Following, we discuss our observations in detail.

One of the major limitations of white-box adversarial attacks is that they require access to the ground truth to optimize the attack (Agnihotri et al., 2024). However, access to the ground truth is not guaranteed in every scenario. Additionally, as discussed by Schmalfuss et al. (2022b), robustness is a measure of the difference in a model's prediction on perturbed input w.r.t. the model's prediction on clean input samples. Thus, the goal of an attack should be to fool the method into changing its initial predictions (predictions when the method is not attacked), independent of the ground truth. Thus, we attempt to optimize the adversarial attack w.r.t. to the initial flow prediction on the unperturbed input sample before any attacks, as access to this is almost guaranteed. This helps us ascertain if initial flow predictions can be used as a proxy to ground truth while optimizing attacks. Thus, in Eq. (4), Eq. (8), Eq. (9) and there places where applicable $\boldsymbol{Y}=\boldsymbol{X}^{\text{clean}}$ (please refer Appendix E.1). However, this optimization is only possible for attacks that introduce certain randomness in the initial input sample, as shown by Eq. (7). This allows for there to exist a non-zero loss between the predictions on the clean input samples and the perturbed input samples allowing for optimization. We report the evaluations for CosPGD and PGD attack using the KITTI2015 dataset for 10 interesting methods in Fig. 5. We choose the optical flow estimation methods on the basis of their performance in Sec. 6 and their performance on i.i.d. samples. For additional evaluation using more models please refer to Appendix H. We observe in Fig. 5 that there appears a high correlation in the performance of all considered methods under attack when optimized using the ground truth flow and the initial flow prediction, Thus, initial flow predictions from methods do serve as a strong proxy to the ground truth for optimizing attacks. This new finding over a big sample helps advance the study in the reliability of optical flow methods, even when ground truth predictions are not available.

7 Conclusion

FlowBench is the first robustness benchmarking tool and a novel benchmark for optical flow estimation methods. It currently supports 90 model checkpoints, over distinct datasets, and all relevant robustness evaluation methods, including SotA adversarial attacks and image corruptions. We discuss the unique features of FlowBench in detail and demonstrate that the library is user-friendly. Adding new evaluation methods or optical flow estimation methods to FlowBench is easy and intuitive. In Sec. 6.1, we show that methods from the FlowFormer family have good i.i.d. performance but are the most unreliable under targeted attacks, also that IRR stands out to have marginally better reliability. generalization abilities. In

Sec. 6.2, we show that, unlike image classification, increasing the number of learnable parameters does not help increase the robustness of optical flow estimation methods, however, a couple of RAFT variants have marginally better generalization abilities even with fewer parameters. In Sec. 6.3, we find that there is a high correlation in the performance of optical flow estimation methods against targeted attacks using different targets, thus saving compute for future works as they need to evaluate only against one target. In Sec. 6.4, we observe the methods known to be SotA on i.i.d. samples are not reliable and do not generalize well to image corruptions, demonstrating the gap in current research when considering real-world applications. Additionally, we observe here that there is no apparent correlation between generalization abilities and the reliability of optical flow estimation methods. These observations help us conclude that, based on current works, different approaches might be required to attain reliability under attacks and generalization ability to image corruptions. Lastly, in Sec. 6.5 we show that white-box adversarial attacks on optical flow estimation methods can be independent of the availability of ground truth information, and can harness the information in the initial flow predictions to optimize attacks, thus overcoming a huge limitation in the field. Such an in-depth understanding of reliability and generalization abilities to optical flow estimation methods can only be obtained using our proposed FlowBench. We are certain that FlowBench will be immensely helpful in gathering more such interesting findings and its comprehensive and consolidated nature would make things easier for the research community.

Future Work. For optical flow estimation, patch attacks are also interesting and widely studied (Ranjan et al., 2019; Schrodi et al., 2022; Scheurer et al., 2024). We plan to add such patch attacks to FlowBench in future iterations. Schmalfuss et al. (2022b) proposed optimizing adversarial noise jointly for the consecutive image frames and also over the entire evaluation set. Only PCFA supports such optimization regimes in FlowBench, so it would be interesting to extend such optimization to other adversarial attacks as well. Croce et al. (2021) show that the training methods used significantly impact the robustness of image classification methods. The same might be true for optical flow estimation methods, thus, robustness evaluations under the lens of different training setups used would make an interesting extension to the analysis in this work. Lastly, traditional non-DL-based optical flow estimation methods might be more robust to adversarial attacks than current DL-based methods. Thus, it would be interesting to study their robustness and hopefully adapt them to increase the reliability of current methods. Another interesting line of work considers black-box adversarial attacks. While white-box adversarial attacks serve as a probe for the quality of representations learned by a DL method, and thus, the stability of the output under a Lipschitz continuity bound, black-box adversarial attacks help test their performance under real-world threat scenarios. Moreover, while synthetic corruptions help study the performance of DL methods, they might not cover all real-world scenarios. Thus, including existing datasets like those introduced by Janai et al. (2017) would further improve the assessment of the real-world applicability of existing optical flow methods. These are some interesting future directions for FlowBench that we intend to pursue. Upon acceptance, FlowBench will be completely open-source, allowing the community to generate pull requests to add new methods, attacks, checkpoints, benchmarking results, and metrics, and thus pursue these directions of work as well.

Reproducibility Statement

Every experiment in this work is reproducible and is part of an effort toward open-source work. FlowBench will be open source and publicly available, including all evaluation logs and model checkpoint weights. This work intends to help the research community build more reliable and generalizable optical flow estimation methods such that they are ready for deployment in the real world, even under safety-critical applications. FlowBench is built upon ptlflow and thus any new model added with ptlflow would most likely be supported by FlowBench as well. The proposed FlowBench benchmarking tool is available as a library in the following codebase: `https://anonymous.4open.science/r/flowbench-TMLR`. The repository might not work as is due to anonymization. Upon acceptance, the FlowBench repository will be completely open-source, allowing the community to generate pull requests to add their new results and optimize the code base to add new attacks, new evaluation metrics and others.

There always exists stochasticity when evaluating adversarial attacks, due to the randomness these attacks exploit, and when evaluating common corruptions due to different seeds and calculation approximations

made by different Python libraries. Therefore, for transparency and reproducibility, we evaluate different runs on the same seed and different runs of different seeds. We report these evaluations in Appendix K, using Tab. 5 for adversarial attacks and Tab. 6 for common corruptions, and observe that the variance is extremely low and the analysis performed in this work still stands.

References

Shashank Agnihotri, Julia Grabinski, and Margret Keuper. Improving stability during upsampling – on the importance of spatial context, 2023.

Shashank Agnihotri, Steffen Jung, and Margret Keuper. CosPGD: an efficient white-box adversarial attack for pixel-wise prediction tasks. In *Proc. International Conference on Machine Learning (ICML)*, 2024.

Shashank Agnihotri, David Schader, Nico Sharei, Mehmet Ege Kaçar, and Margret Keuper. Are synthetic corruptions a reliable proxy for real-world corruptions? In *Synthetic Data for Computer Vision Workshop@ CVPR 2025*, 2025.

Hangbo Bao, Li Dong, Songhao Piao, and Furu Wei. BEit: BERT pre-training of image transformers. In *International Conference on Learning Representations*, 2022. URL `https://openreview.net/forum?id=p-BhZSz59o4`.

Aviram Bar-Haim and Lior Wolf. Scopeflow: Dynamic scene scoping for optical flow. In *Proc. IEEE/CVF Conference on Computer Vision and Pattern Recognition (CVPR)*, pp. 7998–8007, 2020.

Daniel J. Butler, Jonas Wulff, Garrett B. Stanley, and Michael J. Black. A naturalistic open source movie for optical flow evaluation. In *Proc. European Conference on Computer Vision (ECCV)*, LNCS 7577, pp. 611–625, 2012.

Linda Capito, Umit Ozguner, and Keith Redmill. Optical flow based visual potential field for autonomous driving. In *2020 IEEE Intelligent Vehicles Symposium (IV)*, pp. 885–891. IEEE, 2020.

Xiangxiang Chu, Zhi Tian, Yuqing Wang, Bo Zhang, Haibing Ren, Xiaolin Wei, Huaxia Xia, and Chunhua Shen. Twins: Revisiting the design of spatial attention in vision transformers. *Advances in neural information processing systems*, 34:9355–9366, 2021.

MMFlow Contributors. MMFlow: Openmmlab optical flow toolbox and benchmark. `https://github.com/open-mmlab/mmflow`, 2021.

Marius Cordts, Mohamed Omran, Sebastian Ramos, Timo Rehfeld, Markus Enzweiler, Rodrigo Benenson, Uwe Franke, Stefan Roth, and Bernt Schiele. The cityscapes dataset for semantic urban scene understanding, 2016.

Francesco Croce, Maksym Andriushchenko, Vikash Sehwag, Edoardo Debenedetti, Nicolas Flammarion, Mung Chiang, Prateek Mittal, and Matthias Hein. RobustBench: a standardized adversarial robustness benchmark. In *Advances in Neural Information Processing Systems (NeurIPS)*, 2021.

Francesco Croce, Naman D Singh, and Matthias Hein. Robust semantic segmentation: Strong adversarial attacks and fast training of robust models. *arXiv preprint arXiv:2306.12941*, 2023.

Tri Dao, Dan Fu, Stefano Ermon, Atri Rudra, and Christopher Ré. Flashattention: Fast and memory-efficient exact attention with io-awareness. *Advances in Neural Information Processing Systems*, 35:16344–16359, 2022.

Xiaohan Ding, Xiangyu Zhang, Jungong Han, and Guiguang Ding. Scaling up your kernels to 31x31: Revisiting large kernel design in cnns. In *Proc. of the IEEE/CVF conference on computer vision and pattern recognition*, pp. 11963–11975, 2022.

Qiaole Dong, Chenjie Cao, and Yanwei Fu. Rethinking optical flow from geometric matching consistent perspective. In *Proc. IEEE/CVF Conference on Computer Vision and Pattern Recognition (CVPR)*, pp. 1337–1347, 2023.

Alexey Dosovitskiy, Philipp Fischer, Eddy Ilg, Philip Hausser, Caner Hazirbas, Vladimir Golkov, Patrick Van Der Smagt, Daniel Cremers, and Thomas Brox. Flownet: Learning optical flow with convolutional networks. In *Proc. of the IEEE international conference on computer vision*, pp. 2758–2766, 2015.

Robert Geirhos, Patricia Rubisch, Claudio Michaelis, Matthias Bethge, Felix A Wichmann, and Wieland Brendel. Imagenet-trained cnns are biased towards texture; increasing shape bias improves accuracy and robustness. In *International Conference on Learning Representations*, 2018.

Robert Geirhos, Jörn-Henrik Jacobsen, Claudio Michaelis, Richard Zemel, Wieland Brendel, Matthias Bethge, and Felix A. Wichmann. Shortcut learning in deep neural networks. *Nature Machine Intelligence*, 2(11):665–673, nov 2020.

Pierre Godet, Alexandre Boulch, Aurélien Plyer, and Guy Le Besnerais. STaRFlow: A spatiotemporal recurrent cell for lightweight multi-frame optical flow estimation. In *Proc. IEEE International Conference on Pattern Recognition (ICPR)*, pp. 2462–2469, 2021.

Ian Goodfellow, Jonathon Shlens, and Christian Szegedy. Explaining and harnessing adversarial examples. In *Proc. International Conference on Learning Representations (ICLR)*, 2015.

Julia Grabinski, Paul Gavrikov, Janis Keuper, and Margret Keuper. Robust models are less over-confident. *NeurIPS*, 2022.

Dan Hendrycks and Thomas Dietterich. Benchmarking neural network robustness to common corruptions and perturbations. In *Proc. International Conference on Learning Representations (ICLR)*, 2019.

Dan Hendrycks, Norman Mu, Ekin D. Cubuk, Barret Zoph, Justin Gilmer, and Balaji Lakshminarayanan. AugMix: A simple data processing method to improve robustness and uncertainty. *Proc. of the International Conference on Learning Representations (ICLR)*, 2020.

J Hoffmann, S Agnihotri, Tonmoy Saikia, and Thomas Brox. Towards improving robustness of compressed cnns. In *ICML Workshop on Uncertainty and Robustness in Deep Learning (UDL)*, 2021.

Berthold KP Horn and Brian G Schunck. Determining optical flow. *Artificial intelligence*, 17(1-3):185–203, 1981.

Lukas Hoyer, Dengxin Dai, and Luc Van Gool. Daformer: Improving network architectures and training strategies for domain-adaptive semantic segmentation. In *Proceedings of the IEEE/CVF conference on computer vision and pattern recognition*, pp. 9924–9935, 2022.

Hsin-Ping Huang, Charles Herrmann, Junhwa Hur, Erika Lu, Kyle Sargent, Austin Stone, Ming-Hsuan Yang, and Deqing Sun. Self-supervised autoflow. In *Proceedings of the IEEE/CVF Conference on Computer Vision and Pattern Recognition (CVPR)*, pp. 11412–11421, June 2023.

Zhaoyang Huang, Xiaoyu Shi, Chao Zhang, Qiang Wang, Ka Chun Cheung, Hongwei Qin, Jifeng Dai, and Hongsheng Li. FlowFormer: A transformer architecture for optical flow. In *Proc. European Conference on Computer Vision (ECCV)*, LNCS 13677, pp. 668–685, 2022.

Tak-Wai Hui and Chen Change Loy. LiteFlowNet3: Resolving correspondence ambiguity for more accurate optical flow estimation. In *Proc. European Conference on Computer Vision (ECCV)*, LNCS 12365, pp. 169–184, 2020.

Tak-Wai Hui, Xiaoou Tang, and Chen Change Loy. LiteFlownet: A lightweight convolutional neural network for optical flow estimation. In *Proc. IEEE/CVF Conference on Computer Vision and Pattern Recognition (CVPR)*, pp. 8981–8989, 2018.

Tak-Wai Hui, Xiaoou Tang, and Chen Change Loy. A lightweight optical flow CNN—revisiting data fidelity and regularization. *IEEE Transactions on Pattern Analysis and Machine Intelligence (TPAMI)*, 43(8): 2555–2569, 2020.

Junhwa Hur and Stefan Roth. Iterative residual refinement for joint optical flow and occlusion estimation. In *Proc. IEEE/CVF Conference on Computer Vision and Pattern Recognition (CVPR)*, pp. 5754–5763, 2019.

Eddy Ilg, Nikolaus Mayer, Tonmoy Saikia, Margret Keuper, Alexey Dosovitskiy, and Thomas Brox. Flownet 2.0: Evolution of optical flow estimation with deep networks. In *Proc. IEEE/CVF Conference on Computer Vision and Pattern Recognition (CVPR)*, pp. 2462–2470, 2017.

Woobin Im, Sebin Lee, and Sung-Eui Yoon. Semi-supervised learning of optical flow by flow supervisor. In *European Conference on Computer Vision*, pp. 302–318. Springer, 2022.

Azin Jahedi, Maximilian Luz, Marc Rivinius, and Andrés Bruhn. CCMR: High resolution optical flow estimation via coarse-to-fine context-guided motion reasoning. In *Proc. IEEE/CVF Winter Conference on Applications of Computer Vision (WACV)*, pp. 6899–6908, 2024a.

Azin Jahedi, Maximilian Luz, Marc Rivinius, Lukas Mehl, and Andrés Bruhn. MS-RAFT+: high resolution multi-scale raft. *International Journal of Computer Vision (IJCV)*, 132(5):1835–1856, 2024b.

Joel Janai, Fatma Guney, Jonas Wulff, Michael J Black, and Andreas Geiger. Slow flow: Exploiting high-speed cameras for accurate and diverse optical flow reference data. In *Proceedings of the IEEE Conference on Computer Vision and Pattern Recognition*, pp. 3597–3607, 2017.

Shihao Jiang, Dylan Campbell, Yao Lu, Hongdong Li, and Richard Hartley. Learning to estimate hidden motions with global motion aggregation. In *Proc. IEEE/CVF International Conference on Computer Vision (ICCV)*, pp. 9772–9781, 2021a.

Shihao Jiang, Yao Lu, Hongdong Li, and Richard Hartley. Learning optical flow from a few matches. In *Proc. IEEE/CVF Conference on Computer Vision and Pattern Recognition (CVPR)*, pp. 16592–16600, 2021b.

Steffen Jung, Jovita Lukasik, and Margret Keuper. Neural architecture design and robustness: A dataset. In *ICLR*. OpenReview. net, 2023.

Oğuzhan Fatih Kar, Teresa Yeo, Andrei Atanov, and Amir Zamir. 3d common corruptions and data augmentation. In *Proc. IEEE/CVF Conference on Computer Vision and Pattern Recognition (CVPR)*, pp. 18963–18974, 2022.

Sarra Khairi, Etienne Meunier, Renaud Fraisse, and Patrick Bouthemy. Efficient local correlation volume for unsupervised optical flow estimation on small moving objects in large satellite images. In *Proc. IEEE/CVF Conference on Computer Vision and Pattern Recognition (CVPR)*, pp. 440–448, 2024.

Gihyun Kim, Juyeop Kim, and Jong-Seok Lee. Exploring adversarial robustness of vision transformers in the spectral perspective. In *Proceedings of the IEEE/CVF Winter Conference on Applications of Computer Vision*, pp. 3976–3985, 2024.

Hoki Kim. Torchattacks: A pytorch repository for adversarial attacks. *arXiv preprint arXiv:2010.01950*, 2020.

Daniel Kondermann, Rahul Nair, Stephan Meister, Wolfgang Mischler, Burkhard Güssefeld, Sabine Hofmann, Claus Brenner, and Bernd Jähne. Stereo ground truth with error bars. In *Asian Conference on Computer Vision, ACCV 2014*, 2014.

Lingtong Kong, Chunhua Shen, and Jie Yang. Fastflownet: A lightweight network for fast optical flow estimation. In *IEEE International Conference on Robotics and Automation (ICRA)*, pp. 10310–10316, 2021.

Alex Krizhevsky, Vinod Nair, and Geoffrey Hinton. Cifar-10 and cifar-100 datasets, learning multiple layers of features from tiny images. *URl: https://www. cs. toronto. edu/kriz/cifar. html*, 6(1):1, 2009.

Alexey Kurakin, Ian J. Goodfellow, and Samy Bengio. Adversarial machine learning at scale. In *Proc. International Conference on Learning Representations (ICLR)*, 2017.

Alexey Kurakin, Ian J Goodfellow, and Samy Bengio. Adversarial examples in the physical world. In *Artificial Intelligence Safety and Security*, pp. 99–112. Chapman and Hall/CRC, 2018.

Zhuang Liu, Hanzi Mao, Chao-Yuan Wu, Christoph Feichtenhofer, Trevor Darrell, and Saining Xie. A convnet for the 2020s. In *Proc. of the IEEE/CVF conference on computer vision and pattern recognition*, pp. 11976–11986, 2022.

Bruce D Lucas and Takeo Kanade. An iterative image registration technique with an application to stereo vision. In *IJCAI'81: 7th international joint conference on Artificial intelligence*, volume 2, pp. 674–679, 1981.

Kaleel Mahmood, Rigel Mahmood, and Marten Van Dijk. On the robustness of vision transformers to adversarial examples. In *Proceedings of the IEEE/CVF international conference on computer vision*, pp. 7838–7847, 2021.

Nikolaus Mayer, Eddy Ilg, Philip Hausser, Philipp Fischer, Daniel Cremers, Alexey Dosovitskiy, and Thomas Brox. A large dataset to train convolutional networks for disparity, optical flow, and scene flow estimation. In *Proc. IEEE/CVF Conference on Computer Vision and Pattern Recognition (CVPR)*, pp. 4040–4048, 2016.

Lukas Mehl, Jenny Schmalfuss, Azin Jahedi, Yaroslava Nalivayko, and Andrés Bruhn. Spring: A high-resolution high-detail dataset and benchmark for scene flow, optical flow and stereo. In *Proc. IEEE/CVF Conference on Computer Vision and Pattern Recognition (CVPR)*, pp. 4981–4991, 2023.

Moritz Menze and Andreas Geiger. Object scene flow for autonomous vehicles. In *Proc. IEEE/CVF Conference on Computer Vision and Pattern Recognition (CVPR)*, pp. 3061–3070, 2015.

Seyed-Mohsen Moosavi-Dezfooli, Alhussein Fawzi, and Pascal Frossard. Deepfool: a simple and accurate method to fool deep neural networks. In *Proc. of the IEEE conference on computer vision and pattern recognition*, pp. 2574–2582, 2016.

Henrique Morimitsu. Pytorch lightning optical flow. `https://github.com/hmorimitsu/ptlflow`, 2021.

Henrique Morimitsu, Xiaobin Zhu, Roberto M Cesar, Xiangyang Ji, and Xu-Cheng Yin. RAPIDFlow: Recurrent adaptable pyramids with iterative decoding for efficient optical flow estimation. In *IEEE International Conference on Robotics and Automation (ICRA)*, pp. 2946–2952, 2024a.

Henrique Morimitsu, Xiaobin Zhu, Xiangyang Ji, and Xu-Cheng Yin. Recurrent partial kernel network for efficient optical flow estimation. In *AAAI Conference on Artificial Intelligence (AAAI)*, 2024b.

Adam Paszke, Sam Gross, Francisco Massa, Adam Lerer, James Bradbury, Gregory Chanan, Trevor Killeen, Zeming Lin, Natalia Gimelshein, Luca Antiga, Alban Desmaison, Andreas Kopf, Edward Yang, Zachary DeVito, Martin Raison, Alykhan Tejani, Sasank Chilamkurthy, Benoit Steiner, Lu Fang, Junjie Bai, and Soumith Chintala. Pytorch: An imperative style, high-performance deep learning library. In *Advances in Neural Information Processing Systems 32*, pp. 8024–8035. Curran Associates, Inc., 2019.

Sayak Paul and Pin-Yu Chen. Vision transformers are robust learners. In *Proceedings of the AAAI Conference on Artificial Intelligence*, volume 36, pp. 2071–2081, 2022.

Adarsh Prasad. *Towards Robust and Resilient Machine Learning*. PhD thesis, Carnegie Mellon University, 2022.

Anurag Ranjan, Joel Janai, Andreas Geiger, and Michael J Black. Attacking optical flow. In *Proc. IEEE/CVF International Conference on Computer Vision (ICCV)*, pp. 2404–2413, 2019.

Jonas Rauber, Roland Zimmermann, Matthias Bethge, and Wieland Brendel. Foolbox native: Fast adversarial attacks to benchmark the robustness of machine learning models in pytorch, tensorflow, and jax. *Journal of Open Source Software*, 5(53):2607, 2020. doi: 10.21105/joss.02607. URL `https://doi.org/10.21105/joss.02607`.

Stephan R Richter, Zeeshan Hayder, and Vladlen Koltun. Playing for benchmarks. In *Proceedings of the IEEE international conference on computer vision*, pp. 2213–2222, 2017.

Benoît Rosa, Valentin Bordoux, and Florent Nageotte. Combining differential kinematics and optical flow for automatic labeling of continuum robots in minimally invasive surgery. *Frontiers in Robotics and AI*, 6:86, 2019.

Olga Russakovsky, Jia Deng, Hao Su, Jonathan Krause, Sanjeev Satheesh, Sean Ma, Zhiheng Huang, Andrej Karpathy, Aditya Khosla, Michael Bernstein, Alexander C. Berg, and Li Fei-Fei. ImageNet Large Scale Visual Recognition Challenge. *International Journal of Computer Vision (IJCV)*, 115(3):211–252, 2015. doi: 10.1007/s11263-015-0816-y.

Christos Sakaridis, Dengxin Dai, and Luc Van Gool. ACDC: The adverse conditions dataset with correspondences for semantic driving scene understanding. In *Proceedings of the IEEE/CVF International Conference on Computer Vision (ICCV)*, October 2021.

Erik Scheurer, Jenny Schmalfuss, Alexander Lis, and Andrés Bruhn. Detection defenses: An empty promise against adversarial patch attacks on optical flow. In *Proc. IEEE/CVF Winter Conference on Applications of Computer Vision (WACV)*, 2024.

Jenny Schmalfuss, Lukas Mehl, and Andrés Bruhn. Attacking motion estimation with adversarial snow. In *Proc. ECCV Workshop on Adversarial Robustness in the Real World (AROW)*, 2022a. doi: 10.48550/arXiv.2210.11242. URL `https://doi.org/10.48550/arXiv.2210.11242`.

Jenny Schmalfuss, Philipp Scholze, and Andrés Bruhn. A perturbation-constrained adversarial attack for evaluating the robustness of optical flow. In *Proc. European Conference on Computer Vision (ECCV)*, LNCS 13682, pp. 183–200, 2022b.

Jenny Schmalfuss, Lukas Mehl, and Andrés Bruhn. Distracting downpour: Adversarial weather attacks for motion estimation. In *Proc. IEEE/CVF International Conference on Computer Vision (ICCV)*, pp. 10106–10116, 2023.

Ludwig Schmidt, Shibani Santurkar, Dimitris Tsipras, Kunal Talwar, and Aleksander Madry. Adversarially robust generalization requires more data. *NIPS*, 31, 2018.

Simon Schrodi, Tonmoy Saikia, and Thomas Brox. Towards understanding adversarial robustness of optical flow networks. In *CVPR*, pp. 8916–8924, 2022.

Hao Shi, Yifan Zhou, Kailun Yang, Xiaoting Yin, and Kaiwei Wang. Csflow: Learning optical flow via cross strip correlation for autonomous driving. In *IEEE Intelligent Vehicles Symposium (IV)*, pp. 1851–1858, 2022.

Xiaoyu Shi, Zhaoyang Huang, Weikang Bian, Dasong Li, Manyuan Zhang, Ka Chun Cheung, Simon See, Hongwei Qin, Jifeng Dai, and Hongsheng Li. VideoFlow: Exploiting temporal cues for multi-frame optical flow estimation. In *Proc. IEEE/CVF International Conference on Computer Vision (ICCV)*, pp. 12469–12480, 2023a.

Xiaoyu Shi, Zhaoyang Huang, Dasong Li, Manyuan Zhang, Ka Chun Cheung, Simon See, Hongwei Qin, Jifeng Dai, and Hongsheng Li. FlowFormer++: Masked cost volume autoencoding for pretraining optical flow estimation. In *Proc. IEEE/CVF Conference on Computer Vision and Pattern Recognition (CVPR)*, pp. 1599–1610, 2023b.

Xiuchao Sui, Shaohua Li, Xue Geng, Yan Wu, Xinxing Xu, Yong Liu, Rick Goh, and Hongyuan Zhu. CRAFT: Cross-attentional flow transformer for robust optical flow. In *Proc. IEEE/CVF Conference on Computer Vision and Pattern Recognition (CVPR)*, pp. 17602–17611, 2022.

Deqing Sun, Xiaodong Yang, Ming-Yu Liu, and Jan Kautz. PWC-Net: CNNs for optical flow using pyramid, warping, and cost volume. In *Proc. IEEE/CVF Conference on Computer Vision and Pattern Recognition (CVPR)*, pp. 8934–8943, 2018.

Shangkun Sun, Yuanqi Chen, Yu Zhu, Guodong Guo, and Ge Li. SKFlow: Learning optical flow with super kernels. *Advances in Neural Information Processing Systems (NeurIPS)*, 35:11313–11326, 2022.

Shiyu Tang, Ruihao Gong, Yan Wang, Aishan Liu, Jiakai Wang, Xinyun Chen, Fengwei Yu, Xianglong Liu, Dawn Song, Alan Yuille, Philip H.S. Torr, and Dacheng Tao. Robustart: Benchmarking robustness on architecture design and training techniques. *https://arxiv.org/pdf/2109.05211.pdf*, 2021.

Zachary Teed and Jia Deng. RAFT: Recurrent all-pairs field transforms for optical flow. In *Proc. European Conference on Computer Vision (ECCV)*, LNCS 12347, pp. 402–419, 2020.

Dustin Tran, Jeremiah Liu, Michael W Dusenberry, Du Phan, Mark Collier, Jie Ren, Kehang Han, Zi Wang, Zelda Mariet, Huiyi Hu, et al. Plex: Towards reliability using pretrained large model extensions. *arXiv preprint arXiv:2207.07411*, 2022.

Dimitris Tsipras, Shibani Santurkar, Logan Engstrom, Alexander Turner, and Aleksander Madry. Robustness may be at odds with accuracy. In *ICLR*, 2019.

Bo Wang, Yifan Zhang, Jian Li, Yang Yu, Zhenping Sun, Li Liu, and Dewen Hu. Splatflow: Learning multi-frame optical flow via splatting. *International Journal of Computer Vision*, pp. 1–23, 2024.

Hengli Wang, Peide Cai, Yuxiang Sun, Lujia Wang, and Ming Liu. Learning interpretable end-to-end vision-based motion planning for autonomous driving with optical flow distillation. In *2021 IEEE International Conference on Robotics and Automation (ICRA)*, pp. 13731–13737. IEEE, 2021.

Jianyuan Wang, Yiran Zhong, Yuchao Dai, Kaihao Zhang, Pan Ji, and Hongdong Li. Displacement-invariant matching cost learning for accurate optical flow estimation. *Advances in Neural Information Processing Systems (NeurIPS)*, 33:15220–15231, 2020.

Eric Wong, Leslie Rice, and J. Zico Kolter. Fast is better than free: Revisiting adversarial training. *ArXiv*, abs/2001.03994, 2020.

J. Wulff, D. J. Butler, G. B. Stanley, and M. J. Black. Lessons and insights from creating a synthetic optical flow benchmark. In A. Fusiello et al. (Eds.) (ed.), *ECCV Workshop on Unsolved Problems in Optical Flow and Stereo Estimation*, Part II, LNCS 7584, pp. 168–177. Springer-Verlag, October 2012.

Enze Xie, Wenhai Wang, Zhiding Yu, Anima Anandkumar, Jose M Alvarez, and Ping Luo. Segformer: Simple and efficient design for semantic segmentation with transformers. *Advances in neural information processing systems*, 34:12077–12090, 2021.

Haofei Xu, Jiaolong Yang, Jianfei Cai, Juyong Zhang, and Xin Tong. High-resolution optical flow from 1d attention and correlation. In *Proc. IEEE/CVF International Conference on Computer Vision (ICCV)*, pp. 10498–10507, 2021a.

Haofei Xu, Jing Zhang, Jianfei Cai, Hamid Rezatofighi, and Dacheng Tao. GMFlow: Learning optical flow via global matching. In *Proc. IEEE/CVF Conference on Computer Vision and Pattern Recognition (CVPR)*, pp. 8121–8130, 2022.

Haofei Xu, Jing Zhang, Jianfei Cai, Hamid Rezatofighi, Fisher Yu, Dacheng Tao, and Andreas Geiger. Unifying flow, stereo and depth estimation. *IEEE Transactions on Pattern Analysis and Machine Intelligence (TPAMI)*, 45(11):13941–13958, 2023a.

Jiawei Xu, Zongqing Lu, and Qingmin Liao. LLA-Flow: A lightweight local aggregation on cost volume for optical flow estimation. In *IEEE International Conference on Image Processing (ICIP)*, pp. 3220–3224, 2023b.

Xiaogang Xu, Hengshuang Zhao, and Jiaya Jia. Dynamic divide-and-conquer adversarial training for robust semantic segmentation. In *IEEE/CVF International Conference on Computer Vision (ICCV)*, pp. 7466–7475, 2021b. doi: 10.1109/ICCV48922.2021.00739.

Gengshan Yang and Deva Ramanan. Volumetric correspondence networks for optical flow. *Advances in Neural Information Processing Systems (NeurIPS)*, 32, 2019.

Zhichao Yin, Trevor Darrell, and Fisher Yu. Hierarchical discrete distribution decomposition for match density estimation. In *Proc. IEEE/CVF Conference on Computer Vision and Pattern Recognition (CVPR)*, pp. 6044–6053, 2019.

Feihu Zhang, Oliver J Woodford, Victor Adrian Prisacariu, and Philip HS Torr. Separable Flow: Learning motion cost volumes for optical flow estimation. In *Proc. IEEE/CVF International Conference on Computer Vision (CVPR)*, pp. 10807–10817, 2021.

Zhiyong Zhang, Huaizu Jiang, and Hanumant Singh. Neuflow: Real-time, high-accuracy optical flow estimation on robots using edge devices. *arXiv preprint arXiv:2403.10425*, 2024.

Shengyu Zhao, Yilun Sheng, Yue Dong, Eric I Chang, Yan Xu, et al. MaskFlownet: Asymmetric feature matching with learnable occlusion mask. In *Proc. IEEE/CVF Conference on Computer Vision and Pattern Recognition (CVPR)*, pp. 6278–6287, 2020.

Shiyu Zhao, Long Zhao, Zhixing Zhang, Enyu Zhou, and Dimitris Metaxas. Global matching with overlapping attention for optical flow estimation. In *Proc. IEEE/CVF Conference on Computer Vision and Pattern Recognition (CVPR)*, pp. 17592–17601, 2022.

Zihua Zheng, Ni Nie, Zhi Ling, Pengfei Xiong, Jiangyu Liu, Hao Wang, and Jiankun Li. DIP: Deep inverse patchmatch for high-resolution optical flow. In *Proc. IEEE/CVF Conference on Computer Vision and Pattern Recognition (CVPR)*, pp. 8925–8934, 2022.

FlowBench: Benchmarking Optical Flow Estimation Methods for Reliability and Generalization

Supplementary Material

Table Of Content

The supplementary material covers the following information:

    - ∗ Appendix H.2.4: Evaluations for all models against CosPGD attack under ℓ_∞-norm bound and ℓ_2-norm bound, as targeted (both targets $\overrightarrow{0}$ and $\overrightarrow{-f}$) and non-targeted attack, over multiple attack iterations.
    - ∗ Appendix H.2.5: Evaluations for all models against PCFA attack under ℓ_2-norm bound, as targeted (both targets $\overrightarrow{0}$ and $\overrightarrow{-f}$) attack, over multiple attack iterations.
    - ∗ Appendix H.2.6: Evaluations for all models against Adversarial Weather attack, all four conditions: Fog, Rain, Snow, and Sparks, as targeted (both targets $\overrightarrow{0}$ and $\overrightarrow{-f}$) and non-targeted attack.
  - Appendix H.3: We provide an overview of the performance of the benchmarked methods against 2D Common Corruptions and 3D Common Corruptions.
  - Appendix H.4: 2D Common Corruptions
    - ∗ Appendix H.4.1: Evaluating generalization capabilities of semi-supervised and self-supervised optical flow methods using 2D Common Corruptions.
    - ∗ Appendix H.4.2: Evaluations for all models under 2D Common Corruptions at severity 3, for KITTI2015, MPI Sintel (clean), and MPI Sintel (final) datasets.
  - Appendix H.5: Evaluations for all models under 3D Common Corruptions at severity 3, for KITTI2015, MPI Sintel (clean), and MPI Sintel (final) datasets.

- Appendix I: We share the initial prototype of the future website.

- Appendix J: We discuss the limitations of FlowBench.

- Appendix K: We discuss the reproducibility of our evaluations and show that the variance in metrics is extremely low and our analysis comfortably holds under these variances.

A Do Synthetic Corruptions Represent The Real World?

In their work Agnihotri et al. (2025), they find the correlation between mean mIoU over the ACDC evaluation dataset (Sakaridis et al., 2021) and mean mIoU over each 2D Common Corruption (Hendrycks & Dietterich, 2019) over the Cityscapes dataset (Cordts et al., 2016). We include Figure 6 from their work here for ease of understanding. All models were trained using the training subset of the Cityscapes dataset. ACDC is the Adverse Conditions Dataset with Correspondences for Semantic Driving Scene Understanding captured in similar scenes are cityscapes but under four different domains: Day/Night, Rain, Snow, and Fog in the wild. ACDC is a community-used baseline for evaluating the performance of semantic segmentation methods on domain shifts observed in the wild. They find that there exists a very strong positive correlation between the two. This shows, that **yes, synthetic corruptions can serve as a proxy for the real world**. Unfortunately, a similar "in the wild" captured dataset does not exist for optical flow estimation to evaluate the effect of domain shifts on the performance of optical flow methods. However, given that for the task of semantic segmentation, we find a very high positive correlation between the performance on real-world corruptions and synthetic corruptions, it is a safe assumption that the same would hold true for optical flow estimation as well. Thus, in this work, we evaluate against synthetic 2D Common Corruptions (Hendrycks & Dietterich, 2019) and synthetic 3D Common Corruptions (Kar et al., 2022).

B Reasons For Categorizing Methods To Their Respective Families

Over the years, various modifications have been proposed for DL-based optical flow estimation methods. These can be based on the training strategy used or new architectures. However, barring DIP Zheng et al. (2022) and StarFlow Godet et al. (2021) that appear to have significantly different architectures, most other optimal flow methods can be categorized into four major families: FlowNet (Dosovitskiy et al.,

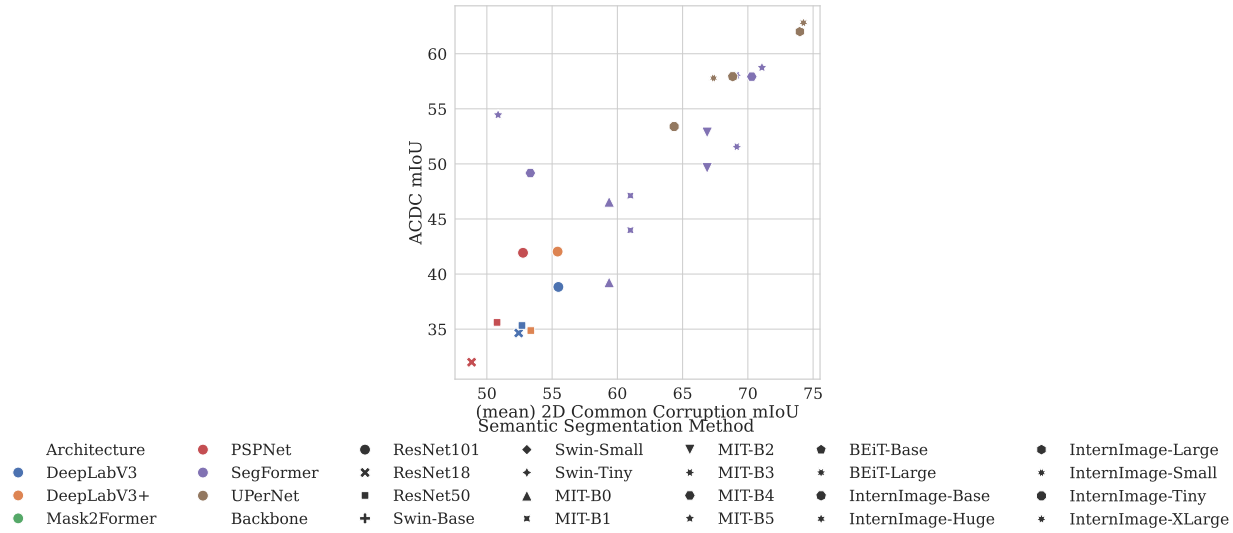

Figure 6: Results from work by Agnihotri et al. (2025). Here they find a **very strong positive correlation between mean mIoU over the ACDC evaluation dataset (Sakaridis et al., 2021) and mean mIoU over each 2D Common Corruption (Hendrycks & Dietterich, 2019)** over the Cityscapes dataset (Cordts et al., 2016). All models were trained using the training subset of the Cityscapes dataset. ACDC is the Adverse Conditions Dataset with Correspondences for Semantic Driving Scene Understanding, captured in similar scenes are cityscapes but under four different domains: Day/Night, Rain, Snow, and Fog in the wild. ACDC is a community-used baseline for evaluating the performance of semantic segmentation methods on domain shifts observed in the wild.

2015), PWC (Pyramid, Wrapping, and Cost Volume) (Sun et al., 2018), RAFT (Teed & Deng, 2020), and FlowFormer (Huang et al., 2022). In the following, we discuss the reasoning for our categorization. Please note, that methods categorized in one family can have high similarity to methods in another family. We usually solve this categorization problem by looking at when the method was proposed and which similarity was intended, for example, LiteFlowNets also have a pyramidal structure similar to PWCNets, however, they are categorized in the FlowNet family since the first LiteFlowNet paper was proposed around the same time as the first PWCNet paper and the similarity was not intended. Moreover, the functioning of the pyramidal structure in LiteFlowNets is significantly different from PWCNets.

B.1 FlowNet Family

Dosovitskiy et al. (2015) were the first to propose an end-to-end differentiable DL-based architecture for optical flow estimation, FlowNet. Many further works were inspired by FlowNet, making changes to FlowNet to propose novel optical flow estimation methods. These methods include:

- **FlowNet2.0** (Ilg et al., 2017): They improve upon FlowNet by changes to the schedule of training data usage, using a stacked architecture to include the warping of the second image with intermediate optical flow, and a sub-network to focus on small displacements.
- **LiteFlowNet** (Hui et al., 2018): Compared to FlowNet2.0 they use a more effective flow inference approach at each pyramid level through a lightweight cascaded network. They also use a flow regularization layer to ameliorate the issue of outliers and vague flow boundaries by using a feature-driven local convolution, and they use feature warping instead of image warping. They use the same training schedule as FlowNet2.0 but they train their network stage-wise.
- **LiteFlowNet2** (Hui et al., 2020): They improve the accuracy and latency from LiteFlowNet by making minor architectural changes to LiteFlowNet. They follow the training schedule of FlowNet2.0 to some extent and perform stage-wise training.

- **LiteFlowNet3** (Hui & Loy, 2020): They further improve upon the LiteFlowNet2.0 by amending each cost vector using an adaptive modulation before the flow decoding to alleviate the issue of outliers in the cost volume. Additionally, they replace each potentially inaccurately predicted optical flow with an accurate one from a near position through a warping of the flow field. They follow a special training schedule, first training the LiteFlowNet2 modules as mentioned in Hui et al. (2020), and then training the entire architecture again with the LiteFlowNet3 modifications to LiteFlowNet2 following the training protocol from FlowNet2.0.

B.2 PWC Family

While still using features from different at different scales, warping, and cost volume, Sun et al. (2018) proposed PWC-Net which with its architectural changes, presented a significant shift in architectures from the traditional FlowNet. Sun et al. (2018) describe, "PWC-Net uses the current optical flow estimate to warp the CNN features of the second image. It then uses the warped features and features of the first image to construct a cost volume, which is processed by a CNN to estimate the optical flow." This was faster than FlowNet2.0, easier to train, and significantly outperformed it on established benchmarks like KITTI2015 (Menze & Geiger, 2015) and MPI Sintel (Butler et al., 2012). PWC-Net uses a similar training schedule and protocol as FlowNet2.0. Many other works followed PWC-Net either changing the training strategy or making architectural changes to PWC-Net to further improve on i.i.d. performance. These methods include:

- **FastFlowNet** (Kong et al., 2021): They replace the dual convolution feature pyramid in PWC-Net with the head enhanced pooling pyramid (HEPP) for enhancing the high-resolution pyramid feature and reducing model size, then, they propose center dense dilated correlation layer (MFC) for constructing compact cost volume while keeping the large search radius. followed by shuffle block decoders (SBD) at each pyramid level to regress optical flow with significantly cheaper computation. They follow the same training protocol mentioned by FlowNet2.0.
- **DICL** (Wang et al., 2020): They improve upon PWC-Net by decoupling the connection between 2D displacements and learn the matching costs at each 2D displacement hypothesis independently, i.e., displacement-invariant cost learning. They apply the same 2D convolution-based matching net independently on each 2D displacement hypothesis to learn a 4D cost volume and avoid learning a 5D feature volume, thus saving computing resources. They use the same training protocol as PWC-Net and FlowNet2.0, and use the data augmentations proposed by VCN.
- **HD3** (Yin et al., 2019): They adapt a PWC-Net-like architecture for the decomposition of the discrete probability distribution instead of the feature representations allowing them to learn probabilistic pixel correspondences in both optical flow and stereo matching. They decompose the full match density into multiple scales hierarchically and estimate the local matching distributions at each scale conditioned on the matching and warping at coarser scales. This allows the local distributions to be composed together to form the global match density. They essentially follow the same training protocol as FlowNet2.0 while omitting some hard examples. Additionally, they use ImageNet1k (Russakovsky et al., 2015)-pre-trained weights for their pyramid feature extractor.
- **IRR** (Hur & Roth, 2019): They take inspiration from classical energy minimization approaches, as well as residual networks to propose an iterative residual refinement, they show that their proposed IRR can be combined with both FlowNets and PWC-Net. In our work, we consider their adaptation to PWC-Net as that has better i.i.d. performance. They use the same training procedure as PWC-Net but additionally set out-of-bound pixels (after applying augmentations the same as those in FlowNet2.0) as occluded.
- **MaskFlowNet** (Zhao et al., 2020): Zhao et al. (2020) apart their proposed Occlusion-Aware Feature Matching Module (OFMM) and Asymmetric Occlusion-Aware Feature Matching Module (AsymOFMM) in PWC-Net and consists to two cascaded subnetworks for obtaining dual feature pyramids. Their proposed method helps them overcome the ambiguity caused due to occlusions

in images that induce inaccuracies in the flow fields during warping. They use the same training protocol as IRR-PWC-Net. However, first, they train the MaskFlowNetS, then keep its weights frozen while training the entire MaskFlowNet. They use additional data from KITTI2015 and HD1k dataset (Kondermann et al., 2014) for fine-tuning on MPI-Sintel.

- **MaskFlowNetS** (Zhao et al., 2020): Proposed as the first stage of MaskFlowNet, MaskFlowNetS inherits the network architecture from PWC-Net, but replaces the feature matching modules (FMMs) by their proposed AsymOFMMs. They use the same training procedure as IRR-PWC-Net.
- **ScopeFlow** (Bar-Haim & Wolf, 2020): Bar-Haim & Wolf (2020) improve upon IRR-PWC-net by improving the data sampling process while testing the regularization and augmentations used to mitigate the bias induced by the training protocols. They keep some aspects of the training protocols from FlowNet2.0 intact while changing a few like cropping, and regularization at different stages of the multi-phase training.
- **VCN** Yang & Ramanan (2019): They improve upon the 4D cost volume used by variants of the PWC family by proposing volumetric encoder-decoder architectures that efficiently capture large receptive fields, multi-channel cost volumes that capture multi-dimensional notions of pixel similarities, and separable volumetric filtering that significantly reduces computation and parameters while preserving i.i.d. performance. They use a very similar training procedure as FlowNet2.0 and PWC-Net, however, with fewer iterations.

B.3 RAFT Family

Teed & Deng (2020) proposed Recurrent All-Pairs Field Transforms (RAFT) to extract per-pixel features to build a multi-scale 4D correlation volume for all pairs of pixels. Here a recurrent unit is used to perform lookups on these correlation volumes. They use additional data and fine-tuning compared to FlowNet2.0. RAFT was a significant architectural change from PWC-Nets and inspired many future works that made modifications to RAFT to further improve i.i.d. performance. These methods include:

- **CCMR** (Jahedi et al., 2024a): They propose adapting RAFT to use attention-based motion grouping concepts for multi-scale optical flow estimation. CCMR first computes global multi-scale context features and then uses them to guide the actual motion grouping. While iterating both steps over all coarse-to-fine scales, Jahedi et al. (2024a) adapt cross-covariance image transformers to allow for an efficient realization while maintaining scale-dependent properties. They use a training procedure similar to MS-RAFT+, after the traditionally followed training procedure of FlowNet2.0, they additionally finetune on a mixed set from KITTI and Viper dataset (Richter et al., 2017).
- **CRAFT** (Sui et al., 2022): CRAFT inherits the flow estimation pipeline of RAFT and revitalizes the correlation volume computation part with two proposed components: the Semantic Smoothing Transformer on the features from the second frame, and a Cross-Frame Attention Layer to compute the correlation volume. Sui et al. (2022) propose that these two components help suppress spurious correlations in the correlation volume. They use the same training procedure as RAFT.
- **CSFlow** (Shi et al., 2022): They propose, "Cross Strip Correlation module (CSC) and Correlation Regression Initialization module (CRI). CSC utilizes a striping operation across the target image and the attended image to encode global context into correlation volumes while maintaining high efficiency. CRI is used to maximally exploit the global context for optical flow initialization". They take inspiration from RAFT and adapt the multi-layer GRU from the stereo estimation task to optical flow. They follow a training procedure very similar to RAFT.
- **Flow1D** (Xu et al., 2021a): They take inspiration from transformers (Bao et al., 2022) and propose a 1D attention operation that is first applied in the vertical direction of the target image, and then a simple 1D correlation in the horizontal direction of the attended image to achieve 2D correspondence modeling effect. The directions of attention and correlation can also be exchanged, resulting in two 3D cost volumes that are concatenated for optical flow regression, where they adopt RAFT's

framework to estimate the optical flow iteratively. They follow a very similar training procedure to RAFT, however for harder datasets, they use additional data for fine-tuning.

- **GMA** (Jiang et al., 2021a): They adapt an RAFT architecture to include their proposed global motion aggregation (GMA) module, a transformer-based approach to find long-range dependencies between pixels in the first image, and perform global aggregation on the corresponding motion features. This modified RAFT architecture with a GMA further inspired other architectures and works for optical flow estimation. GMA has a very similar training procedure to RAFT.
- **GMFlow** (Xu et al., 2022): They adapt RAFT to identify correspondences in image pairs by comparing their feature similarities. They use transformer-based modules to enhance extracted features, followed by self-attention modules for feature matching and flow propagation. Their feature extraction and feature upsampling modules are identical to RAFT. They follow a very similar training procedure to RAFT.
- **GMFlowNet** (Zhao et al., 2022): They adopt the iterative update operator of RAFT as the optimization step for their proposed GMFlowNet. They use their proposed patch-based overlapping attention (POLA) instead of multi-headed self-attention of transformer blocks to extract large context features to improve the matching step. They follow a very similar training procedure to RAFT.
- **LCV** (Khairi et al., 2024): They propose a lightweight module for learnable cost volume that adds onto RAFT to improve i.i.d. performance. For training, they initialize their learnable cost volume kernels to be identity and directly load the pre-trained weights from RAFT, and then they follow a similar training schedule as RAFT but with significantly fewer iterations.
- **LLA-Flow** (Xu et al., 2023b): They propose the local similarity aggregation for 4D cost volume and present lightweight operations to diminish the impact of outliers caused by lack of texture. They apply their module on RAFT to improve i.i.d. performance. They follow a very similar training procedure to RAFT.
- **MS-RAFT+** (Jahedi et al., 2024b): MS-RAFT adapted RAFT for combining hierarchical concepts at multiple scales. MS-RAFT+ builds on top of MS-RAFT by exploiting an additional finer scale for estimating the flow, which is made feasible using the on-demand cost computation proposed by RAFT. They follow a very particular training schedule which is in parts similar to RAFT, however, due to an overhead of a number of learnable parameters, requires more data and training time.
- **MatchFlow** (Dong et al., 2023): They propose a different feature matching extractor (FME) to be used with RAFT and GMA module, this proposed FME is pre-trained on a different dataset, which allows for increased i.i.d. performance due to better feature extraction and matching. After incorporating the pre-trained FME, the resultant MatchFlow is trained very similarly to RAFT.
- **RapidFlow** (Morimitsu et al., 2024a): Inspired by RAFT, Morimitsu et al. (2024a) propose Recurrent Adaptable Pyramids with Iterative Decoding. They propose a recurrent feature encoder that uses a single shared block with efficient 1D layers (NeXt1D) to generate feature pyramids of variable levels. Their decoder is similar to RAFT, with a few changes inspired by SKFLow (Sun et al., 2022). They follow a very similar training procedure to RAFT.
- **RPKNet** (Morimitsu et al., 2024b): They adapt RAFT to use their proposed Partial Kernel Convolution (PKConv) layers and Separable Large kernels (SLK). PKConv is used to produce variable multi-scale features with a single shared block, while SLK is used to capture large context information with low computational cost. They follow a very similar training procedure to RAFT.
- **SCV** (Jiang et al., 2021b): They adapt RAFT to use a sparse correlation volume instead of a dense correlation volume. They follow a very similar training procedure to RAFT.
- **SeparableFlow** (Zhang et al., 2021): They propose a separable cost volume module, a drop-in replacement to RAFT's correlation cost volumes, that uses non-local aggregation layers to exploit global context cues and prior knowledge, to disambiguate motions in poorly constrained ambiguous regions. They follow a training procedure the same as RAFT.

- **SKFlow** (Sun et al., 2022): They propose using Super Kernels that allow for larger receptive fields allowing it to recover occluded motions. Finally, they use the non-local GMA module from GMA for optical flow estimations. They follow a similar training procedure to RAFT.
- **SplatFlow** (Wang et al., 2024): They essentially propose to use splatting for feature matching in architectures like RAFT and GMA. As SplatFlow is proposed to be a multi-frame optical flow estimation method, it requires three frames at a time for training as opposed to the two frames used by RAFT and GMA. We use their modified version with GMA. This requires first loading the pr-trained weights of GMA as proposed by GMA, freezing them, and training the GPU prediction and convex upsampling networks introduced by Splatflow. Then, all parameters are fine-tuned using dataset-specific finetuning procedures very similar to RAFT.
- **VideoFlow** (Shi et al., 2023a): They propose a multi-frame optical flow estimation method and use the same iterative flow refinement module as other methods in the RAFT family, specifically they use the SKBlocks from SKFlow. For feature extractors, they take inspiration from FlowFormer (Huang et al., 2022) and use ImageNet1k pre-trained Twins-SVT (Chu et al., 2021). They use three and five-image frames during training while following training procedures slightly similar to RAFT.
- **NeuFlow** (Zhang et al., 2024): Inspired by GMFlow, they use transformer-based blocks to implement global cross-attention, however, they use Flash Attention (Dao et al., 2022) for slight speed improvements. They use a very similar upsampling module as GMFlow and RAFT. However, to obtain feature maps with finer details, they directly extract features from the original images using a CNN block, instead of using features for matching at the $\frac{1}{16}^{\text{th}}$ and $\frac{1}{8}^{\text{th}}$ scale like RAFT and GMFlow. They use a very similar training procedure as RAFT.

B.4 FlowFormer Family

Proposed by Huang et al. (2022), FlowFormer marks a significant shift in the architecture of optical flow estimation methods compared to the RAFT family.

- **FlowFormer** (Huang et al., 2022): It is a transformer-based neural network architecture for optical flow estimation. Huang et al. (2022) describe, FlowFormer tokenizes the 4D cost volume built from an image pair, encodes the cost tokens into a cost memory with alternate group transformer (AGT) layers in a latent space, and decodes the cost memory via a recurrent transformer decoder with dynamic positional cost queries. The two-stage Twins-SVT (Chu et al., 2021) feature extractor is pre-trained on the ImageNet1k dataset. After that, the training procedure of the entire FlowFormer is similar to RAFT's training procedure.
- **FlowFormer++** (Shi et al., 2023b): This is built upon FlowFormer to include Masked Cost Volume Autoencoding (MCVA) to improve the i.i.d. performance of FlowFormer by pre-training the cost-volume encoder with a mask encoding strategy proposed by them. FlowFormer++ requires significantly different pre-training, while the training and fine-tuning procedures are similar to RAFT.

C Dataset Details

FlowBench supports a total of four distinct optical flow datasets. Following, we describe these datasets in detail.

C.1 FlyingThings3D

This is a synthetic dataset proposed by Mayer et al. (2016) largely used for training and evaluation of optical flow estimation methods. This dataset consists of 25000 stereo frames, of everyday objects such as chairs, tables, cars, etc. flying around in 3D trajectories. The idea behind this dataset is to have a large volume of trajectories and random movements rather than focus on a real-world application. In their work, Dosovitskiy et al. (2015) showed models trained on FlyingThings3D can generalize to a certain extent to other datasets.

C.2 KITTI2015

Proposed by Menze & Geiger (2015), this dataset is focused on the real-world driving scenario. It contains a total of 400 pairs of image frames, split equally for training and testing. The image frames were captured in the wild while driving around on the streets of various cities. The ground-truth labels were obtained by an automated process.

C.3 MPI Sintel

Proposed by Butler et al. (2012) and Wulff et al. (2012), this dataset is derived from an open-source animated short film and consists of a total of 1064 synthetic frames for training and 564 synthetic frames for testing, both at a resolution of 1024×436. The intention of this dataset is to enforce realism while having a dataset at scale. This dataset is provided as two datasets, which are passes with more transformations and effects on the frames that originally have constant albedo over time, these passes are,

- MPI Sintel (clean): This is the clean pass that adds some realism to the images by adding some spectral effects, like illumination, shadows, and smooth shading.
- MPI Sintel (final): This is the final pass that adds more realism by adding effects such as blur due to depth and camera focus, blur due to motion, and atmospheric effects such as snow during snow storms, etc.

C.4 Spring

Similar to MPI Sintel, Mehl et al. (2023) proposed a new dataset and benchmark for optical flow estimation, which is much larger than any other dataset before. It consists of frames from the open-source Blender movie "Spring" and consists of 6000 stereo image pairs from 47 sequences with SotA visual effects at full HD resolution (1920×1080 pixels).

D Implementation Details Of The Benchmark

Following we provide details regarding the experiments done for creating the benchmark used in the analysis. In Fig. 7 we provide an overview of the FlowBench benchmarking tool.

Compute Resources. Most experiments were done on a single 40 GB NVIDIA Tesla V100 GPU each, however, MS-RAFT+, FlowFormer, and FlowFormer++ are more compute-intensive, and thus 80GB NVIDIA A100 GPUs or NVIDIA H100 were used for these models, a single GPU for each experiment.

Datasets Used. Performing adversarial attacks and OOD robustness evaluations are very expensive and compute-intensive. Thus, performing evaluation using all model-dataset pairs is not possible given the limited computing resources at our disposal. Thus, for the benchmark, we only use KITTI2015, MPI Sintel (clean), and MPI Sintel (final) as these are the most commonly used datasets for evaluation (Ilg et al., 2017; Huang et al., 2022; Schmalfuss et al., 2022b; Schrodi et al., 2022; Agnihotri et al., 2024).

Metrics Calculation. In Sec. 5 we introduce three new metrics for better understanding our analysis, given the large scale of the benchmark created. For calculating TARE and NARE values we used BIM, PGD, and CosPGD attack with step size α=0.01, perturbation budget $\epsilon = \frac{8}{255}$ under the ℓ_∞-norm bound, as targeted and non-targeted attacks respectively. We use ℓ_∞-norm bound as we observe in Appendix H that there is a high correlation between the performance of optical flow estimation methods when attacked using ℓ_∞-norm bounded attacks and ℓ_2-norm bounded attacks. We use 20 attack iterations for calculating TARE and NARE as we observe in *Appendix H*, that at a lower number of iterations, the gap in performance of different optical flow estimation methods is small, thus an in-depth analysis would be difficult, and we do not go beyond 20 attack iterations as computing each attack step for an adversarial attack is very expensive, and

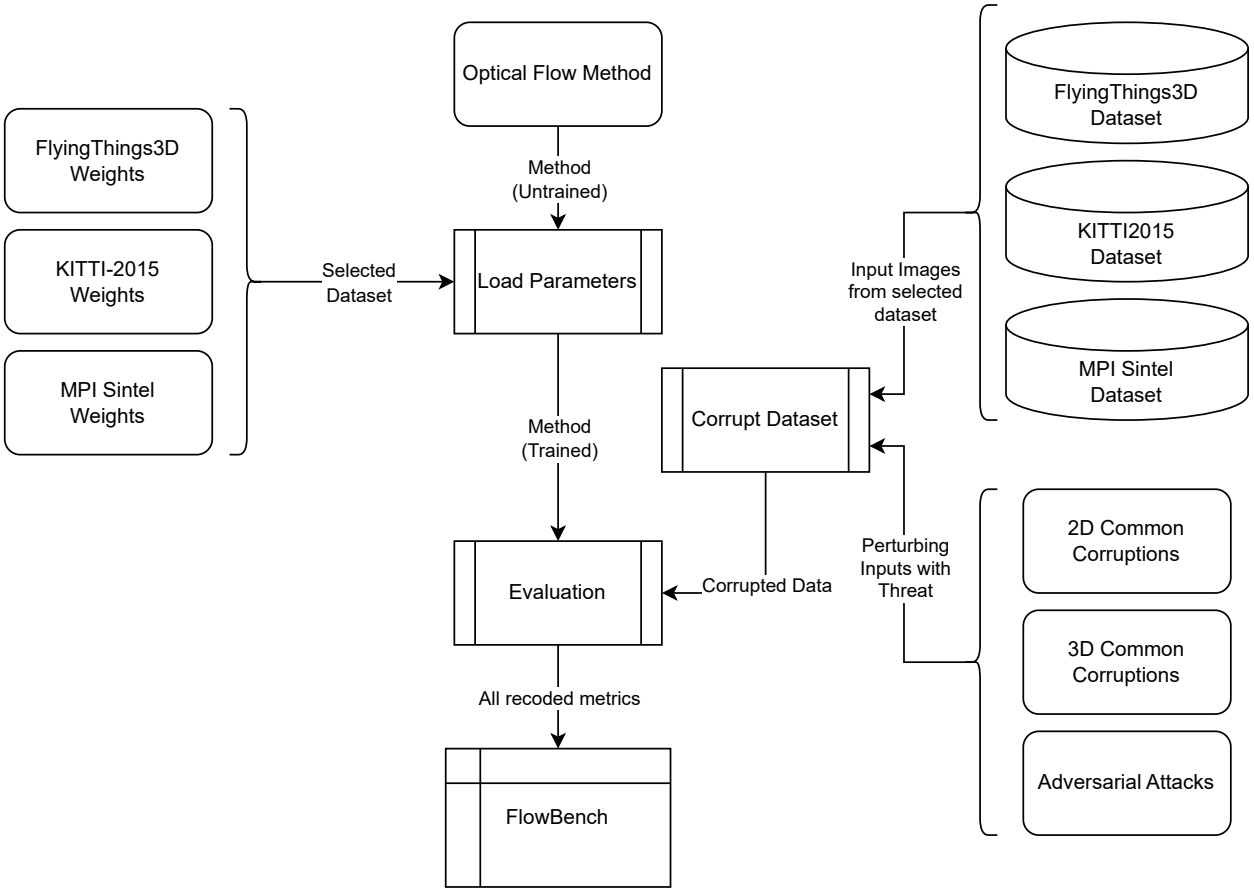

Figure 7: An overview of the FlowBench benchmarking tool.

as shown by Agnihotri et al. (2024) and Schmalfuss et al. (2022b), 20 iterations are enough to optimize an attack to truly understand the performance of the attacked method. For calculating GAE, we use all 15 2D Common Corruptions: 'Gaussian Noise', Shot Noise', 'Impulse Noise', 'Defocus Blur', 'Frosted Glass Blur', 'Motion Blur', 'Zoom Blur', 'Snow', 'Frost', 'Fog', 'Brightness', 'Contrast', 'Elastic Transform', 'Pixelate', 'JPEG Compression', and eight 3D Common Corruptions: 'Color Quantization', 'Far Focus', 'Fog 3D', 'ISO Noise', 'Low Light', 'Near Focus', 'XY Motion Blur', and 'Z Motion Blur'. All the common corruptions are at severity 3. Kar et al. (2022) offers more 3D Common Corruptions, however computing them is resource intensive. Thus, given our limited resources and an overlap in the corruptions between 2D Common Corruptions and 3D Common Corruptions, we focus on generating 3D Common Corruptions that might be unique from their 2D counterpart, require fewer sources to generate, and are interesting from an optical flow estimation perspective.

Calculating the EPE. EPE is the Euclidean distance between the two vectors, where one vector is the predicted flow by the optical flow estimation method and the other vector is the ground truth in case of i.i.d. performance evaluations, non-targeted attacks evaluations, and OOD robustness evaluations, while it is the target flow vector, in case of targeted attacks. For each dataset, the EPE value is calculated over all the samples of the evaluation set of the respective dataset, and then the mean EPE value is used as the mean-EPE of the respective method over the respective dataset.

Other Metrics. Apart from EPE, FlowBench also enables calculating a lot of other interesting metrics, such as ℓ_0, ℓ_2, ℓ_∞, distance between the perturbations of each image before and after a threat. Apart from these, in all scenarios, we also capture the outlier error, 1-px error, 3-px error, 5-px error, and cosine distance between two vectors. These vectors are the same as those in the case of EPE calculations. The 1-px, 3-px, and 5-px error metrics measure the percentage of pixels where the EPE between predicted and ground-truth

optical flow exceeds 1, 3, or 5 pixels, respectively. These thresholds evaluate the accuracy of flow estimates at different levels of tolerance, with lower thresholds indicating stricter accuracy. The outlier error in optical flow estimation is the percentage of pixels where the endpoint error exceeds both a fixed threshold (e.g., 3 pixels) and a relative threshold (e.g., more than 5% of the ground-truth flow magnitude), highlighting severe mismatches. The cosine distance measures the angular difference between predicted and ground-truth flow vectors, capturing errors in flow direction irrespective of magnitude. Lower values indicate better directional alignment. These metrics have been used my multiple previous works on optical flow estimation, such as Menze & Geiger (2015); Butler et al. (2012); Schmalfuss et al. (2022b); Mehl et al. (2023).

Let $f_{\text{gt}} = (u_{\text{gt}}, v_{\text{gt}})$ be the ground truth optical flow vector and $f_{\text{pred}} = (u_{\text{pred}}, v_{\text{pred}})$ be the predicted optical flow vector at a pixel. Then the formal definition for the metrics would be,

- **End-Point Error (EPE):**

$$\text{EPE} = \|f_{\text{pred}} - f_{\text{gt}}\|_2 = \sqrt{(u_{\text{pred}} - u_{\text{gt}})^2 + (v_{\text{pred}} - v_{\text{gt}})^2}$$

- L_0 **Distance (Number of non-zero flow errors):**

$$L_0 = \sum_i 1\left[f_{\text{pred}}^{(i)} \neq f_{\text{gt}}^{(i)}\right]$$

- L_1 **Distance:**

$$L_1 = \|f_{\text{pred}} - f_{\text{gt}}\|_1 = |u_{\text{pred}} - u_{\text{gt}}| + |v_{\text{pred}} - v_{\text{gt}}|$$

- L_∞ **Distance:**

$$L_\infty = \|f_{\text{pred}} - f_{\text{gt}}\|_\infty = \max\left(|u_{\text{pred}} - u_{\text{gt}}|, |v_{\text{pred}} - v_{\text{gt}}|\right)$$

We limited the analysis in this work to use EPE, since it is the most commonly used metric for evaluation, moreover, most works on optical flow estimation (Agnihotri et al., 2024; Schmalfuss et al., 2022b; Schrodi et al., 2022; Teed & Deng, 2020; Jahedi et al., 2024b) show a very high correlation between performance evaluations using different metrics.

Models Used. All available checkpoints, as shown in Tab. 2 for MPI Sintel and KITTI2015 dataset were used for creating the benchmark, except the following four models: Separableflow, SCV, VCN, Unimatch as due to special operations used in these models, they required specific libraries which were creating conflicts with all the others models, and as most of these models are very old and do not have performance close to SotA performance, we did not include them.

Adversarial Weather For generating adversarial weather attacks, we followed the implementation proposed by Schmalfuss et al. (2023). However, generating this attack is highly compute-intensive, and thus doing so for all models was not possible. Thus, based on the performance and reliability of all the models, we identified a few (eight) interesting models and only attacked them using the four different attacks curtailed within adversarial weather. This was done to demonstrate the capability of FlowBench to perform this attack. The following are the specifications for the weather attacks:

- Adversarial Weather: **Snow** (random snowflakes)
  - Number of Particles: 3000
  - Number of optimization steps: 750
- Adversarial Weather: **Rain** (rain streaks of length 0.15 with motion blur)
  - Number of Particles: 20
  - Number of optimization steps: 750

- Adversarial Weather: **Fog** (random large less opacity particles)
  - Number of Particles: 60
  - Number of optimization steps: 750
- Adversarial Weather: **Sparks** (random red sparks)
  - Number of Particles: 3000
  - Number of optimization steps: 750

Please note, that these specifications are identical to the optimal ones proposed by Schmalfuss et al. (2023).

E Description of FlowBench

Following, we describe the benchmarking tool, FlowBench. It is built using pltflow (Morimitsu, 2021), and supports 37 unique architectures and 4 distinct datasets, namely FlyingThings3D (Mayer et al., 2016), KITTI2015 (Menze & Geiger, 2015), MPI Sintel (Butler et al., 2012) (clean and final) and Spring (Mehl et al., 2023) datasets (please refer Appendix C for additional details on the datasets). It enables training and evaluations on all aforementioned datasets including evaluations using SotA adversarial attacks such as CosPGD (Agnihotri et al., 2024) and PCFA (Schmalfuss et al., 2022b), Adversarial weather (Schmalfuss et al., 2023), and other commonly used adversarial attacks like BIM (Kurakin et al., 2018), PGD (Kurakin et al., 2017), FGSM (Goodfellow et al., 2015), under various lipshitz (l_p) norm bounds.

Additionally, it enables evaluations for Out-of-Distribution (OOD) robustness by corrupting the inference samples using 2D Common Corruptions (Hendrycks & Dietterich, 2019) and 3D Common Corruptions (Kar et al., 2022).

We follow the nomenclature set by RobustBench (Croce et al., 2021) and use "threat_model" to define the kind of evaluation to be performed. When "threat_model" is defined to be "None", the evaluation is performed on unperturbed and unaltered images, if the "threat_model" is defined to be an adversarial attack, for example "PGD", "CosPGD" or "PCFA", then FlowBench performs an adversarial attack using the user-defined parameters. We elaborate on this in Appendix E.1. Whereas, if "threat_model" is defined to be "2DCommonCorruptions" or "3DCommonCorruptions", the FlowBench performs evaluations after perturbing the images with 2D Common Corruptions and 3D Common Corruptions respectively. We elaborate on this in Appendix E.2.

If the queried evaluation already exists in the benchmark provided by this work, then FlowBench simply retrieves the evaluations, thus saving computation.

E.1 Adversarial Attacks

FlowBench enables the use of all the attacks mentioned in Sec. 2.3 to help users better study the reliability of their optical flow methods. We choose to specifically include these white-box adversarial attacks as they either serve as the common benchmark for adversarial attacks in classification literature (FGSM, BIM, PGD, APGD) or they are unique attacks proposed specifically for pixel-wise prediction tasks (CosPGD) and optical flow estimation (PCFA and Adversarial Weather). These attacks can either be *Non-targeted* which are designed to simply fool the model into making incorrect predictions, irrespective of what the model eventually predicts, or can be *Targeted*, where the model is fooled to make a certain prediction. Most attacks can be, designed to be either Targeted or Non-targeted, these include, FGSM, BIM, PGD, APGD, CosPGD and Adversarial Weather. However, by design, some attacks are limited to being only one of the two, for example, PCFA which is a targeted attack. Following, we discuss these attacks in detail and highlight their key differences.

FGSM. Assuming a non-targeted attack, given a model f_θ and an unperturbed input sample $\boldsymbol{X}^{\text{clean}}$ and ground truth label $\boldsymbol{Y}$, FGSM attack adds noise δ to $\boldsymbol{X}^{\text{clean}}$ as follows,

$$\boldsymbol{X}^{\text{adv}} = \boldsymbol{X}^{\text{clean}} + \alpha \cdot \text{sign}\nabla_{\boldsymbol{X}^{\text{clean}}} L(f_\theta(\boldsymbol{X}^{\text{clean}}), \boldsymbol{Y}), \tag{1}$$

$$\delta = \phi^\epsilon(\boldsymbol{X}^{\text{adv}} - \boldsymbol{X}^{\text{clean}}), \tag{2}$$

$$\boldsymbol{X}^{\text{adv}} = \phi^r(\boldsymbol{X}^{\text{clean}} + \delta). \tag{3}$$

Here, $L(\cdot)$ is the loss function (differentiable at least once) which calculates the loss between the model prediction and ground truth, $\boldsymbol{Y}$. α is a small value of ϵ that decides the size of the step to be taken in the direction of the gradient of the loss w.r.t. the input image, which leads to the input sample being perturbed such that the loss increases. $\boldsymbol{X}^{\text{adv}}$ is the adversarial sample obtained after perturbing $\boldsymbol{X}^{\text{clean}}$. To make sure that the perturbed sample is semantically indistinguishable from the unperturbed clean sample to the human eye, steps from Eq. (2) and Eq. (3) are performed. Here, function ϕ^ϵ is clipping the δ in ϵ-ball for ℓ_∞-norm bounded attacks or the ϵ-projection in other l_p-norm bounded attacks, complying with the ℓ_∞-norm or other l_p-norm constraints, respectively. While function ϕ^r clips the perturbed sample, ensuring that it is still within the valid input space. FGSM, as proposed, is a single-step attack. For targeted attacks, $\boldsymbol{Y}$ is the target and α is multiplied by -1 so that a step is taken to minimize the loss between the model's prediction and the target prediction.

BIM. This is the direct extension of FGSM into an iterative attack method. In FGSM, $\boldsymbol{X}^{\text{clean}}$ was perturbed just once. While in BIM, $\boldsymbol{X}^{\text{clean}}$ is perturbed iteratively for time steps $t \in [0, \boldsymbol{T}]$, such that $t \in \mathbb{Z}^+$, where $\boldsymbol{T}$ are the total number of permissible attack iterations. This changes the steps of the attack from FGSM to the following,

$$\boldsymbol{X}^{\text{adv}_{t+1}} = \boldsymbol{X}^{\text{adv}_t} + \alpha \cdot \text{sign}\nabla_{\boldsymbol{X}^{\text{adv}_t}} L(f_\theta(\boldsymbol{X}^{\text{adv}_t}), \boldsymbol{Y}), \tag{4}$$

$$\delta = \phi^\epsilon(\boldsymbol{X}^{\text{adv}_{t+1}} - \boldsymbol{X}^{\text{clean}}), \tag{5}$$

$$\boldsymbol{X}^{\text{adv}_{t+1}} = \phi^r(\boldsymbol{X}^{\text{clean}} + \delta). \tag{6}$$

Here, at t=0, $\boldsymbol{X}^{\text{adv}_t}$=$\boldsymbol{X}^{\text{clean}}$.

PGD. Since in BIM, the initial prediction always started from $\boldsymbol{X}^{\text{clean}}$, the attack required a significant amount of steps to optimize the adversarial noise and yet it was not guaranteed that in the permissible ϵ-bound, $\boldsymbol{X}^{\text{adv}_{t+1}}$ was far from $\boldsymbol{X}^{\text{clean}}$. Thus, PGD proposed introducing stochasticity to ensure random starting points for attack optimization. They achieved this by perturbing $\boldsymbol{X}^{\text{clean}}$ with $\mathcal{U}(-\epsilon, \epsilon)$, a uniform distribution in $[-\epsilon, \epsilon]$, before making the first prediction, such that, at t=0

$$\boldsymbol{X}^{adv_t} = \phi^r(\boldsymbol{X}^{clean} + \mathcal{U}(-\epsilon, \epsilon)). \tag{7}$$

APGD. Auto-PGD is an effective extension to the PGD attack that effectively scales the step size α over attack iterations considering the compute budget and the success rate of the attack.

CosPGD. All previously discussed attacks were proposed for the image classification task. Here, the input sample is a 2D image of resolution H × W, where H and W are the height and width of the spatial resolution of the sample, respectively. Pixel-wise information is inconsequential for image classification. This led to the pixel-wise loss $\mathcal{L}(\cdot)$ being aggregated to L$(\cdot)$, as follows,

$$L(f_\theta(\boldsymbol{X}^{\text{adv}_t}), \boldsymbol{Y}) = \frac{1}{\text{H} \times \text{W}} \sum_{i \in \text{H} \times \text{W}} \mathcal{L}(f_\theta(\boldsymbol{X}^{\text{adv}_t})_i, \boldsymbol{Y}_i). \tag{8}$$

This aggregation of $\mathcal{L}(\cdot)$ fails to account for pixel-wise information available in tasks other than image classification, such as pixel-wise prediction tasks like Optical Flow estimation. Thus, in their work Agnihotri et al. (2024) propose an effective extension of the PGD attack that takes pixel-wise information into account by scaling $\mathcal{L}(\cdot)$ by the alignment between the distribution of the predictions and the distributions of $\boldsymbol{Y}$ before aggregating leading to a better-optimized attack, modifying Eq. (4) as follows,

$$\boldsymbol{X}^{\mathrm{adv}_{t+1}} = \boldsymbol{X}^{\mathrm{adv}_t} + \alpha \cdot \mathrm{sign} \nabla_{\boldsymbol{X}^{\mathrm{adv}_t}} \sum_{i \in H \times W} \cos\left(\psi(f_\theta(\boldsymbol{X}^{\mathrm{adv}_t})_i), \Psi(\boldsymbol{Y}_i)\right) \cdot \mathcal{L}\left(f_\theta(\boldsymbol{X}^{\mathrm{adv}_t})_i, \boldsymbol{Y}_i\right). \tag{9}$$

Where, functions ψ and Ψ are used to obtain the distribution over the predictions and $\boldsymbol{Y}_i$, respectively, and the function cos calculates the cosine similarity between the two distributions. CosPGD is the unified SotA adversarial attack for pixel-wise prediction tasks.

PCFA. Recently proposed by Schmalfuss et al. (2022b), is the SotA targeted adversarial attack specifically designed for optical flow estimation. It optimizes the input perturbation $\delta = \boldsymbol{X}^{\mathrm{adv}_t} - \boldsymbol{X}^{\mathrm{clean}}$ within a given l_2 bound to obtain a given target flow $\boldsymbol{Y}^{\mathrm{targ}}$. Mathematically, PCFA transforms the constrained optimization problem to find the most destructive perturbation under an l_2 constraint ε_2 into an unconstrained optimization problem by adding a term that penalizes deviations from the l_2 constraint:

$$\boldsymbol{X}^{\mathrm{adv}_{t+1}} = \boldsymbol{X}^{\mathrm{adv}_t} + \underset{\hat{\delta}}{\mathrm{argmin}}(\mathcal{L}(f_\theta(\boldsymbol{X}^{\mathrm{adv}_t}), \boldsymbol{Y}^{\mathrm{targ}}) + \mu \cdot \mathrm{ReLU}(\|\hat{\delta}\|_2^2 - (\varepsilon_2 \sqrt{2 \times H \times W})^2)) \tag{10}$$

Here, $\mathcal{L}(\cdot)$ is a generic loss function, like EPE or cosine distance. The penalty scaling parameter μ influences how severely deviations from the per-pixel l_2 bound ε_2 are penalized. The optimization problem $\underset{\hat{\delta}}{\mathrm{argmin}}(\cdot)$ is solved with an L-BFGS optimizer.

Adversarial Weather. Unlike the previous attacks which introduced per-pixel modifications, adversarial weather Schmalfuss et al. (2023; 2022a) attacks optical flow methods through optimizing the motion trajectories of rendered weather particles $\mathcal{P}$ like snow flakes, rain drops or fog clouds. The particle trajectories are modelled as positions $\boldsymbol{P} = \{\boldsymbol{P}_1, \boldsymbol{P}_2\}$ in the two frames I_1, I_2. Consequently, $\boldsymbol{X}^{\mathrm{adv}}(\boldsymbol{P})$ is generated by differentiably rendering the particles with their respective 3D positions to the 2D images. The update step optimizes the particle positions to achieve a certain target flow $\boldsymbol{Y}^{\mathrm{targ}}$ while simultaneously limiting the position offset size $\delta_{\boldsymbol{P}^t} = \boldsymbol{P}^{\mathrm{init}} - \boldsymbol{P}^t$:

$$\boldsymbol{X}^{\mathrm{adv}}(\boldsymbol{P}^{t+1}) = \boldsymbol{X}^{\mathrm{adv}}\Big(\boldsymbol{P}^t + \alpha \cdot \nabla_{\boldsymbol{P}^t}\Big(\mathrm{EPE}(f_\theta(\boldsymbol{X}^{\mathrm{adv}}(\boldsymbol{P}^t)), \boldsymbol{Y}^{\mathrm{targ}}) + \sum_{I \in 1,2} \frac{\beta_I}{|\mathcal{P}|} \sum_{j \in \mathcal{P}} \frac{\|\delta^j_{\boldsymbol{P}^t_I}\|_2^2}{d^j_I}\Big)\Big). \tag{11}$$

Here, β balances the two optimization goals of reaching the target flow and limiting trajectory offsets. The allowed trajectory offsets are further scaled with the particle depth d in the scene, to generate visually pleasing results.

Fig. 2, shows adversarial examples created using the SotA attacks and how they affect the model predictions.

E.2 Out-of-Distribution Robustness

While adversarial attacks help explore vulnerabilities of inefficient feature representations learned by a model, another important aspect of reliability is generalization ability. Especially, generalization to previously unseen samples or samples from significantly shifted distributions compared to the distribution of the samples seen while learning model parameters. As one cannot cover all possible scenarios during model training, a certain degree of generalization ability is expected from models. However, multiple works (Hendrycks & Dietterich, 2019; Kar et al., 2022; Hoffmann et al., 2021) showed that models are surprisingly less robust to distribution shifts, even those that can be caused by commonly occurring phenomena such as weather changes, lighting changes, etc. This makes the study of Out-of-Distribution (OOD) robustness an interesting avenue for research. Thus, to facilitate the study of robustness to such commonly occurring corruptions, FlowBench enables evaluating against prominent image corruption methods. Following, we describe these methods in detail.

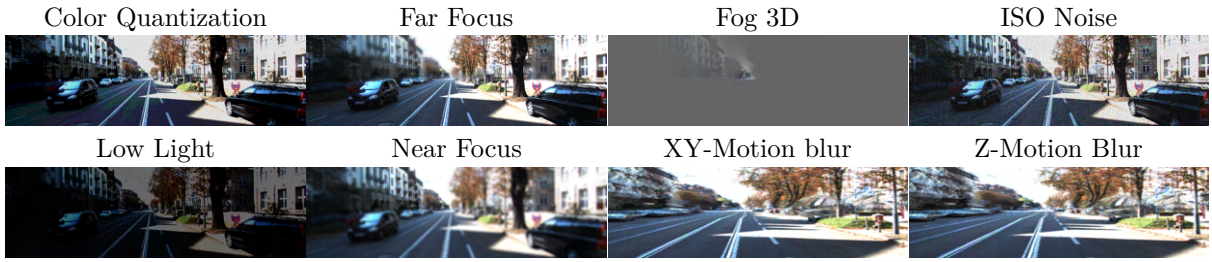

Figure 8: Examples of images from KITTI2015 corrupted using 3D Common Corruptions for evaluation of OOD robustness.

2D Common Corruptions. Hendrycks & Dietterich (2019) propose introducing distribution shift in the input samples by perturbing images with a total of 15 synthetic corruptions that could occur in the real world. These corruptions include weather phenomena such as fog, and frost, digital corruptions such as jpeg compression, pixelation, and different kinds of blurs like motion, and zoom blur, and noise corruptions such as Gaussian and shot noise amongst others corruption types. Each of these corruptions can perturb the image at 5 different severity levels between 1 and 5. The final performance of the model is the mean of the model's performance on all the corruptions, such that every corruption is used to perturb each image in the evaluation dataset. Since these corruptions are applied to a 2D image, they are collectively termed 2D Common Corruptions.

3D Common Corruptions. Since the real world is 3D, Kar et al. (2022) extend 2D Common Corruptions to formulate more realistic-looking corruptions by leveraging depth information (synthetic depth information when real depth is not readily available) and luminescence angles. They name these image corruptions as 3D Common Corruptions. Fig. 8, shows examples of KITTI2015 images corrupted using 3D Common Corruptions.

F Model Zoo

The trained checkpoints for all models available in FlowBench can be obtained using the following lines of code:

```
from flowbench.evals import load_model
model = load_model(model_name='RAFT', dataset='KITTI2015')
```

Each model checkpoint can be retrieved with the pair of 'model_name', the name of the model, and 'dataset', the dataset for which the checkpoint was last fine-tuned. In Table 2, we provide a comprehensive look-up table for all 'model_name' and 'dataset' pairs for which trained checkpoints are available in FlowBench.

G FlowBench Usage Details

Following we provide a detailed description of the evaluation functions and their arguments provided in FlowBench.

G.1 Adversarial Attacks

To evaluate a model for a given dataset, on an attack, the following lines of code are required.

```
from flowbench.evals import evaluate
model, results = evaluate(model_name='RAFT', dataset='KITTI2015',
                  threat_model='CosPGD', iterations=20, alpha=0.01,
```

Table 2: Overview of all available model checkpoints (model X, trained for dataset Y) in FlowBench.

Model	Dataset			Method Family	Time
	FlyingThings3D (Mayer et al., 2016)	KITTI2015 (Menze & Geiger, 2015)	MPI Sintel (Butler et al., 2012)		
CCMR (Jahedi et al., 2024a)	✗	✓	✓	RAFT	January 2024
CRAFT (Sui et al., 2022)	✓	✓	✓	RAFT	March 2022
CSFlow (Shi et al., 2022)	✓	✓	✗	RAFT	February 2022
DICL (Wang et al., 2020)	✓	✓	✓	PWC	October 2020
DIP (Zheng et al., 2022)	✓	✓	✓	Deep Inverse Patchmatch	April 2022
FastFlowNet (Kong et al., 2021)	✓	✓	✓	PWC	March 2021
Flow1D (Xu et al., 2021a)	✓	✓	✓	RAFT	April 2021
FlowFormer (Huang et al., 2022)	✓	✓	✓	FlowFormer	March 2022
FlowFormer++ (Shi et al., 2023b)	✓	✓	✓	FlowFormer	March 2023
FlowNet2.0 (Ilg et al., 2017)	✓	✗	✗	FlowNet	December 2016
GMA (Jiang et al., 2021a)	✓	✓	✓	RAFT	April 2021
GMFlow (Xu et al., 2022)	✓	✓	✓	RAFT	November 2021
GMFlowNet (Zhao et al., 2022)	✓	✓	✓	RAFT	March 2022
HD3 (Yin et al., 2019)	✓	✓	✓	PWC	December 2018
IRR (Hur & Roth, 2019)	✓	✓	✓	PWC	April 2019
LCV (Khairi et al., 2024)	✓	✗	✗	RAFT	July 2020
LiteFlowNet (Hui et al., 2018)	✓	✓	✓	FlowNet	May 2018
LiteFlowNet2 (Hui et al., 2020)	✗	✓	✓	FlowNet	February 2020
LiteFlowNet3 (Hui & Loy, 2020)	✗	✓	✓	FlowNet	July 2020
LLA-Flow (Xu et al., 2023b)	✓	✓	✓	RAFT	April 2023
MaskFlowNetS (Zhao et al., 2020)	✓	✗	✓	PWC	March 2023
MaskFlowNet (Zhao et al., 2020)	✗	✓	✓	PWC	March 2023
MS-RAFT+ (Jahedi et al., 2024b)	✓	✓	✓	RAFT	October 2022
MatchFlow (Dong et al., 2023)	✓	✓	✓	RAFT	March 2023
NeuFlow (Zhang et al., 2024)	✗	✗	✓	FlowNet	March 2024
PWC-Net (Sun et al., 2018)	✓	✗	✓	PWC	September 2017
RapidFlow (Morimitsu et al., 2024a)	✓	✓	✓	RAFT	May 2024
RAFT (Teed & Deng, 2020)	✓	✓	✓	RAFT	March 2020
RPKNet (Morimitsu et al., 2024b)	✓	✓	✓	RAFT	March 2024
ScopeFlow (Bar-Haim & Wolf, 2020)	✓	✓	✓	PWC	February 2020
SeparableFlow (Zhang et al., 2021)	✓	✓	✓	RAFT	October 2021
SKFlow (Sun et al., 2022)	✓	✓	✓	RAFT	November 2022
SplatFlow (Wang et al., 2024)	✗	✓	✗	RAFT	January, 2024
STaRFlow (Godet et al., 2021)	✓	✓	✓	SSRFlow	July 2020
Unimatch (Xu et al., 2023a)	✓	✗	✗	RAFT	November 2022
VCN (Yang & Ramanan, 2019)	✓	✗	✗	PWC	December 2019
VideoFlow (Shi et al., 2023a)	✓	✓	✓	RAFT	March 2023

```
epsilon=8/255, lp_norm='Linf', targeted=True,
optim_wrt='ground_truth', retrieve_existing=True)
```

The argument description is as follows:

- 'model_name' is the name of the optical flow estimation method to be used, given as a string.
- 'dataset' is the name of the dataset to be used also given as a string.
- 'threat_model' is the name of the adversarial attack to be used, given as a string.
- 'iterations' are the number of attack iterations, given as an integer.
- 'epsilon' is the permissible perturbation budget ϵ given a floating point (float).
- 'alpha' is the step size of the attack, α, given as a floating point (float).
- 'lp_norm' is the Lipschitz continuity norm (l_p-norm) to be used for bounding the perturbation, possible options are 'Linf' and 'L2' given as a string.
- 'targeted' is a boolean flag that decides if the attack must be targeted or not. If targeted='True', then by default the target is $\overrightarrow{0}$, passed as target='zero', this can be changed to negative of the initial flow by passing target='negative'.
- 'optim_wrt' decides wrt what attack should be optimized, available choices are 'ground_truth' and 'initial_flow' as string. Please note, this only works well with attacks that utilize Eq. (7).
- 'retrieve_existing' is a boolean flag, which when set to 'True' will retrieve the evaluation from the benchmark if the queried evaluation exists in the benchmark provided by this work, else FlowBench

will perform the evaluation. If the 'retrieve_existing' boolean flag is set to 'False' then FlowBench will perform the evaluation even if the queried evaluation exists in the provided benchmark.

G.2 Adversarial Weather

As an attack, adversarial weather works slightly different compared to other adversarial attacks, thus we additionally mention the commands for using adversarial weather.

```
from flowbench.evals import evaluate
model, results = evaluate(model_name='RAFT', dataset='Sintel-Final',
                  threat_model='Adversarial_Weather', weather='snow',
                  num_particles=10000, targeted=True,
                  retrieve_existing=True)
```

The argument description is as follows:

- 'model_name' is the name of the optical flow estimation method to be used, given as a string.
- 'dataset' is the name of the dataset to be used also given as a string.
- 'threat_model' is the name of the adversarial attack to be used, given as a string.
- 'weather' is the name of the weather condition in adversarial weather attack to be used, given as a string, options include 'snow', 'fog', 'rain' and 'sparks'.
- 'num_particles' is the number of particles per frame to be used, given as a integer.
- 'targeted' is a boolean flag that decides if the attack must be targeted or not. If targeted='True', then by default the target is $\overrightarrow{0}$, passed as target='zero', this can be changed to negative of the initial flow by passing target='negative'.
- 'optim_wrt' decides wrt what attack should be optimized, available choices are 'ground_truth' and 'initial_flow' as string. Please note, this only works well with attacks that utilize Eq. (7).
- 'retrieve_existing' is a boolean flag, which when set to 'True' will retrieve the evaluation from the benchmark if the queried evaluation exists in the benchmark provided by this work, else FlowBench will perform the evaluation. If the 'retrieve_existing' boolean flag is set to 'False' then FlowBench will perform the evaluation even if the queried evaluation exists in the provided benchmark.

Please note, adversarial weather data requires additional particle data as computed by Schmalfuss et al. (2023) and a path to the same should be provided as demonstrated in the GitHub repository: `https://anonymous.4open.science/r/flowbench-TMLR/`.

G.3 2D Common Corruptions

To evaluate a model for a given dataset, with 2D Common Corruptions, the following lines of code are required.

```
from flowbench.evals import evaluate
model, results = evaluate(model_name='RAFT', dataset='KITTI2015',
                  threat_model='2DCommonCorruption',
                  severity=3, retrieve_existing=True)
```

```
from flowbench.evals import evaluate
model, results = evaluate(model_name='RAFT', dataset='KITTI2015',
                  threat_config=config.yml,
                  retrieve_existing=True)
```

The argument description is as follows:

- 'model_name' is the name of the optical flow estimation method to be used, given as a string.
- 'dataset' is the name of the dataset to be used also given as a string.
- 'threat_model' is the name of the common corruption to be used, given as a string.
- 'severity' is the severity of the corruption, given as an integer between 1 and 5 (both inclusive).
- 'retrieve_existing' is a boolean flag, which when set to 'True' will retrieve the evaluation from the benchmark if the queried evaluation exists in the benchmark provided by this work, else FlowBench will perform the evaluation. If the 'retrieve_existing' boolean flag is set to 'False' then FlowBench will perform the evaluation even if the queried evaluation exists in the provided benchmark.

FlowBench supports the following 2D Common Corruption: 'gaussian_noise', shot_noise', 'impulse_noise', 'defocus_blur', 'frosted_glass_blur', 'motion_blur', 'zoom_blur', 'snow', 'frost', 'fog', 'brightness', 'contrast', 'elastic', 'pixelate', 'jpeg'. For the evaluation, FlowBench will evaluate the model on the validation images from the respective dataset corrupted using each of the aforementioned corruptions for the given severity, and then report the mean performance over all of them.

G.4 3D Common Corruptions

To evaluate a model for a given dataset, with 3D Common Corruptions, the following lines of code are required.

```
from flowbench.evals import evaluate
model, results = evaluate(model_name='RAFT', dataset='KITTI2015',
                  threat_model='3DCommonCorruption',
                  severity=3, retrieve_existing=True)
```

The argument description is as follows:

- 'model_name' is the name of the optical flow estimation method to be used, given as a string.
- 'dataset' is the name of the dataset to be used also given as a string.
- 'threat_model' is the name of the common corruption to be used, given as a string.
- 'severity' is the severity of the corruption, given as an integer between 1 and 5 (both inclusive).
- 'retrieve_existing' is a boolean flag, which when set to 'True' will retrieve the evaluation from the benchmark if the queried evaluation exists in the benchmark provided by this work, else FlowBench will perform the evaluation. If the 'retrieve_existing' boolean flag is set to 'False' then FlowBench will perform the evaluation even if the queried evaluation exists in the provided benchmark.

FlowBench supports the following 3D Common Corruption: 'color_quant', 'far_focus', 'fog_3d', 'iso_noise', 'low_light', 'near_focus', 'xy_motion_blur', and 'z_motion_blur'. For the evaluation, FlowBench will evaluate the model on the validation images from the respective dataset corrupted using each of the aforementioned corruptions for the given severity, and then report the mean performance over all of them.

H Additional Results

Following, we include additional results from the benchmark made using FlowBench.

Table 3: Results from a subset of methods adversarially finetuned on the KITTI2015 training dataset using non-targeted ℓ_∞-norm constrained 3 iterations PGD attack with $\epsilon \in [\frac{4}{255}, \frac{8}{255}]$ and $\alpha = 0.01$ and attacked with non-targeted ℓ_∞-norm constrained CosPGD, PGD, and BIM attack with $\epsilon \in [\frac{1}{255}, \frac{2}{255}, \frac{4}{255}, \frac{8}{255}]$ and Number of Attack Iterations $\in [3, 5, 10, 20]$.

Model	Training	Clean	CosPGD				PGD				BIM			
			$\epsilon = \frac{1}{255}$	$\epsilon = \frac{2}{255}$	$\epsilon = \frac{4}{255}$	$\epsilon = \frac{8}{255}$	$\epsilon = \frac{1}{255}$	$\epsilon = \frac{2}{255}$	$\epsilon = \frac{4}{255}$	$\epsilon = \frac{8}{255}$	$\epsilon = \frac{1}{255}$	$\epsilon = \frac{2}{255}$	$\epsilon = \frac{4}{255}$	$\epsilon = \frac{8}{255}$
Attack Iterations = 3														
FastFlowNet	Baseline	2.17	11.98	25.35	46.30	57.53	11.58	25.58	47.38	59.25	15.87	28.37	44.81	65.94
FastFlowNet	Adv $\epsilon = \frac{4}{255}$	29.81	29.41	29.66	29.99	30.42	29.00	29.02	29.27	29.46	28.70	29.09	30.37	31.77
FastFlowNet	Adv $\epsilon = \frac{8}{255}$	30.41	30.34	30.60	31.15	31.52	29.88	29.93	30.36	30.81	29.62	30.18	31.50	33.00
FlowFormer	Baseline	0.49	3.90	8.65	14.39	17.43	3.88	8.66	14.31	17.40	5.24	9.39	15.80	24.75
FlowFormer	Adv $\epsilon = \frac{4}{255}$	36.74	36.74	36.74	36.74	36.73	36.74	36.74	36.74	36.73	36.74	36.74	36.74	36.73
FlowFormer	Adv $\epsilon = \frac{8}{255}$	36.74	36.74	36.74	36.73	36.72	36.74	36.74	36.73	36.72	36.74	36.74	36.73	36.71
IRR-PWC	Baseline	1.44	1.60	1.80	2.28	2.61	1.59	1.78	2.25	2.66	1.61	1.85	2.37	3.57
IRR-PWC	Adv $\epsilon = \frac{4}{255}$	35.38	35.40	35.43	35.46	35.49	35.40	35.43	35.45	35.48	35.39	35.43	35.50	35.60
IRR-PWC	Adv $\epsilon = \frac{8}{255}$	35.74	35.75	35.77	35.80	35.82	35.75	35.77	35.79	35.82	35.75	35.77	35.82	35.89
RAFT	Baseline	0.64	3.67	8.85	15.01	17.54	3.71	8.85	15.14	17.48	5.69	10.13	16.93	27.16
RAFT	Adv $\epsilon = \frac{4}{255}$	1.81	4.02	7.11	10.61	12.02	3.95	7.13	10.55	11.97	4.89	7.64	11.37	16.26
RAFT	Adv $\epsilon = \frac{8}{255}$	1.99	4.25	7.38	10.69	12.06	4.15	7.30	10.65	12.02	5.14	7.87	11.45	16.04
Attack Iterations = 5														
FastFlowNet	Baseline	2.17	14.15	37.47	80.86	120.66	13.36	35.80	81.47	118.29	20.13	41.95	72.89	108.27
FastFlowNet	Adv $\epsilon = \frac{4}{255}$	29.81	29.37	29.61	30.17	31.07	29.00	29.03	29.42	30.22	28.77	29.15	30.22	31.71
FastFlowNet	Adv $\epsilon = \frac{8}{255}$	30.41	30.28	30.53	31.43	31.99	29.86	30.06	30.56	31.35	29.68	30.28	31.48	33.15
FlowFormer	Baseline	0.49	3.15	10.46	30.48	49.88	3.19	10.37	30.36	49.18	7.24	13.16	17.65	24.38
FlowFormer	Adv $\epsilon = \frac{4}{255}$	36.74	36.74	36.74	36.73	36.70	36.74	36.74	36.73	36.71	36.74	36.74	36.73	36.68
FlowFormer	Adv $\epsilon = \frac{8}{255}$	36.74	36.74	36.74	36.72	36.68	36.74	36.74	36.72	36.68	36.74	36.74	36.73	36.67
IRR-PWC	Baseline	1.44	1.60	1.81	2.31	2.99	1.60	1.79	2.35	3.05	1.62	1.87	2.37	3.42
IRR-PWC	Adv $\epsilon = \frac{4}{255}$	35.38	35.40	35.43	35.46	35.50	35.40	35.43	35.46	35.50	35.39	35.43	35.50	35.59
IRR-PWC	Adv $\epsilon = \frac{8}{255}$	35.74	35.75	35.77	35.79	35.83	35.75	35.77	35.79	35.82	35.75	35.77	35.82	35.88
RAFT	Baseline	0.64	3.39	12.12	31.58	43.72	3.44	12.29	31.66	42.84	8.05	15.51	24.80	37.33
RAFT	Adv $\epsilon = \frac{4}{255}$	1.81	3.83	8.06	17.98	21.75	3.71	8.11	18.06	21.73	5.71	9.51	14.33	20.40
RAFT	Adv $\epsilon = \frac{8}{255}$	1.99	3.99	8.29	17.88	21.53	3.87	8.24	17.82	21.29	5.98	9.62	14.00	19.51
Attack Iterations = 10														
FastFlowNet	Baseline	2.17	14.72	56.74	155.64	258.25	14.61	59.04	152.13	258.05	29.05	69.71	125.29	173.05
FastFlowNet	Adv $\epsilon = \frac{4}{255}$	29.81	29.86	29.89	30.76	32.37	29.40	29.32	29.83	31.64	28.77	28.91	30.14	32.44
FastFlowNet	Adv $\epsilon = \frac{8}{255}$	30.41	30.80	30.89	31.84	33.19	30.30	30.37	31.02	32.47	29.81	30.01	31.33	33.31
FlowFormer	Baseline	0.49	2.96	9.75	38.32	124.63	2.93	9.47	37.85	115.52	7.00	12.86	22.33	35.79
FlowFormer	Adv $\epsilon = \frac{4}{255}$	36.74	36.74	36.74	36.72	36.42	36.74	36.74	36.72	36.43	36.74	36.74	36.73	36.59
FlowFormer	Adv $\epsilon = \frac{8}{255}$	36.74	36.74	36.74	36.71	36.35	36.74	36.74	36.71	36.35	36.74	36.74	36.72	36.58
IRR-PWC	Baseline	1.44	1.60	1.79	2.38	3.39	1.60	1.80	2.35	3.48	1.60	1.80	2.33	3.46
IRR-PWC	Adv $\epsilon = \frac{4}{255}$	35.38	35.40	35.42	35.47	35.51	35.40	35.42	35.46	35.51	35.39	35.42	35.47	35.57
IRR-PWC	Adv $\epsilon = \frac{8}{255}$	35.74	35.75	35.77	35.80	35.84	35.75	35.77	35.80	35.83	35.75	35.76	35.80	35.87
RAFT	Baseline	0.64	3.18	11.59	40.53	97.49	3.17	11.23	39.64	96.35	7.73	13.64	24.77	43.54
RAFT	Adv $\epsilon = \frac{4}{255}$	1.81	3.55	7.64	20.38	42.78	3.52	7.64	20.89	42.60	5.54	8.82	14.38	20.58
RAFT	Adv $\epsilon = \frac{8}{255}$	1.99	3.74	7.75	20.45	40.90	3.70	7.44	19.61	40.72	5.52	8.86	13.42	20.16
Attack Iterations = 20														
FastFlowNet	Baseline	2.17	15.27	77.80	243.35	458.65	15.18	76.99	245.23	453.52	37.60	98.40	171.28	213.98
FastFlowNet	Adv $\epsilon = \frac{4}{255}$	29.81	29.85	29.98	31.27	34.75	29.41	29.27	30.41	34.30	28.84	28.92	30.66	33.95
FastFlowNet	Adv $\epsilon = \frac{8}{255}$	30.41	30.82	31.01	32.18	34.55	30.42	30.38	31.70	33.93	29.81	30.12	31.79	34.64
FlowFormer	Baseline	0.49	2.72	9.57	55.51	201.03	2.83	10.33	52.50	206.17	7.26	13.41	23.82	36.45
FlowFormer	Adv $\epsilon = \frac{4}{255}$	36.74	36.74	36.74	36.71	35.94	36.74	36.74	36.71	35.97	36.74	36.74	36.72	36.55
FlowFormer	Adv $\epsilon = \frac{8}{255}$	36.74	36.74	36.74	36.70	36.02	36.74	36.74	36.70	36.01	36.74	36.74	36.72	36.55
IRR-PWC	Baseline	1.44	1.59	1.80	2.47	3.73	1.59	1.79	2.42	3.88	1.60	1.84	2.37	3.41
IRR-PWC	Adv $\epsilon = \frac{4}{255}$	35.38	35.40	35.43	35.47	35.52	35.40	35.42	35.47	35.52	35.39	35.42	35.48	35.57
IRR-PWC	Adv $\epsilon = \frac{8}{255}$	35.74	35.75	35.77	35.80	35.84	35.75	35.77	35.80	35.83	35.75	35.77	35.81	35.87
RAFT	Baseline	0.64	3.13	12.04	40.70	120.51	3.16	11.54	43.72	124.46	8.13	15.45	24.92	41.42
RAFT	Adv $\epsilon = \frac{4}{255}$	1.81	3.50	7.63	21.94	49.12	3.40	7.89	21.29	49.72	5.82	9.02	13.89	20.02
RAFT	Adv $\epsilon = \frac{8}{255}$	1.99	3.70	7.88	22.19	48.13	3.69	7.78	21.38	48.53	5.84	9.04	14.10	20.07

H.1 Adversarial Training

In Table 3 we report results from a subset of methods adversarially finetuned (≈10k iterations with a starting learning rate=10^{-6} and same learning rate scheduler as used by the method during training) on the KITTI2015 training dataset using ℓ_∞-norm constrained 3 iterations PGD attack with $\epsilon \in [\frac{4}{255}, \frac{8}{255}]$ and $\alpha = 0.01$ and attacked with ℓ_∞-norm constrained CosPGD, PGD, and BIM attack with $\epsilon \in [\frac{1}{255}, \frac{2}{255}, \frac{4}{255}, \frac{8}{255}]$ and Number of Attack Iterations $\in [3, 5, 10, 20]$.

For finetuning, each mini-batch is adversarially attacked and used to finetune the model.

We observe that adversarial training does, in fact, improve the performance of all considered optical flow methods, but IRR-PWC, against adversarial attacks. For IRR-PWC, we observe a significant drop in clean and adversarial performance when naively finetuned adversarially. For other methods, we observe a gain. This gain in performance is significant for RAFT while losing only a small amount of performance on clean data. However, other methods like FastFlowNet and FlowFormer, where there is a gain in adversarial performance with adversarial finetuning, there is a significant drop in clean performance.

Please note that in this work, image-wide white-box adversarial attacks have been used as a probe for the reliability of the feature representations learned by the model when trained normally. While adversarial training is a known adversarial defense method, using it in this context defeats the purpose of using image-wide white-box adversarial attacks as a probe for reliability.

H.2 Adversarial Attacks

Here we report additional results for all adversarial attacks.

H.2.1 FGSM Attack

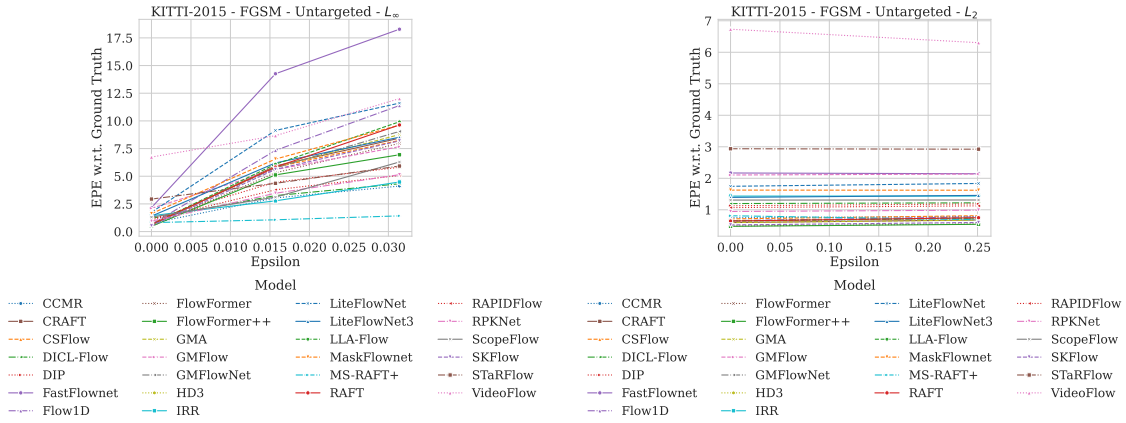

Figure 9: Evaluations for non-targeted FGSM attack under ℓ_∞-norm bound using the KITTI2015 dataset. The attack was optimized w.r.t. the ground truth predictions.

Here we report the evaluations using FGSM attack, both as targeted (both targets: $\overrightarrow{0}$ and $\overrightarrow{-f}$) and non-targeted attacks optimized under the ℓ_∞-norm bound and the ℓ_2-norm bound. For ℓ_∞-norm bound, perturbation budget $\epsilon = \frac{8}{255}$, while for ℓ_2-norm bound, perturbation budget $\epsilon = \frac{64}{255}$.

Attack evaluations include Fig. 9, Fig. 10, Fig. 11, Fig. 12, Fig. 13, Fig. 14, Fig. 15, Fig. 16, Fig. 17, Fig. 18, Fig. 19, Fig. 20, Fig. 21, Fig. 22, and Fig. 23.

H.2.2 BIM Attack

Here we report the evaluations using BIM attack, both as targeted (both targets: $\overrightarrow{0}$ and $\overrightarrow{-f}$) and non-targeted attacks optimized under the ℓ_∞-norm bound and the ℓ_2-norm bound over multiple attack iterations.

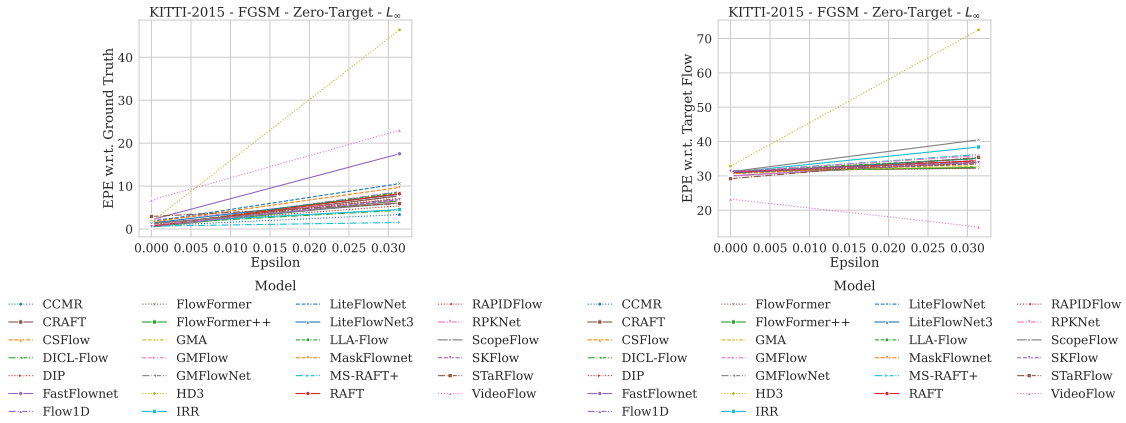

Figure 10: Evaluations for targeted FGSM attack with target $\overrightarrow{0}$ under ℓ_∞-norm bound using the KITTI2015 dataset. The attack was optimized w.r.t. the ground truth predictions.

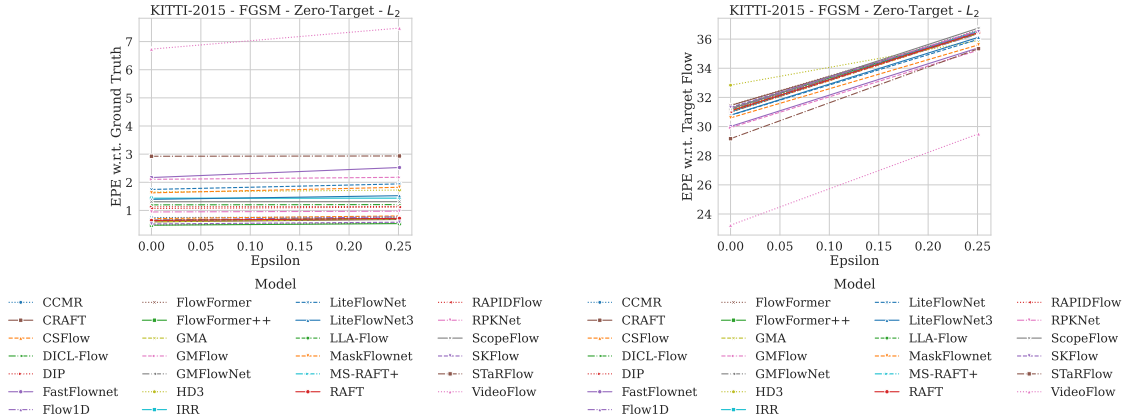

Figure 11: Evaluations for targeted FGSM attack with target $\overrightarrow{0}$ under ℓ_2-norm bound using the KITTI2015 dataset. The attack was optimized w.r.t. the ground truth predictions.

For ℓ_∞-norm bound, perturbation budget $\epsilon = \frac{8}{255}$, and step size α=0.01, while for ℓ_2-norm bound, perturbation budget $\epsilon = \frac{64}{255}$ and step size α=0.1. Attack evaluations include Fig. 24, Fig. 25, Fig. 26, Fig. 27, Fig. 28, Fig. 29, Fig. 30, Fig. 31, Fig. 32, Fig. 33, Fig. 34, Fig. 35, Fig. 36, Fig. 37, and Fig. 38.

H.2.3 PGD Attack

Here we report the evaluations using PGD attack, both as targeted (both targets: $\overrightarrow{0}$ and $\overrightarrow{-f}$) and non-targeted attacks optimized under the ℓ_∞-norm bound and the ℓ_2-norm bound over multiple attack iterations. For ℓ_∞-norm bound, perturbation budget $\epsilon = \frac{8}{255}$, and step size α=0.01, while for ℓ_2-norm bound, perturbation budget $\epsilon = \frac{64}{255}$ and step size α=0.1. Attack evaluations include Fig. 39, Fig. 40, Fig. 41, Fig. 42, Fig. 43, Fig. 44, Fig. 45, Fig. 46, Fig. 47, Fig. 48, Fig. 49, Fig. 50, Fig. 51, Fig. 52, and Fig. 53.

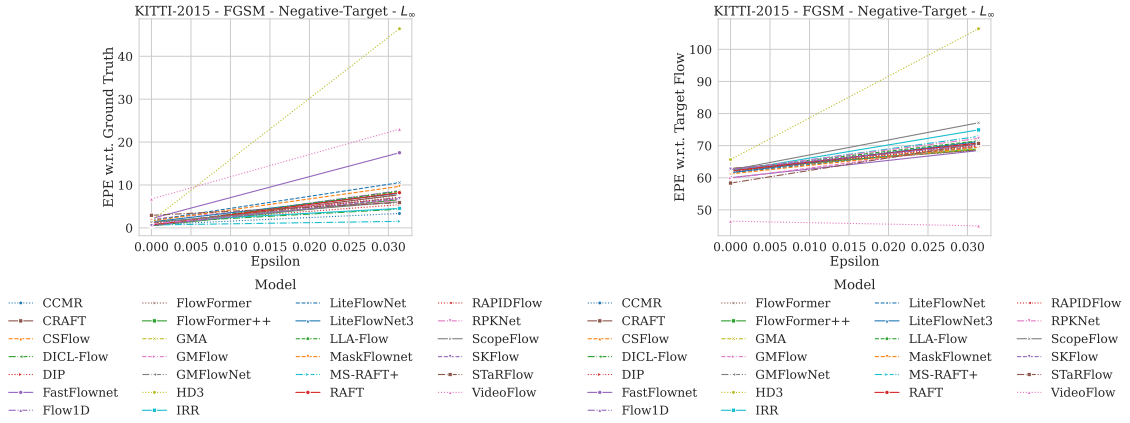

Figure 12: Evaluations for targeted FGSM attack with target $\overrightarrow{-f}$ under ℓ_∞-norm bound using the KITTI2015 dataset. The attack was optimized w.r.t. the ground truth predictions.

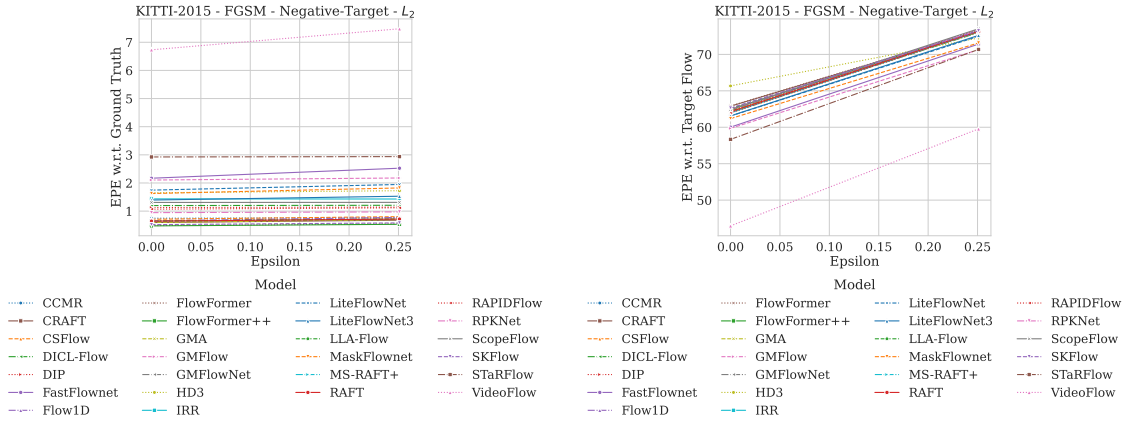

Figure 13: Evaluations for targeted FGSM attack with target $\overrightarrow{-f}$ under ℓ_2-norm bound using the KITTI2015 dataset. The attack was optimized w.r.t. the ground truth predictions.

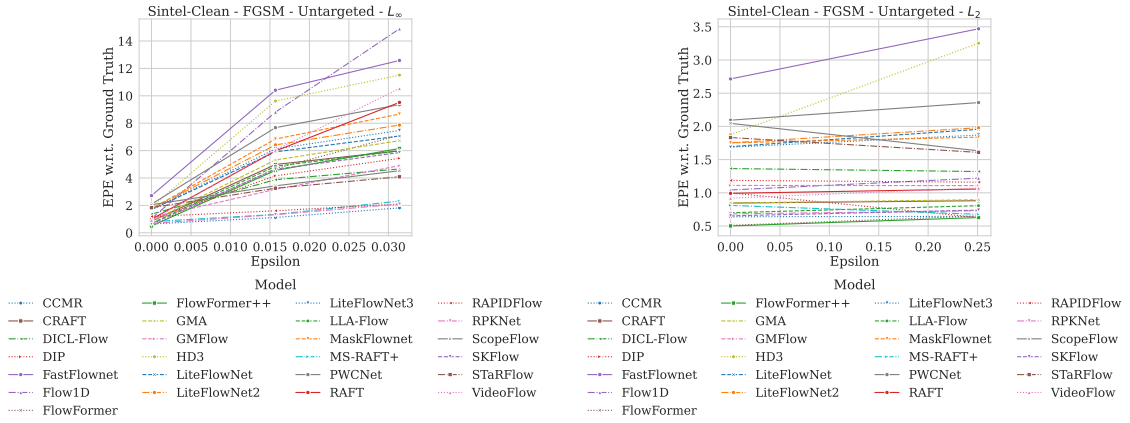

Figure 14: Evaluations for non-targeted FGSM attack under ℓ_∞-norm bound using the MPI Sintel (clean) dataset. The attack was optimized w.r.t. the ground truth predictions.

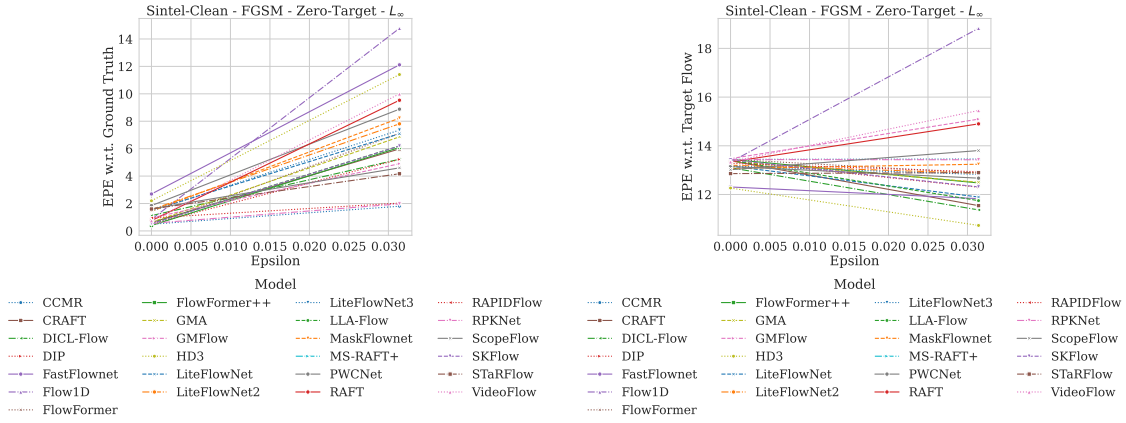

Figure 15: Evaluations for targeted FGSM attack with target $\overrightarrow{0}$ under ℓ_∞-norm bound using the MPI Sintel (clean) dataset. The attack was optimized w.r.t. the ground truth predictions.

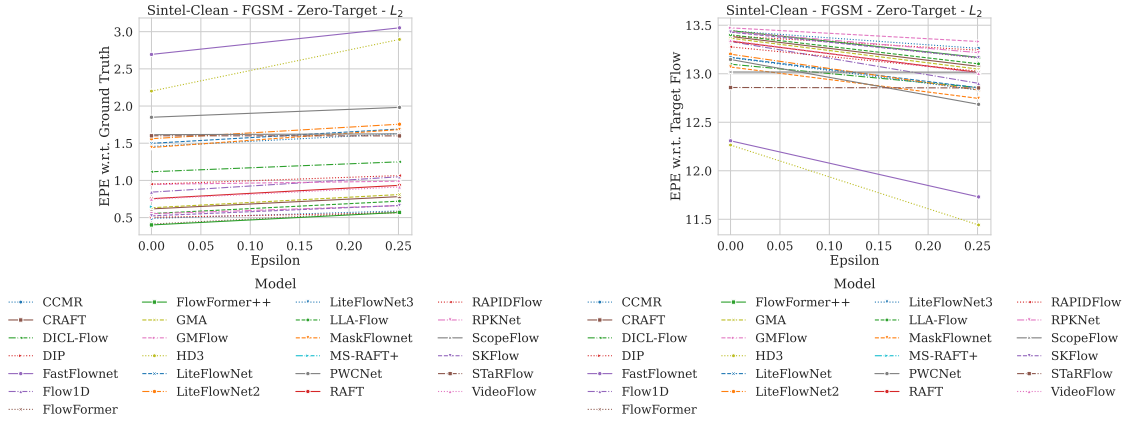

Figure 16: Evaluations for targeted FGSM attack with target $\overrightarrow{0}$ under ℓ_2-norm bound using the MPI Sintel (clean) dataset. The attack was optimized w.r.t. the ground truth predictions.

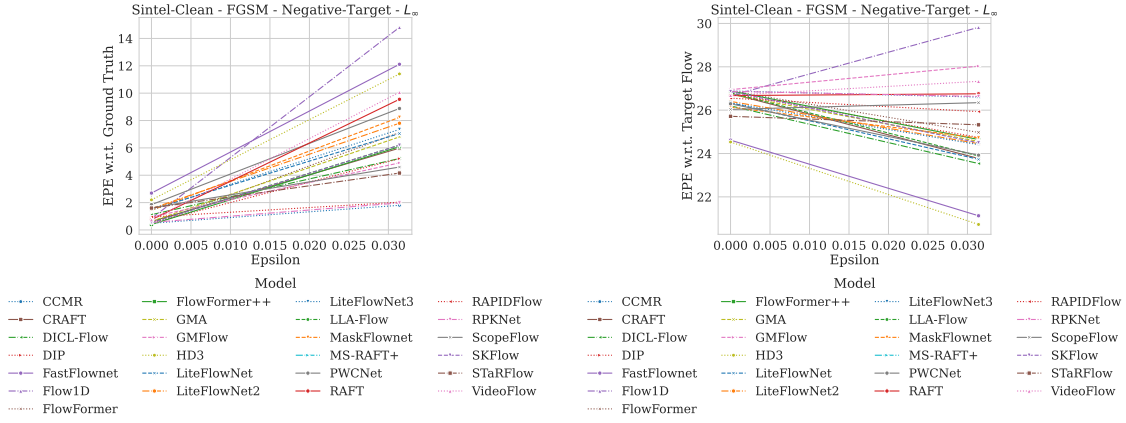

Figure 17: Evaluations for targeted FGSM attack with target $\overrightarrow{-f}$ under ℓ_∞-norm bound using the MPI Sintel (clean) dataset. The attack was optimized w.r.t. the ground truth predictions.

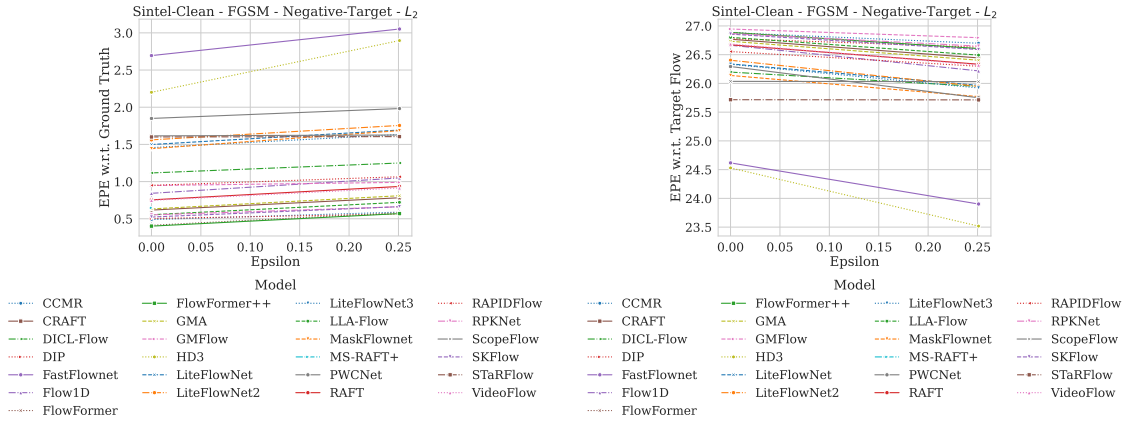

Figure 18: Evaluations for targeted FGSM attack with target $\overrightarrow{-f}$ under ℓ_2-norm bound using the MPI Sintel (clean) dataset. The attack was optimized w.r.t. the ground truth predictions.

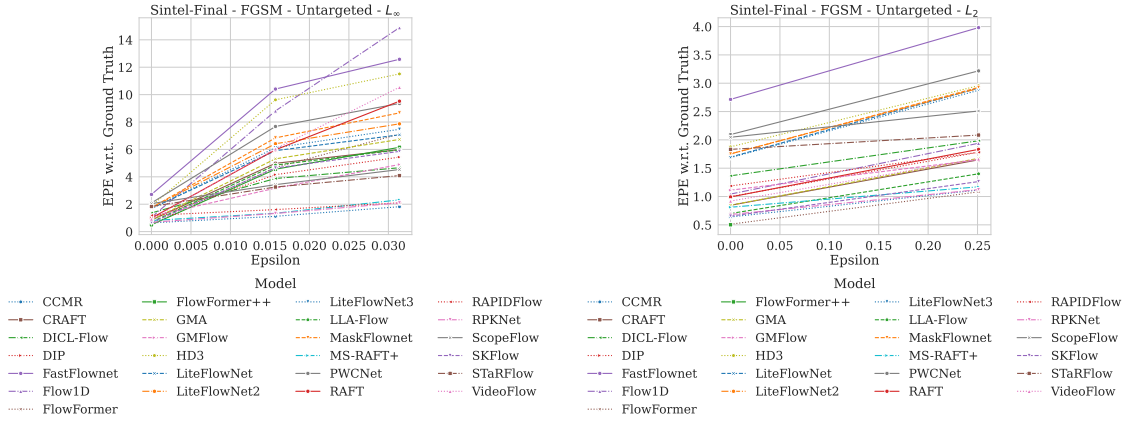

Figure 19: Evaluations for non-targeted FGSM attack under ℓ_∞-norm bound using the MPI Sintel (final) dataset. The attack was optimized w.r.t. the ground truth predictions.

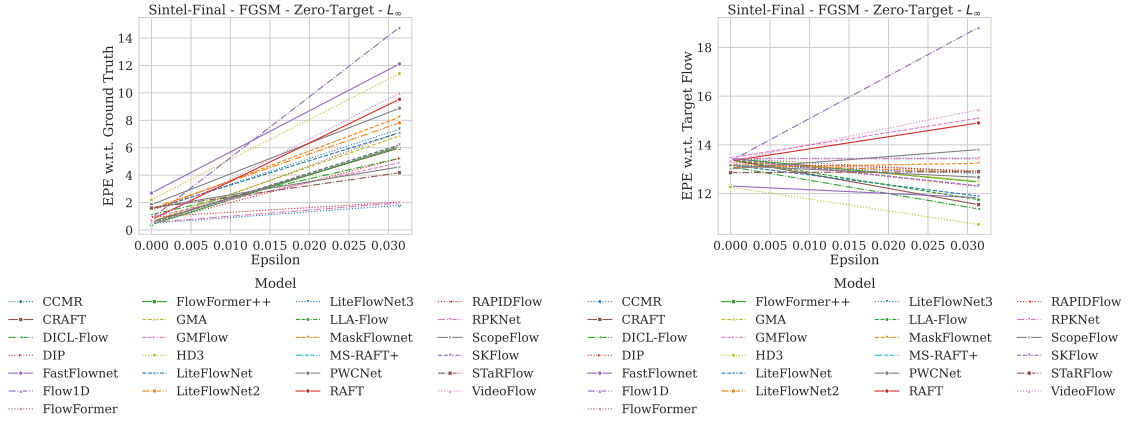

Figure 20: Evaluations for targeted FGSM attack with target $\overrightarrow{0}$ under ℓ_∞-norm bound using the MPI Sintel (final) dataset. The attack was optimized w.r.t. the ground truth predictions.

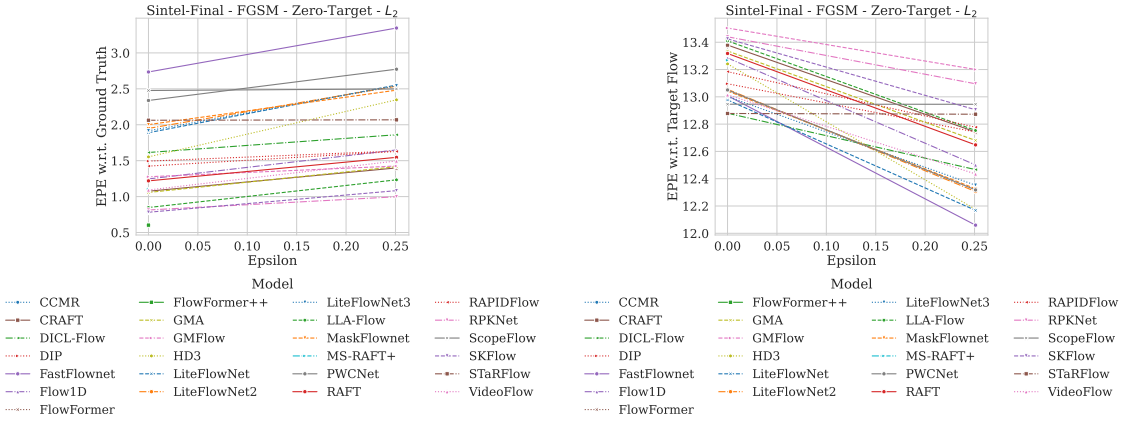

Figure 21: Evaluations for targeted FGSM attack with target $\overrightarrow{0}$ under ℓ_2-norm bound using the MPI Sintel (final) dataset. The attack was optimized w.r.t. the ground truth predictions.

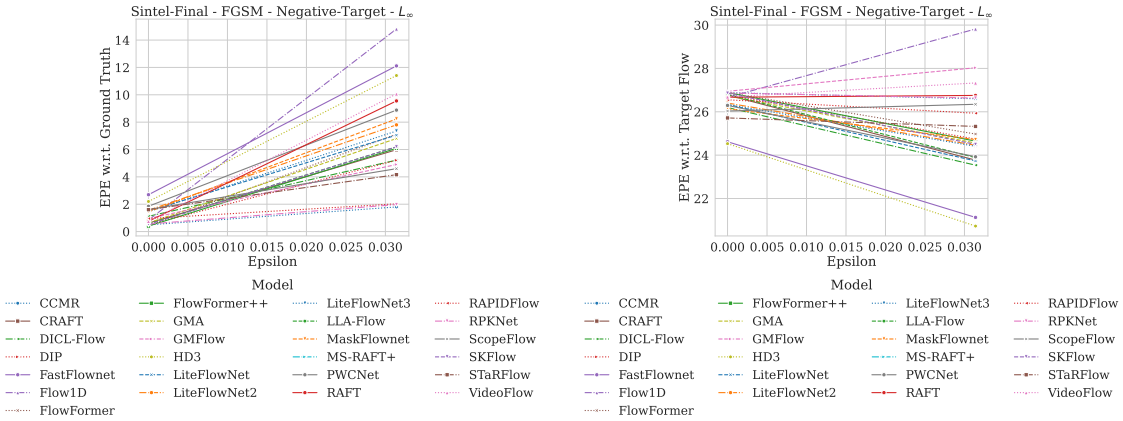

Figure 22: Evaluations for targeted FGSM attack with target $\overrightarrow{-f}$ under ℓ_∞-norm bound using the MPI Sintel (final) dataset. The attack was optimized w.r.t. the ground truth predictions.

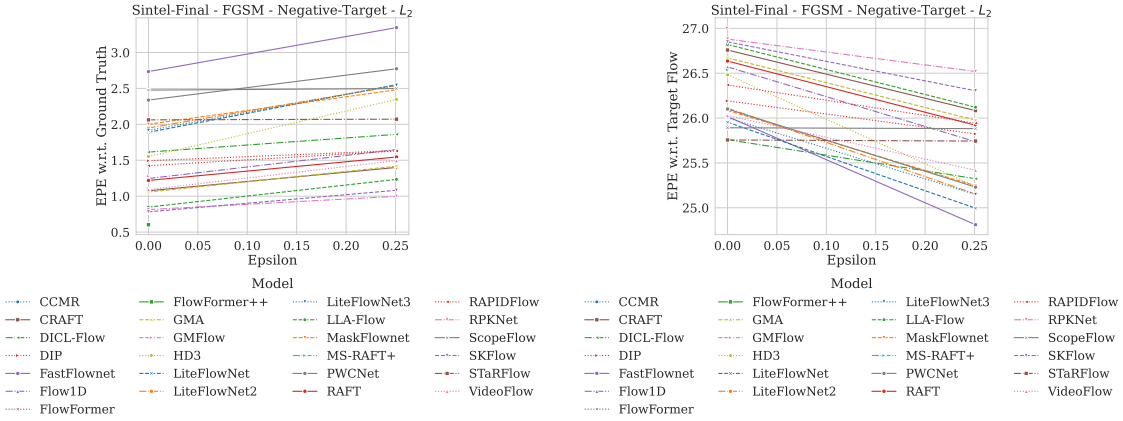

Figure 23: Evaluations for targeted FGSM attack with target $\overrightarrow{-f}$ under ℓ_2-norm bound using the MPI Sintel (final) dataset. The attack was optimized w.r.t. the ground truth predictions.

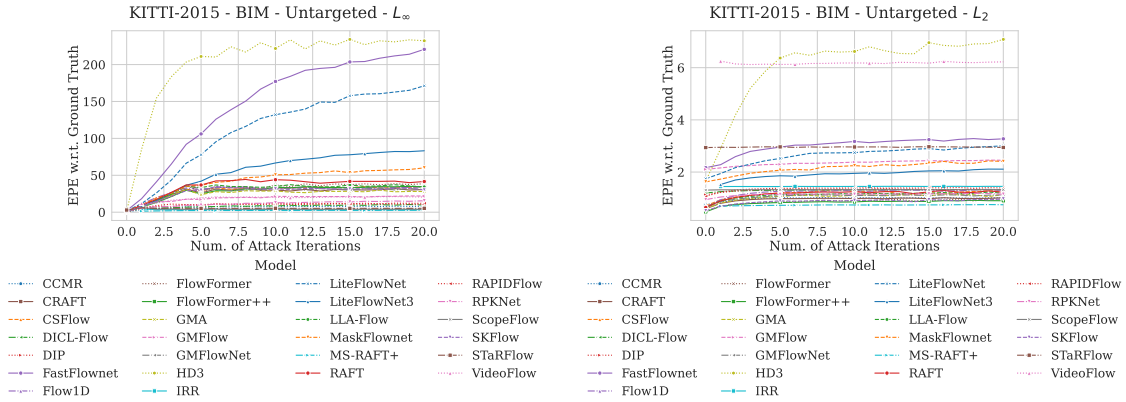

Figure 24: Evaluations for non-targeted BIM attack under ℓ_∞-norm bound using the KITTI2015 dataset. The attack was optimized w.r.t. the ground truth predictions.

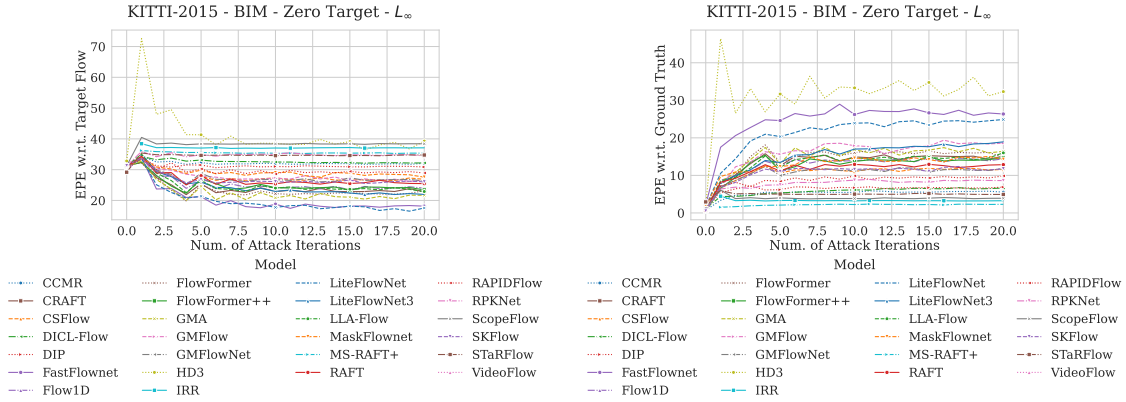

Figure 25: Evaluations for targeted BIM attack with target $\overrightarrow{0}$ under ℓ_∞-norm bound using the KITTI2015 dataset. The attack was optimized w.r.t. the ground truth predictions.

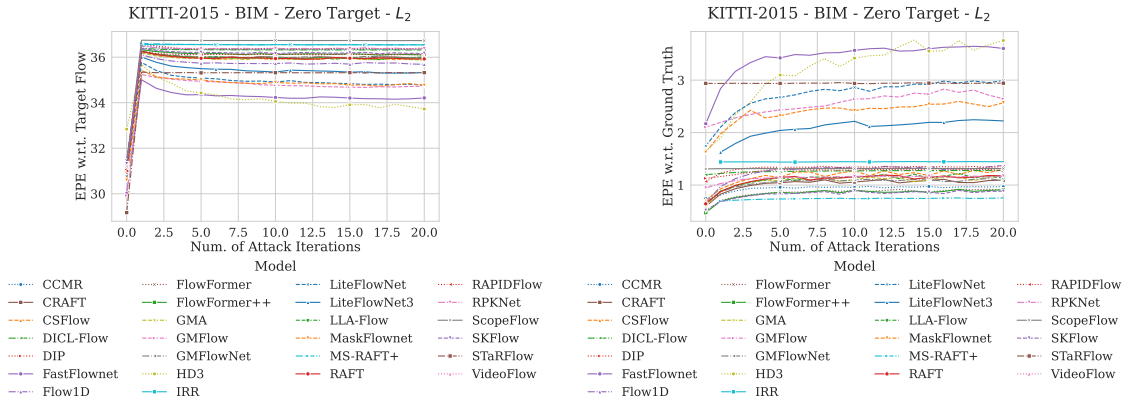

Figure 26: Evaluations for targeted BIM attack with target $\overrightarrow{0}$ under ℓ_2-norm bound using the KITTI2015 dataset. The attack was optimized w.r.t. the ground truth predictions.

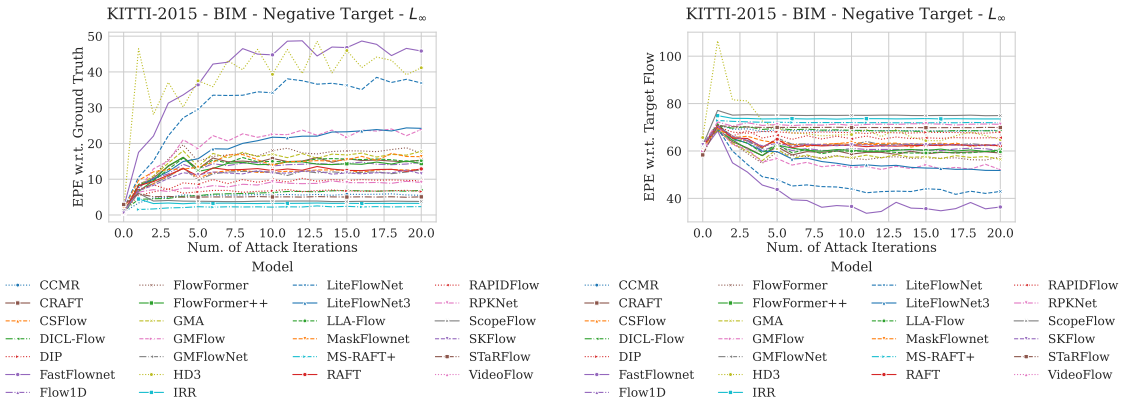

Figure 27: Evaluations for targeted BIM attack with target $\overrightarrow{-f}$ under ℓ_∞-norm bound using the KITTI2015 dataset. The attack was optimized w.r.t. the ground truth predictions.

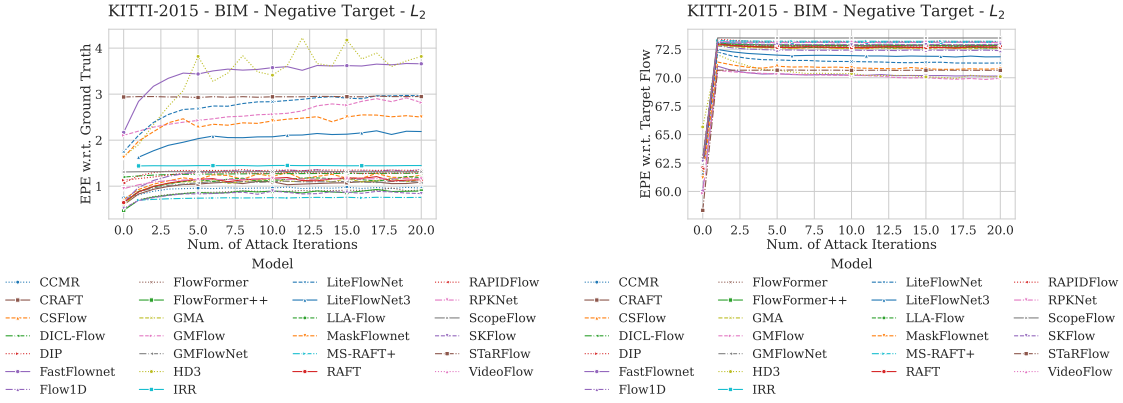

Figure 28: Evaluations for targeted BIM attack with target $\overrightarrow{-f}$ under ℓ_2-norm bound using the KITTI2015 dataset. The attack was optimized w.r.t. the ground truth predictions.

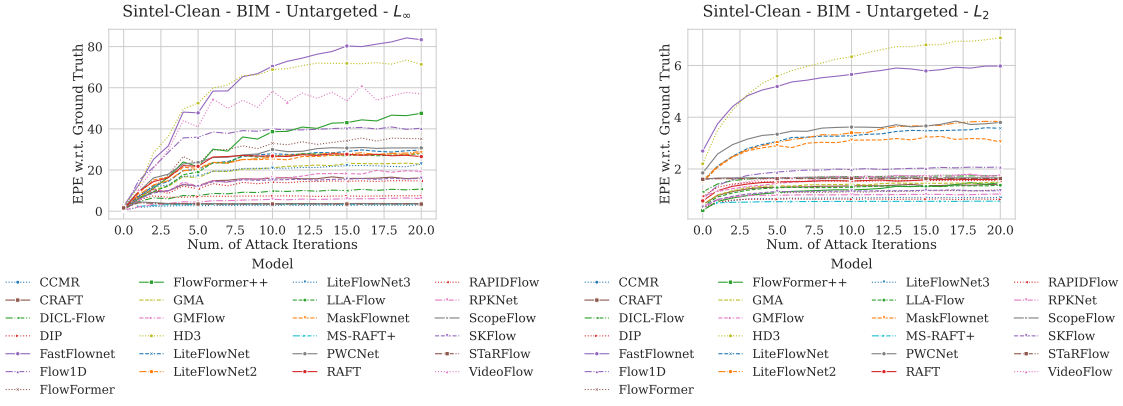

Figure 29: Evaluations for non-targeted BIM attack under ℓ_∞-norm bound using the MPI Sintel (clean) dataset. The attack was optimized w.r.t. the ground truth predictions.

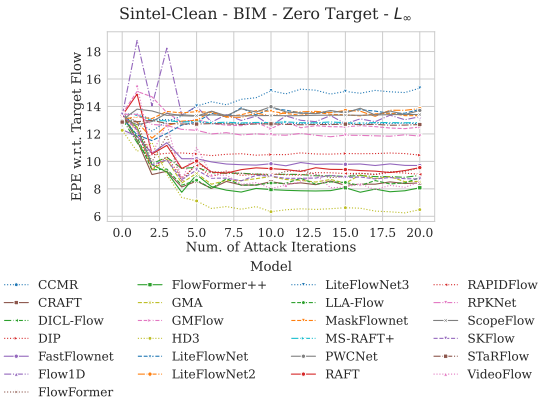

Figure 30: Evaluations for targeted BIM attack with target $\overrightarrow{0}$ under ℓ_∞-norm bound using the MPI Sintel (clean) dataset. The attack was optimized w.r.t. the ground truth predictions.

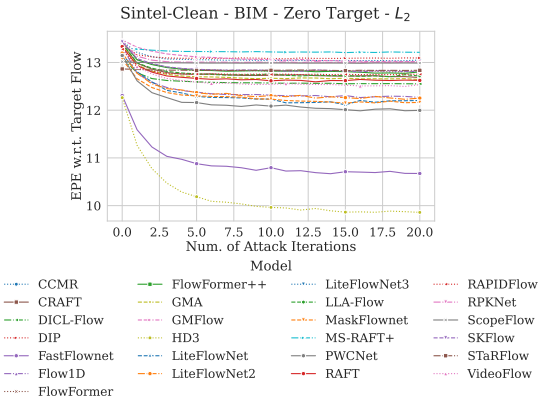

Figure 31: Evaluations for targeted BIM attack with target $\overrightarrow{0}$ under ℓ_2-norm bound using the MPI Sintel (clean) dataset. The attack was optimized w.r.t. the ground truth predictions.

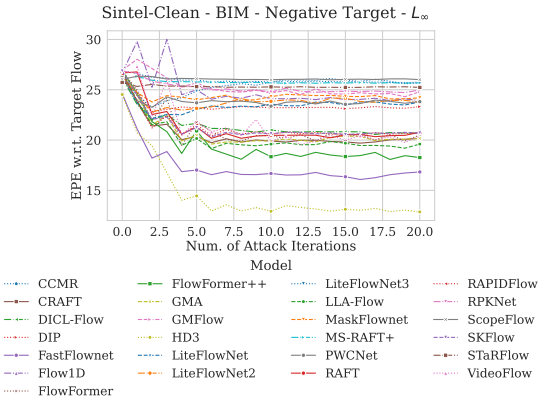

Figure 32: Evaluations for targeted BIM attack with target $\overrightarrow{-f}$ under ℓ_∞-norm bound using the MPI Sintel (clean) dataset. The attack was optimized w.r.t. the ground truth predictions.

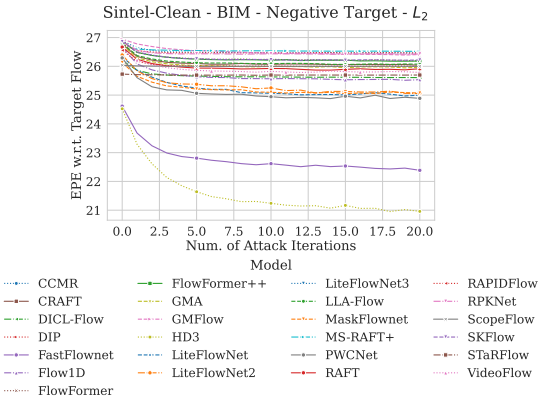

Figure 33: Evaluations for targeted BIM attack with target $\overrightarrow{-f}$ under ℓ_2-norm bound using the MPI Sintel (clean) dataset. The attack was optimized w.r.t. the ground truth predictions.

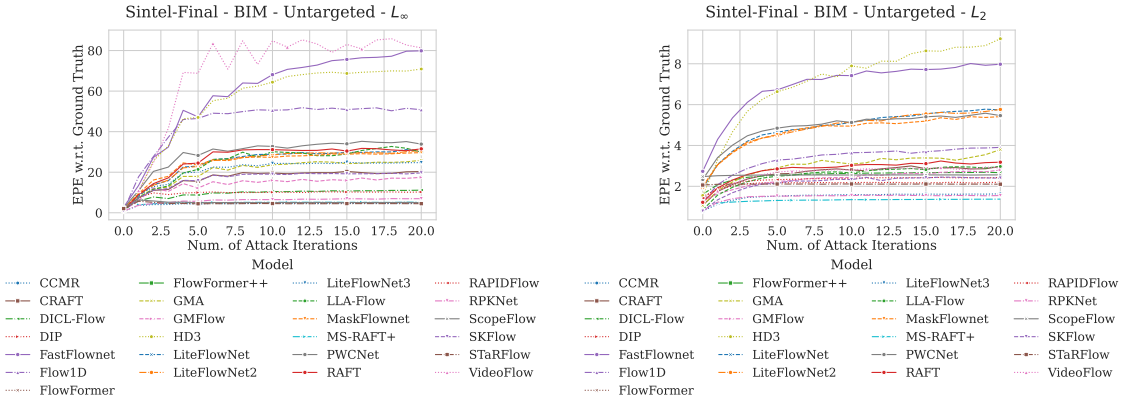

Figure 34: Evaluations for non-targeted BIM attack under ℓ_∞-norm bound using the MPI Sintel (final) dataset. The attack was optimized w.r.t. the ground truth predictions.

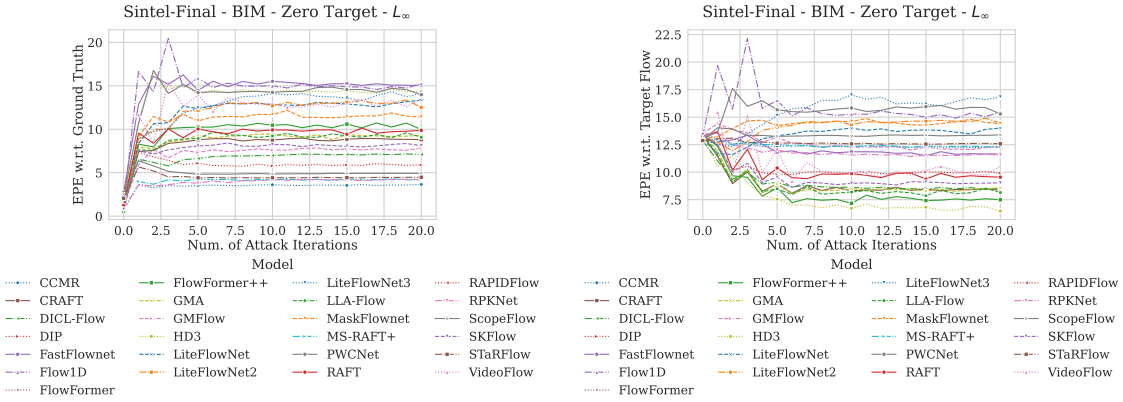

Figure 35: Evaluations for targeted BIM attack with target $\overrightarrow{0}$ under ℓ_∞-norm bound using the MPI Sintel (final) dataset. The attack was optimized w.r.t. the ground truth predictions.

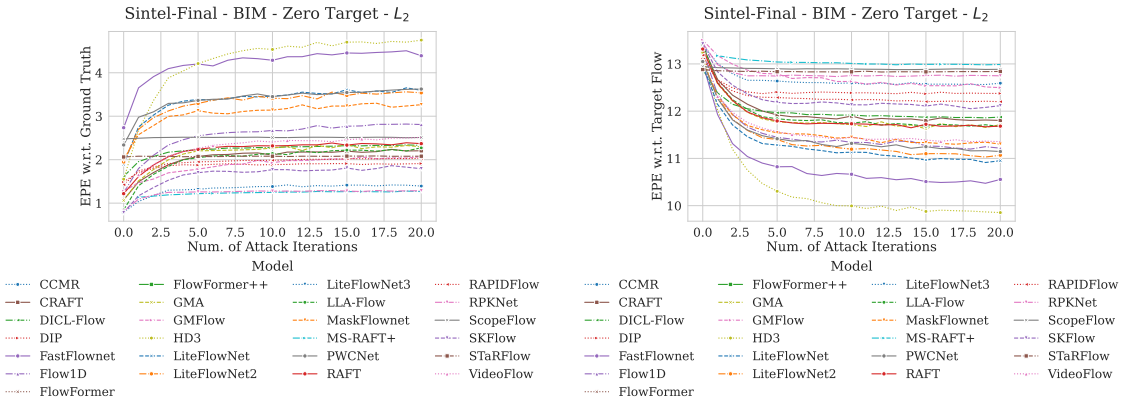

Figure 36: Evaluations for targeted BIM attack with target $\overrightarrow{0}$ under ℓ_2-norm bound using the MPI Sintel (final) dataset. The attack was optimized w.r.t. the ground truth predictions.

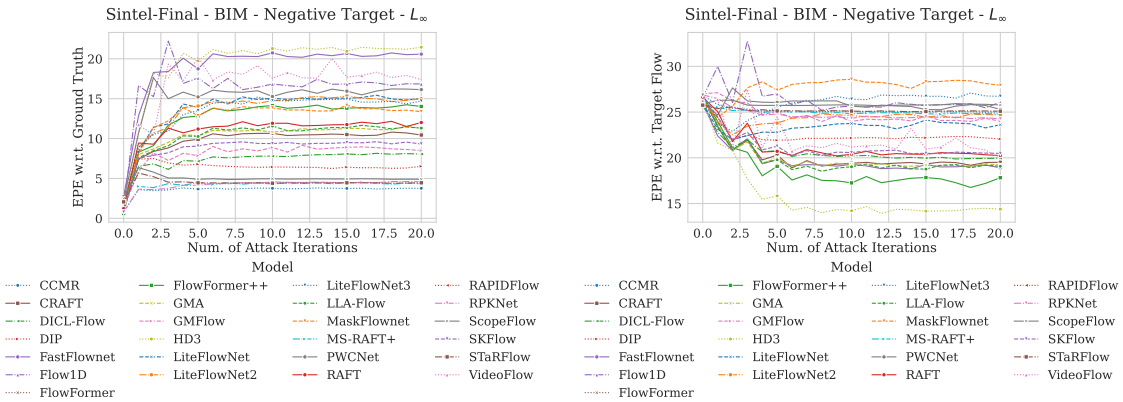

Figure 37: Evaluations for targeted BIM attack with target $\overrightarrow{-f}$ under ℓ_∞-norm bound using the MPI Sintel (final) dataset. The attack was optimized w.r.t. the ground truth predictions.

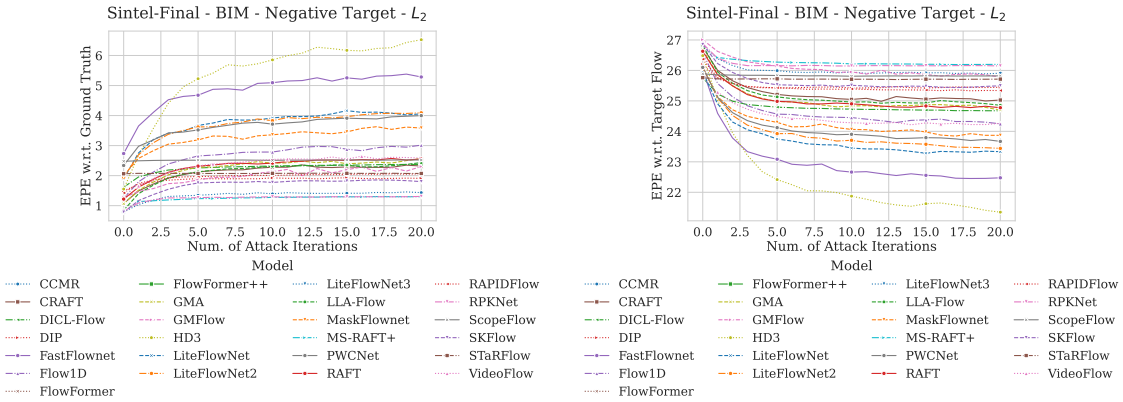

Figure 38: Evaluations for targeted BIM attack with target $\overrightarrow{-f}$ under ℓ_2-norm bound using the MPI Sintel (final) dataset. The attack was optimized w.r.t. the ground truth predictions.

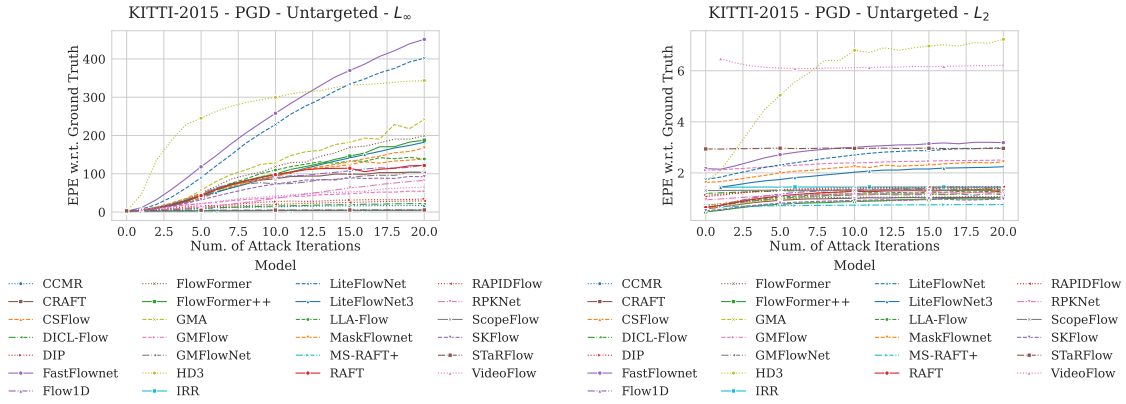

Figure 39: Evaluations for non-targeted PGD attack under ℓ_∞-norm bound using the KITTI2015 dataset. The attack was optimized w.r.t. the ground truth predictions.

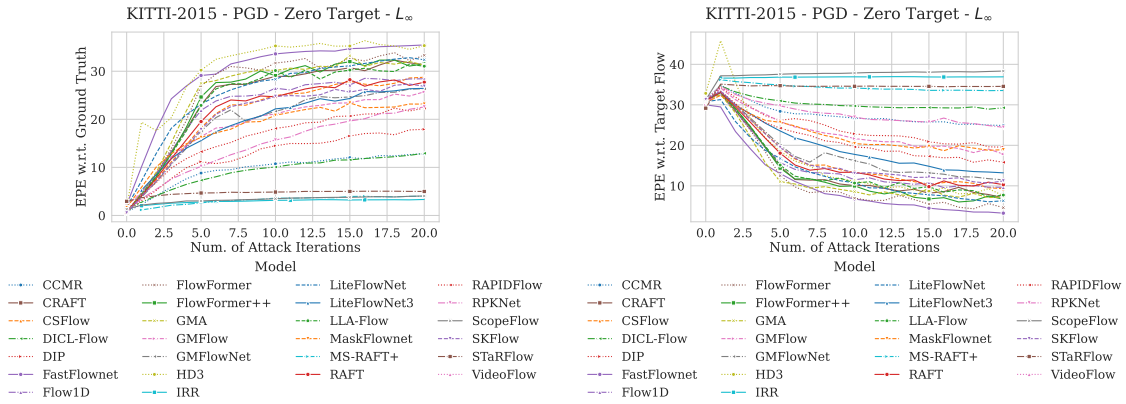

Figure 40: Evaluations for targeted PGD attack with target $\overrightarrow{0}$ under ℓ_∞-norm bound using the KITTI2015 dataset. The attack was optimized w.r.t. the ground truth predictions.

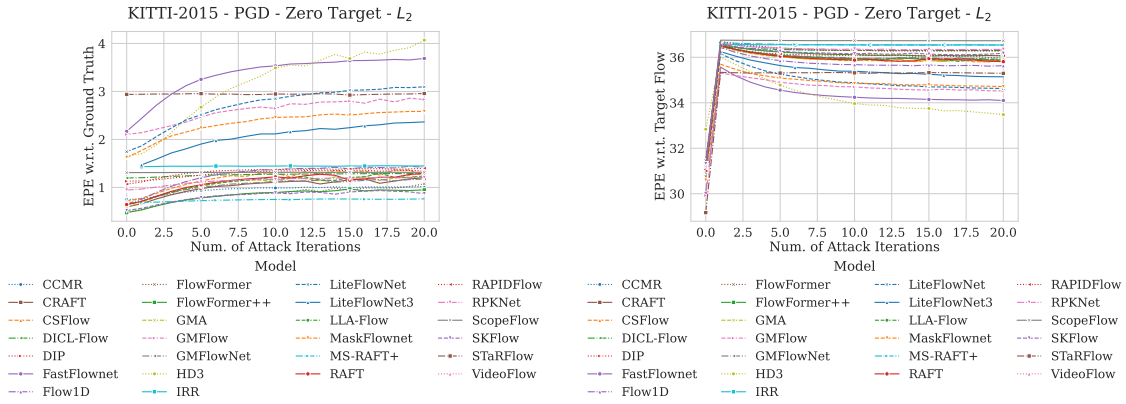

Figure 41: Evaluations for targeted PGD attack with target $\overrightarrow{0}$ under ℓ_2-norm bound using the KITTI2015 dataset. The attack was optimized w.r.t. the ground truth predictions.

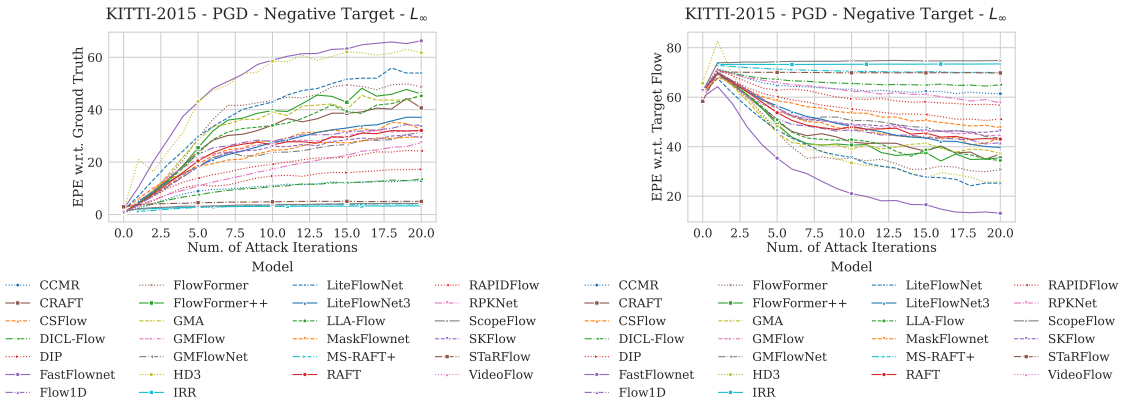

Figure 42: Evaluations for targeted PGD attack with target $\overrightarrow{-f}$ under ℓ_∞-norm bound using the KITTI2015 dataset. The attack was optimized w.r.t. the ground truth predictions.

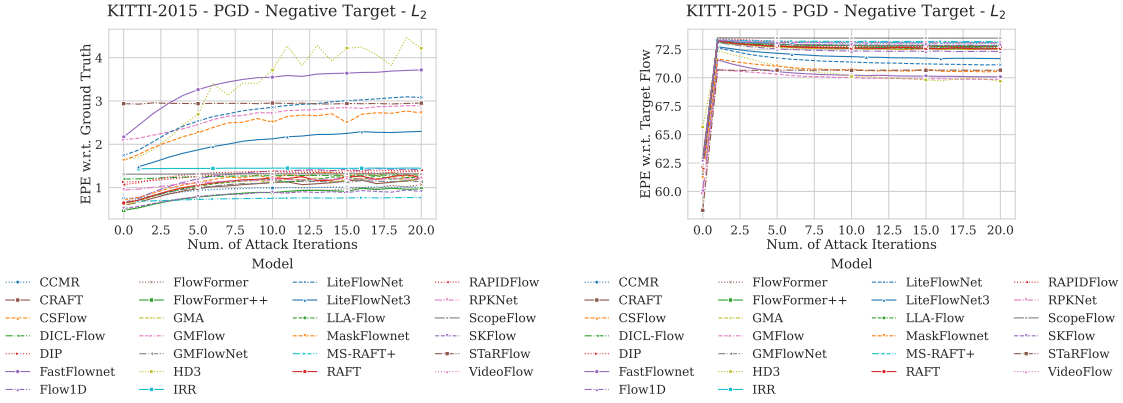

Figure 43: Evaluations for targeted PGD attack with target $\overrightarrow{-f}$ under ℓ_2-norm bound using the KITTI2015 dataset. The attack was optimized w.r.t. the ground truth predictions.

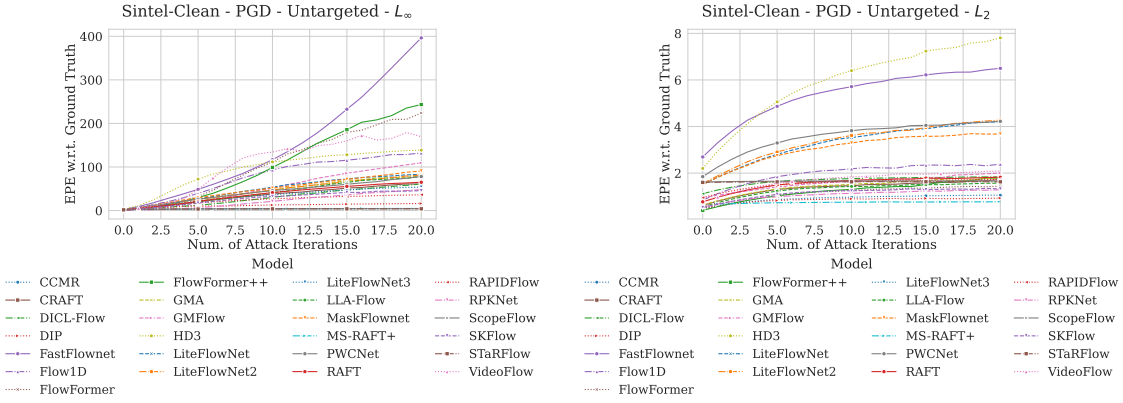

Figure 44: Evaluations for non-targeted PGD attack under ℓ_∞-norm bound using the MPI Sintel (clean) dataset. The attack was optimized w.r.t. the ground truth predictions.

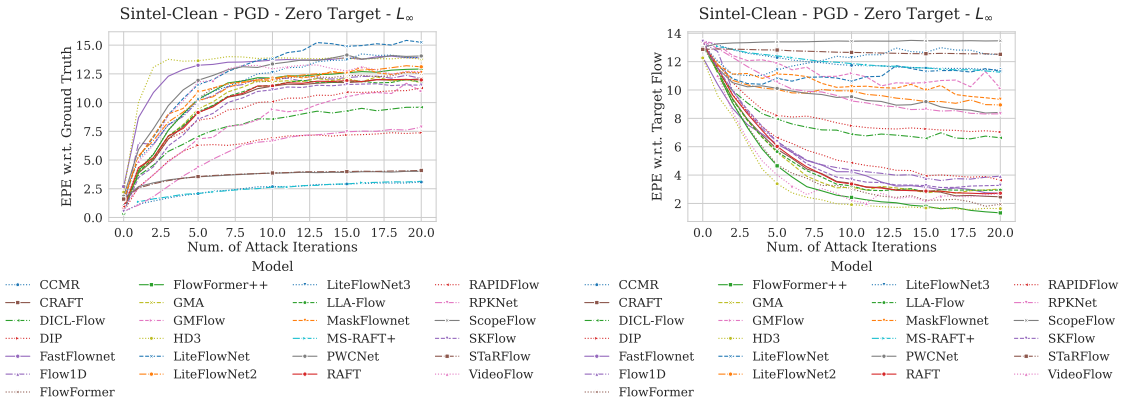

Figure 45: Evaluations for targeted PGD attack with target $\overrightarrow{0}$ under ℓ_∞-norm bound using the MPI Sintel (clean) dataset. The attack was optimized w.r.t. the ground truth predictions.

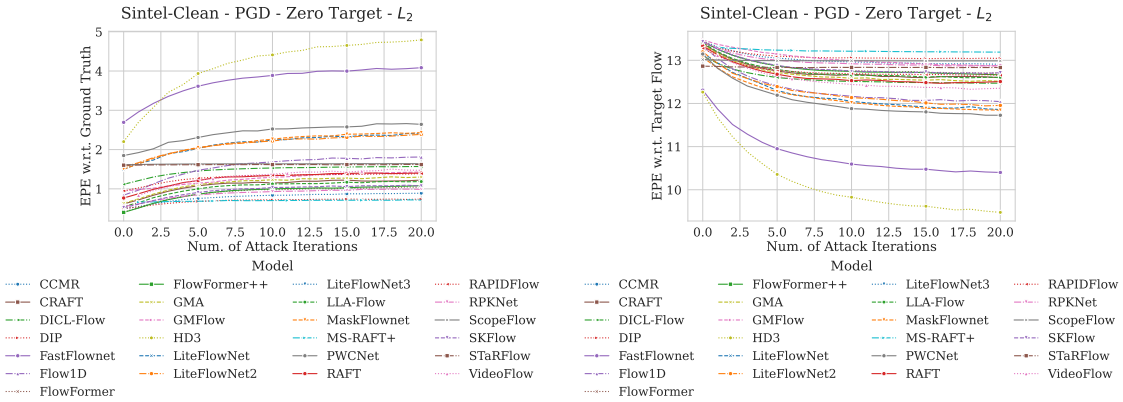

Figure 46: Evaluations for targeted PGD attack with target $\overrightarrow{0}$ under ℓ_2-norm bound using the MPI Sintel (clean) dataset. The attack was optimized w.r.t. the ground truth predictions.

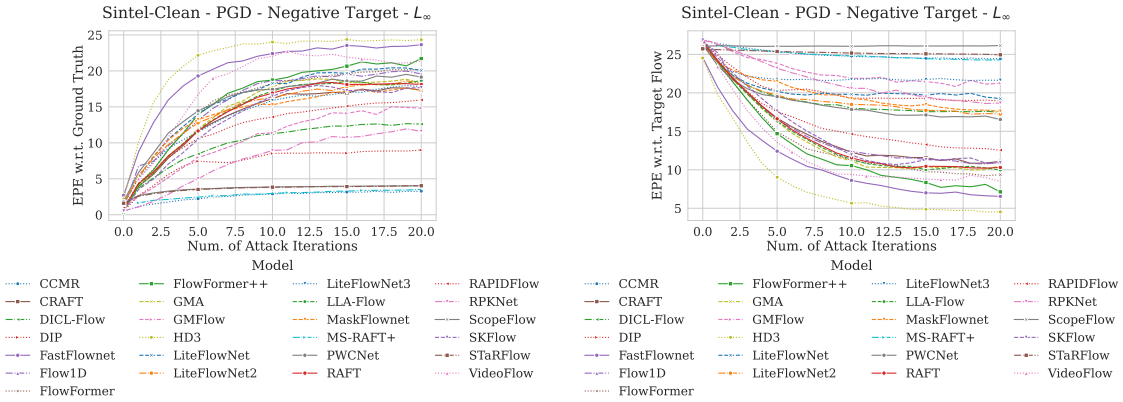

Figure 47: Evaluations for targeted PGD attack with target $\overrightarrow{-f}$ under ℓ_∞-norm bound using the MPI Sintel (clean) dataset. The attack was optimized w.r.t. the ground truth predictions.

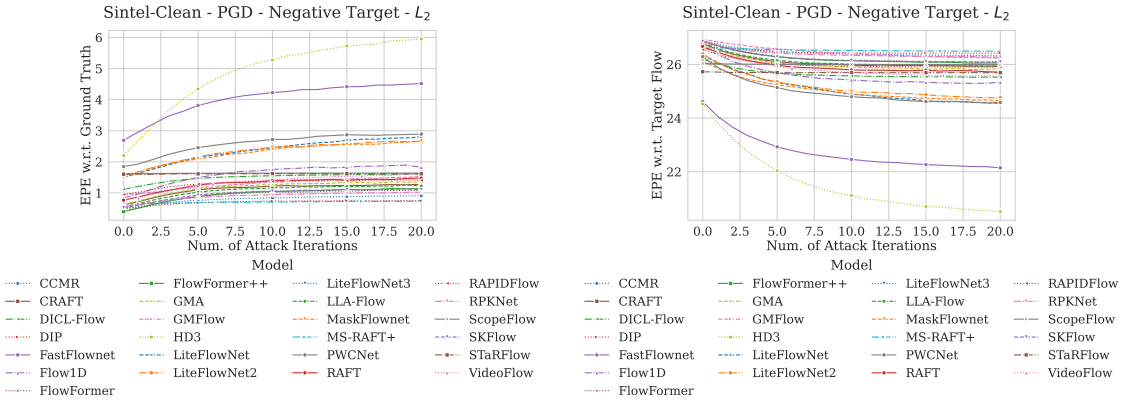

Figure 48: Evaluations for targeted PGD attack with target $-\overrightarrow{f}$ under ℓ_2-norm bound using the MPI Sintel (clean) dataset. The attack was optimized w.r.t. the ground truth predictions.

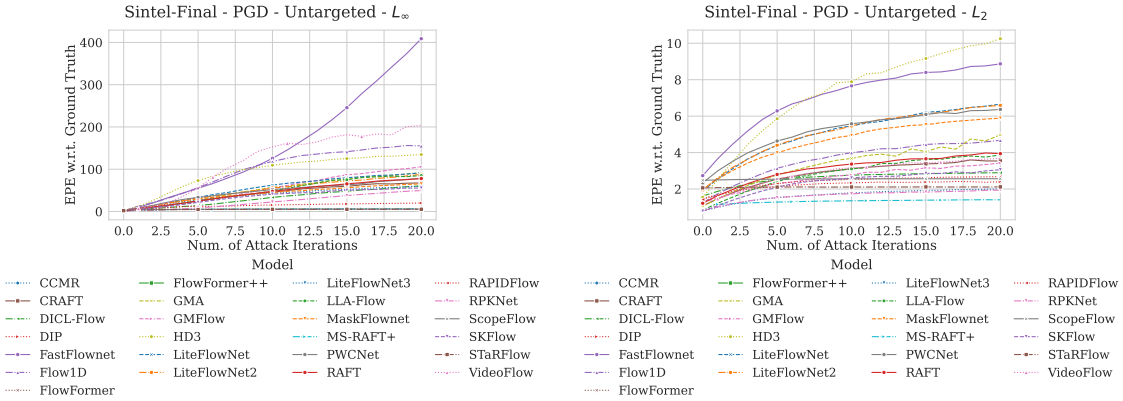

Figure 49: Evaluations for non-targeted PGD attack under ℓ_∞-norm bound using the MPI Sintel (final) dataset. The attack was optimized w.r.t. the ground truth predictions.

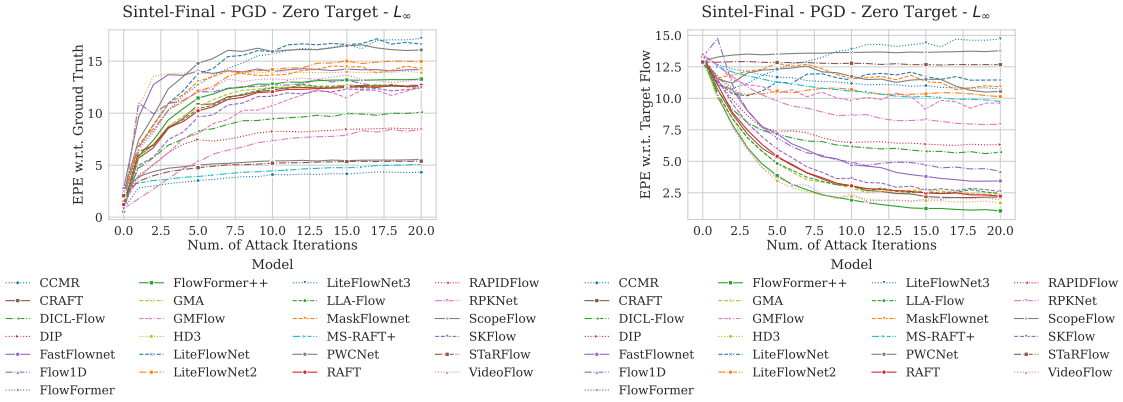

Figure 50: Evaluations for targeted PGD attack with target $\overrightarrow{0}$ under ℓ_∞-norm bound using the MPI Sintel (final) dataset. The attack was optimized w.r.t. the ground truth predictions.

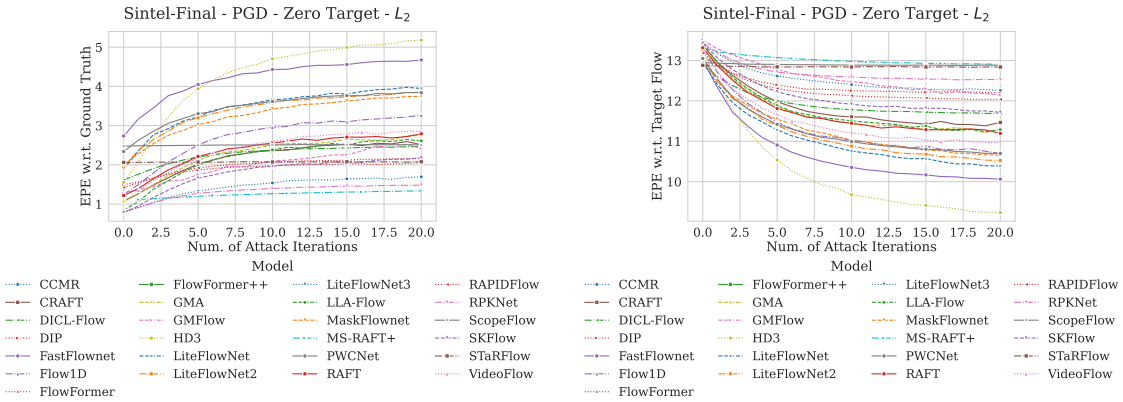

Figure 51: Evaluations for targeted PGD attack with target $\overrightarrow{0}$ under ℓ_2-norm bound using the MPI Sintel (final) dataset. The attack was optimized w.r.t. the ground truth predictions.

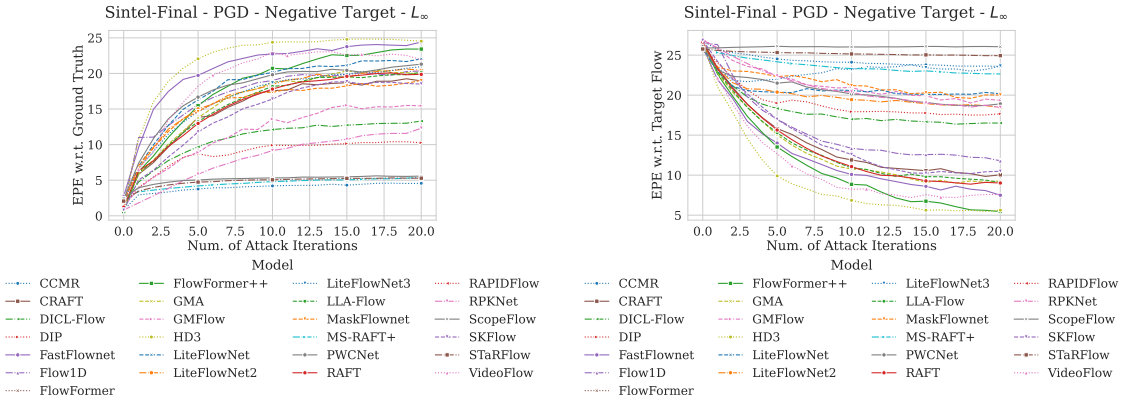

Figure 52: Evaluations for targeted PGD attack with target $\overrightarrow{-f}$ under ℓ_∞-norm bound using the MPI Sintel (final) dataset. The attack was optimized w.r.t. the ground truth predictions.

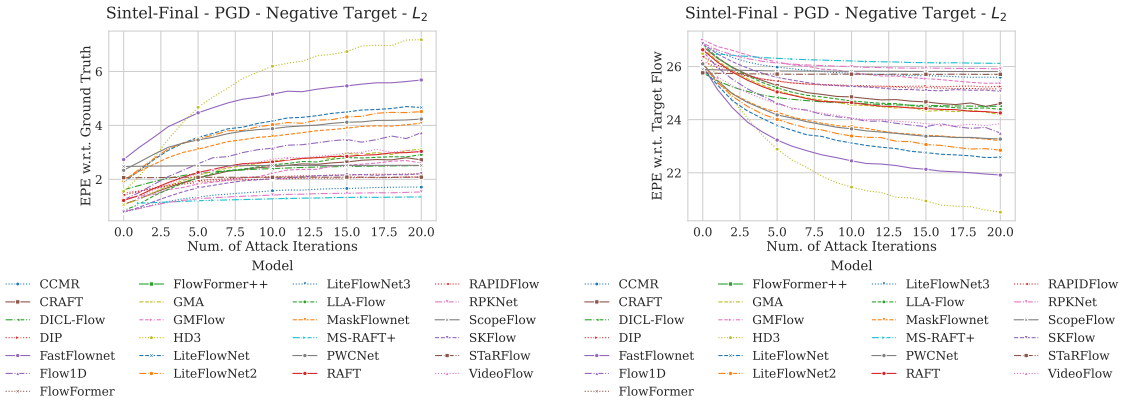

Figure 53: Evaluations for targeted PGD attack with target $\overrightarrow{-f}$ under ℓ_2-norm bound using the MPI Sintel (final) dataset. The attack was optimized w.r.t. the ground truth predictions.

H.2.4 CosPGD Attack

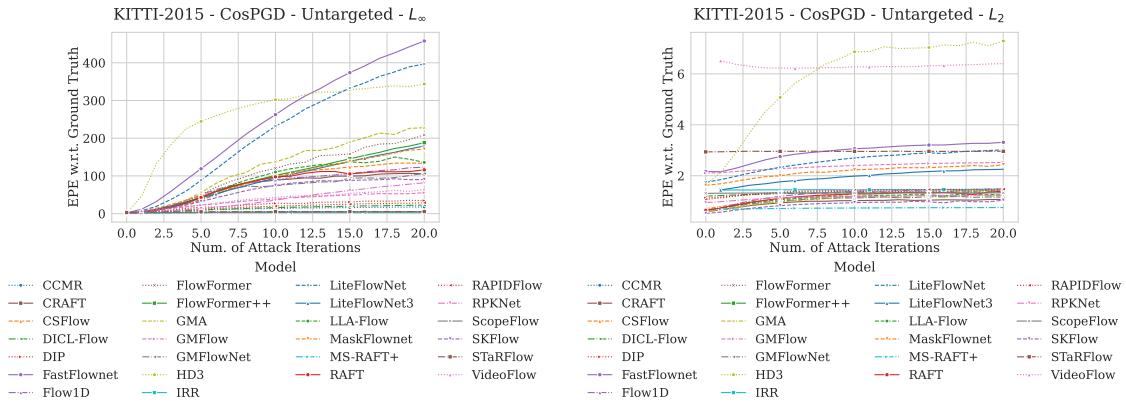

Figure 54: Evaluations for non-targeted CosPGD attack under ℓ_∞-norm bound using the KITTI2015 dataset. The attack was optimized w.r.t. the ground truth predictions.

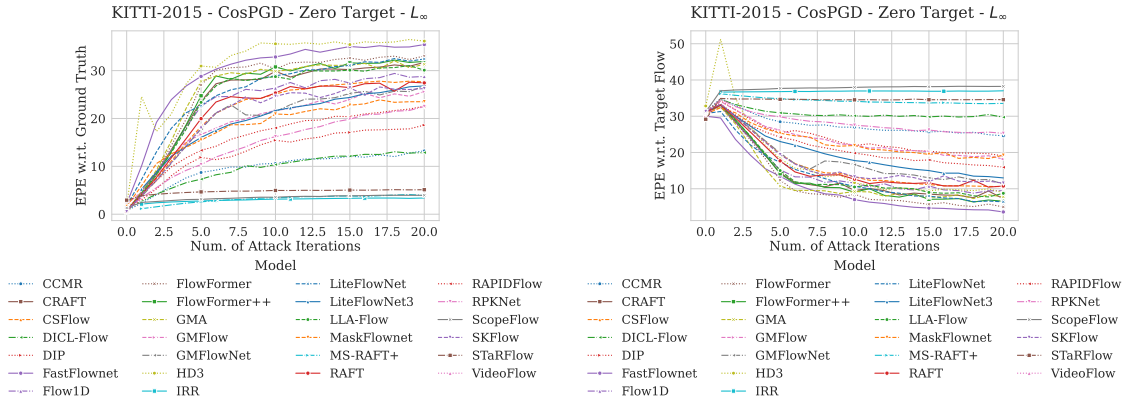

Figure 55: Evaluations for targeted CosPGD attack with target $\overrightarrow{0}$ under ℓ_∞-norm bound using the KITTI2015 dataset. The attack was optimized w.r.t. the ground truth predictions.

Here we report the evaluations using CosPGD attack, both as targeted (both targets: $\overrightarrow{0}$ and $\overrightarrow{-f}$) and non-targeted attacks optimized under the ℓ_∞-norm bound and the ℓ_2-norm bound over multiple attack iterations. For ℓ_∞-norm bound, perturbation budget $\epsilon = \frac{8}{255}$, and step size α=0.01, while for ℓ_2-norm bound, perturbation budget $\epsilon = \frac{64}{255}$ and step size α=0.1. Attack evaluations include Fig. 54, Fig. 55, Fig. 56, Fig. 57, Fig. 58, Fig. 59, Fig. 60, Fig. 61, Fig. 62, Fig. 63, Fig. 64, Fig. 65, Fig. 66, Fig. 67, and Fig. 68.

H.2.5 PCFA Attack

Here we report the evaluations using PCFA attack, as targeted (both targets: $\overrightarrow{0}$ and $\overrightarrow{-f}$) optimized under the ℓ_2-norm bound over multiple attack iterations. Here the perturbation budget $\epsilon = 0.05$ and step size $\alpha = 1e-7$. Attack evaluations include Fig. 69 and Fig. 70.

H.2.6 Adversarial Weather Attack

Here we report the evaluations using different Adversarial Weather, both as targeted (both targets: $\overrightarrow{0}$ and $\overrightarrow{-f}$) and non-targeted attacks. Attack evaluations include Fig. 71, Fig. 72, Fig. 73 and Fig. 74.

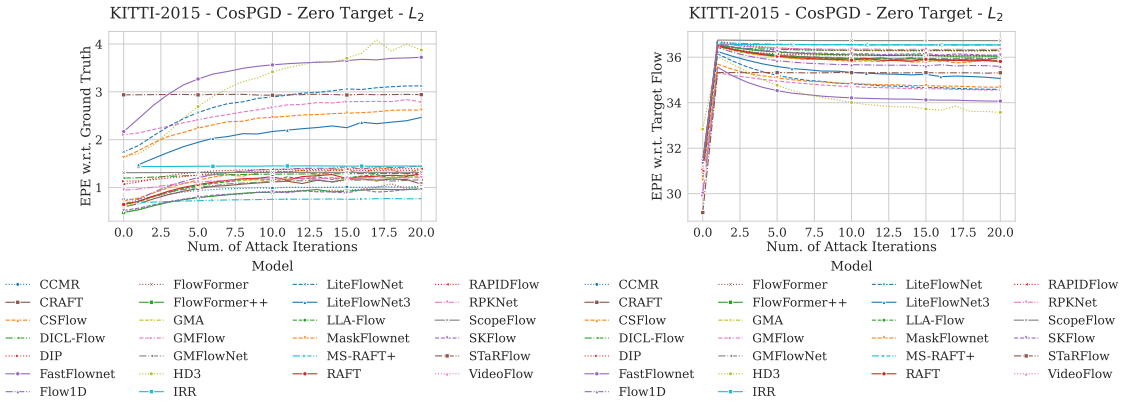

Figure 56: Evaluations for targeted CosPGD attack with target $\overrightarrow{0}$ under ℓ_2-norm bound using the KITTI2015 dataset. The attack was optimized w.r.t. the ground truth predictions.

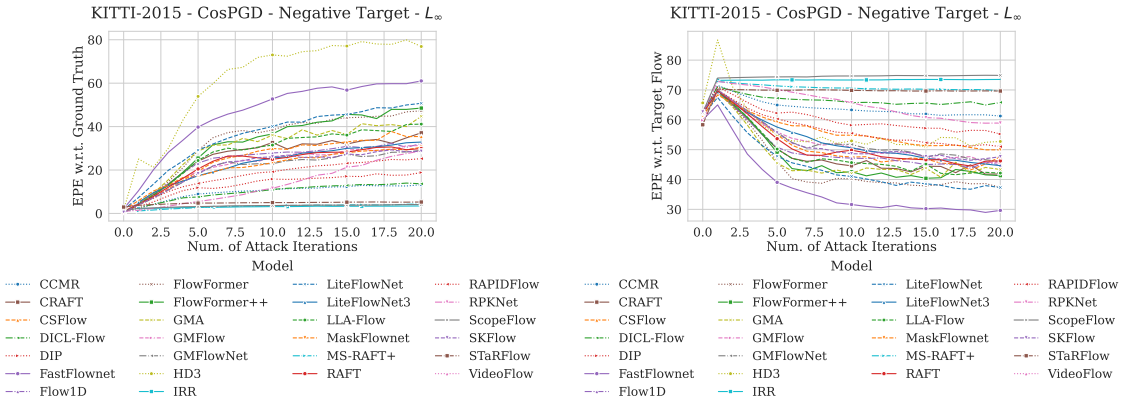

Figure 57: Evaluations for targeted CosPGD attack with target $\overrightarrow{-f}$ under ℓ_∞-norm bound using the KITTI2015 dataset. The attack was optimized w.r.t. the ground truth predictions.

H.3 Common Corruptions Overview

Following, we provide an overview of the performance over all corruptions. This is reported in Fig. 75.

H.4 2D Common Corruptions

Following, we report additional results for 2D Common Corruptions.

H.4.1 Semi-Supervised And Self-Supervised optical Flow Methods

Following, we evaluate the generalization capabilities of semi-supervised Im et al. (2022) and self-supervised Huang et al. (2023) optical flow methods, using 2D Common Corruptions. We take a common architecture, RAFT, for the results to be comparable. We report our results in Table 4. We observe that pretraining on the AutoFlow Huang et al. (2023) dataset provides better generalization capabilities to the RAFT model, however, it lowers its performance on the clean data. Whereas, the semi-supervised method Flow Supervisor Im et al. (2022) provides better or comparable generalization to RAFT on all common corruptions except Snow and Frost, leading to a worse mean performance against corruptions. Please note, we do not observe a significant difference in performance for AutoFlow checkpoints pretrained only on their dataset and the checkpoint finetuned for KITTI2015, except that the "only pretrained" checkpoint, slightly

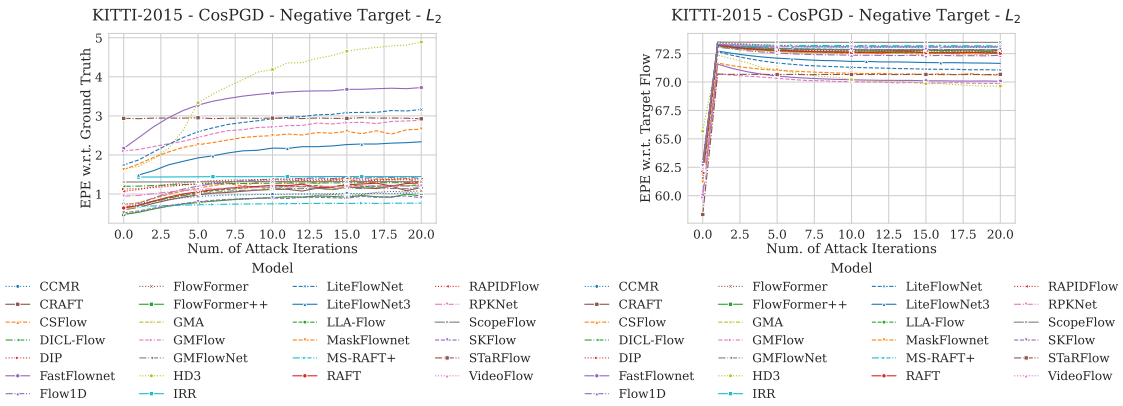

Figure 58: Evaluations for targeted CosPGD attack with target $\overrightarrow{-f}$ under ℓ_2-norm bound using the KITTI2015 dataset. The attack was optimized w.r.t. the ground truth predictions.

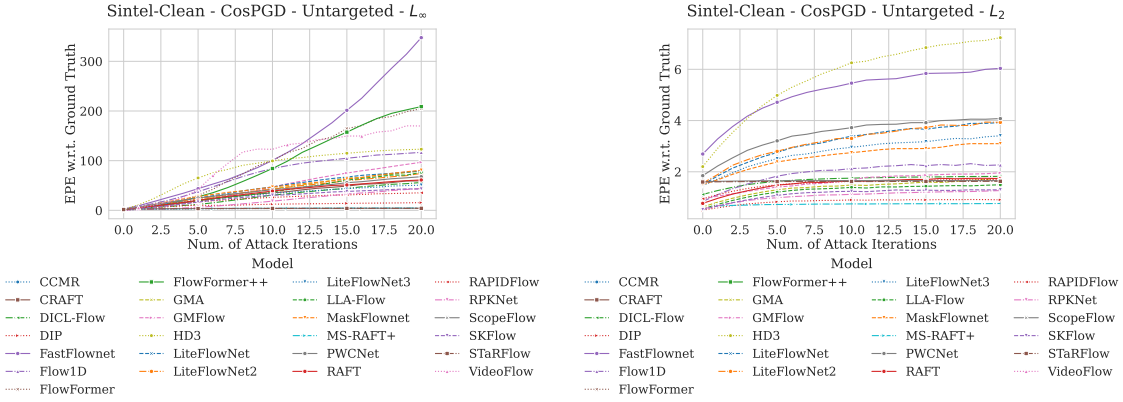

Figure 59: Evaluations for non-targeted CosPGD attack under ℓ_∞-norm bound using the MPI Sintel (clean) dataset. The attack was optimized w.r.t. the ground truth predictions.

but significantly outperforms the checkpoint finetuned on KITTI2015. We suspect that the checkpoints provided are incorrect or mislabeled. Thus, we recommend caution when interpreting these results.

H.4.2 Benchmarking Results

Here we report evaluations using different 2D common corruptions over all considered datasets. OOD Robustness evaluations with 2D Common Corruptions include Fig. 76, Fig. 77 and Fig. 78.

H.5 3D Common Corruptions

Here we report evaluations using different considered 3D common corruptions over all considered datasets. OOD Robustness evaluations with 3D Common Corruptions include Fig. 79, Fig. 80 and Fig. 81.

I Initial Prototype Of The Future Website

In Figure 82 we share a screenshot from our prototype website currently under work, which would help better understand the metrics. In this screenshot, the methods are ranked based on their EPE w.r.t. the ground truth flow under non-targeted CosPGD attack at 20 attack iterations under the ℓ_∞-norm bound (lower means the method is more robust), evaluated using the KITTI2015 dataset. We are currently designing it

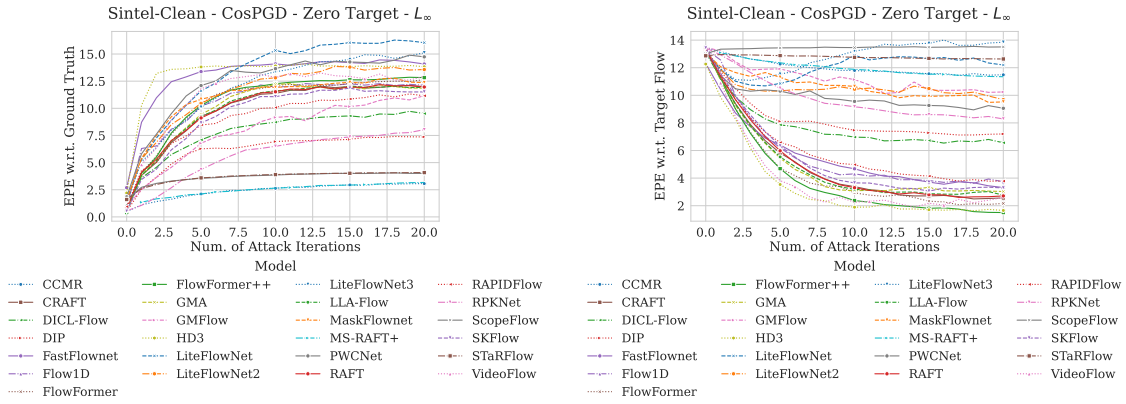

Figure 60: Evaluations for targeted CosPGD attack with target $\overrightarrow{0}$ under ℓ_∞-norm bound using the MPI Sintel (clean) dataset. The attack was optimized w.r.t. the ground truth predictions.

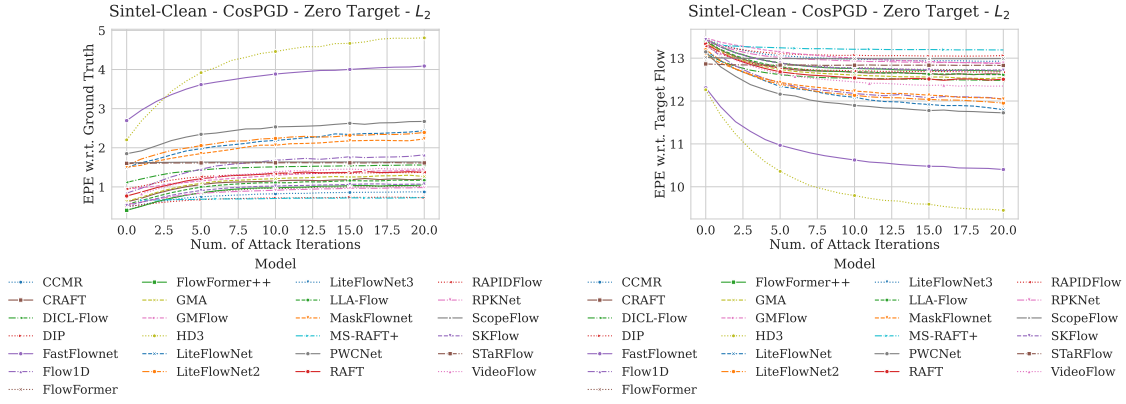

Figure 61: Evaluations for targeted CosPGD attack with target $\overrightarrow{0}$ under ℓ_2-norm bound using the MPI Sintel (clean) dataset. The attack was optimized w.r.t. the ground truth predictions.

to make the numbers and column headings better visible to the users, and the users can dynamically rank these based on any of the columns. We will host the website after acceptance.

J Limitations

Benchmarking optical flow estimation methods is a computationally and labor-intensive endeavor. Thus, best utilizing available resources, we use FlowBench to benchmark a limited number of settings. The benchmarking tool itself offers significantly more combinations that can be benchmarked. Nonetheless, the benchmark provided is comprehensive and instills interest to further utilizing FlowBench.

K Reproducibility Of Evaluations

There always exists stochasticity when evaluating adversarial attacks, due to the randomness these attacks exploit, and also common corruptions due to variations in seeds and calculation approximations made by various python libraries. Therefore, for transparency and reproducibility, we evaluate different runs on the same seed and different runs of different seeds. We report these evaluations here, using Tab. 5 for adversarial attacks and Tab. 6 for common corruptions, and observe that the variance is extremely low and the analysis performed in this work still stands.

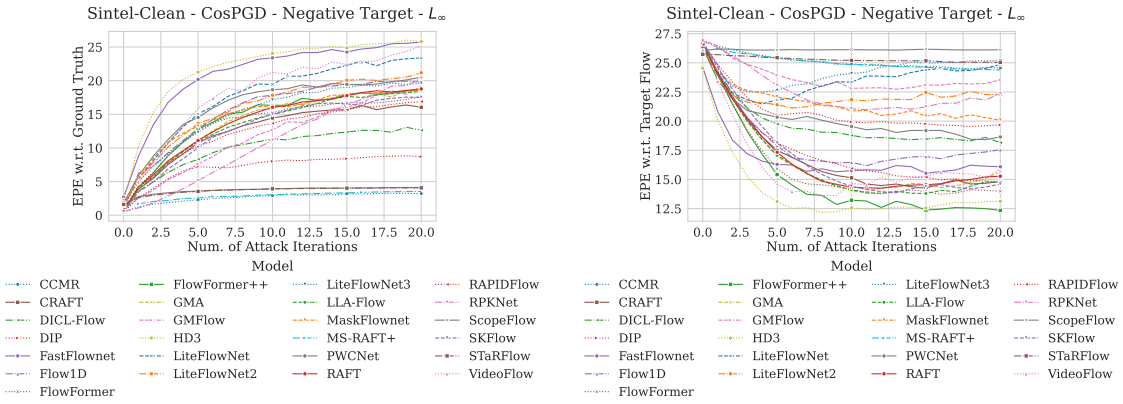

Figure 62: Evaluations for targeted CosPGD attack with target $\overrightarrow{-f}$ under ℓ_∞-norm bound using the MPI Sintel (clean) dataset. The attack was optimized w.r.t. the ground truth predictions.

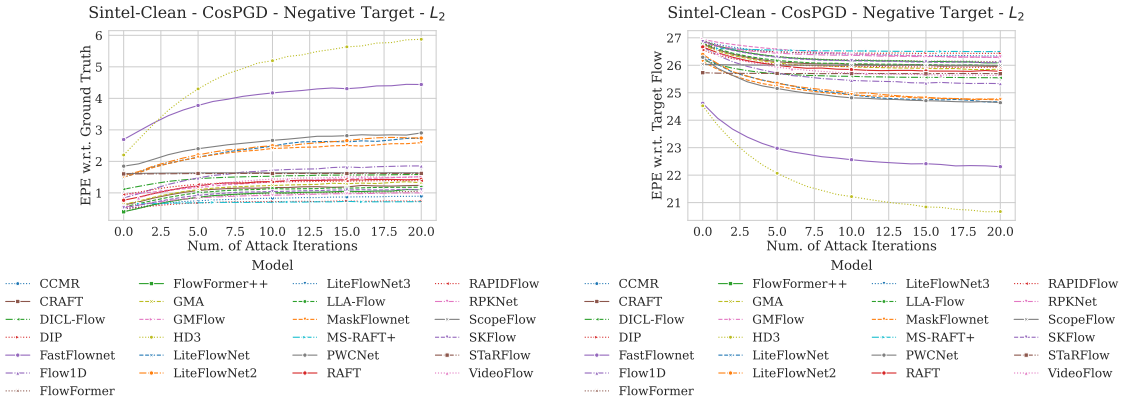

Figure 63: Evaluations for targeted CosPGD attack with target $\overrightarrow{-f}$ under ℓ_2-norm bound using the MPI Sintel (clean) dataset. The attack was optimized w.r.t. the ground truth predictions.

To ensure the reproducibility of our adversarial attack evaluations we repeat experiments in two ways: first, three different runs with the same seed, and second, one run each for three different seeds. We observe very minute variations in results in both cases which can be attributed to calculation approximations made by different libraries such as pytorch (Paszke et al., 2019). Due to the compute-hungry nature of these evaluations, we limit them to using one method: RAFT on the KITTI2015 dataset, and the attack used is CosPGD. We evaluate multiple settings: different ℓ_p-norm bounds, different attack optimization methods (optimizing w.r.t. ground truth flow and optimizing w.r.t. initial flow prediction.), and for targeted attacks, two different targets. The attack settings are consistent with the paper.

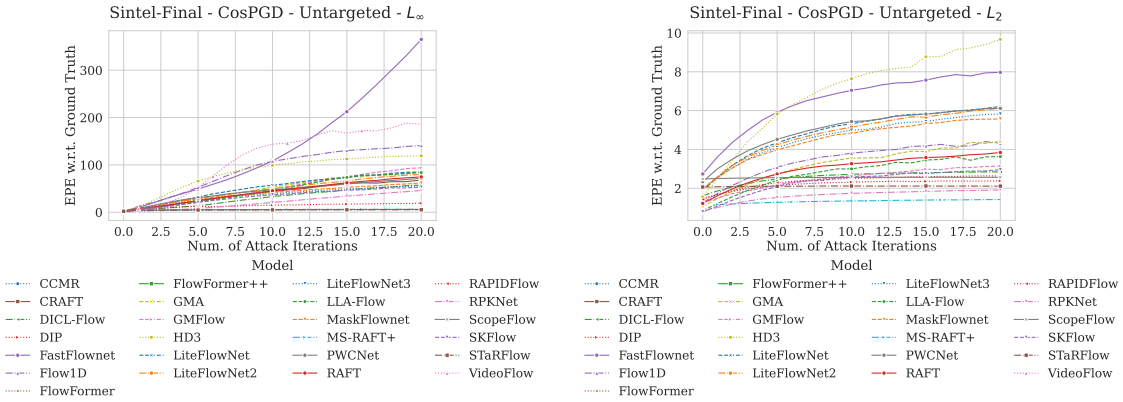

Figure 64: Evaluations for non-targeted CosPGD attack under ℓ_∞-norm bound using the MPI Sintel (final) dataset. The attack was optimized w.r.t. the ground truth predictions.

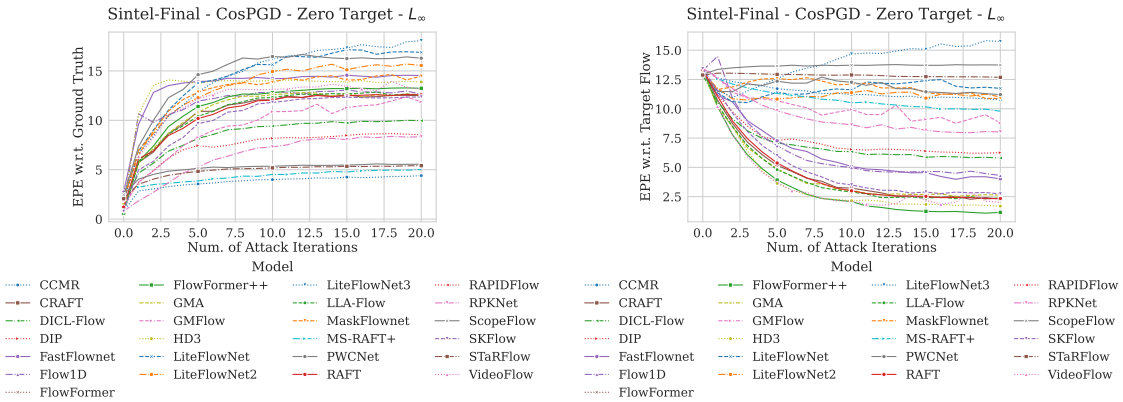

Figure 65: Evaluations for targeted CosPGD attack with target $\overrightarrow{0}$ under ℓ_∞-norm bound using the MPI Sintel (final) dataset. The attack was optimized w.r.t. the ground truth predictions.

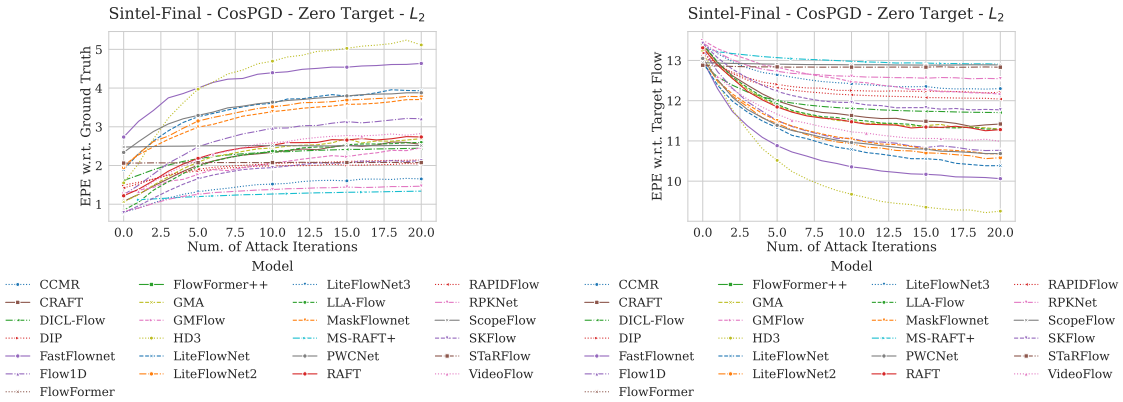

Figure 66: Evaluations for targeted CosPGD attack with target $\overrightarrow{0}$ under ℓ_2-norm bound using the MPI Sintel (final) dataset. The attack was optimized w.r.t. the ground truth predictions.

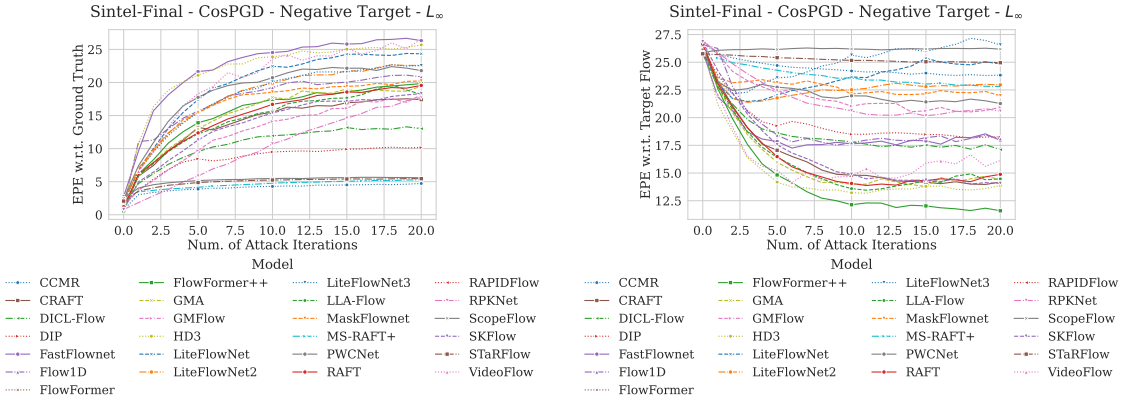

Figure 67: Evaluations for targeted CosPGD attack with target $\overrightarrow{-f}$ under ℓ_∞-norm bound using the MPI Sintel (final) dataset. The attack was optimized w.r.t. the ground truth predictions.

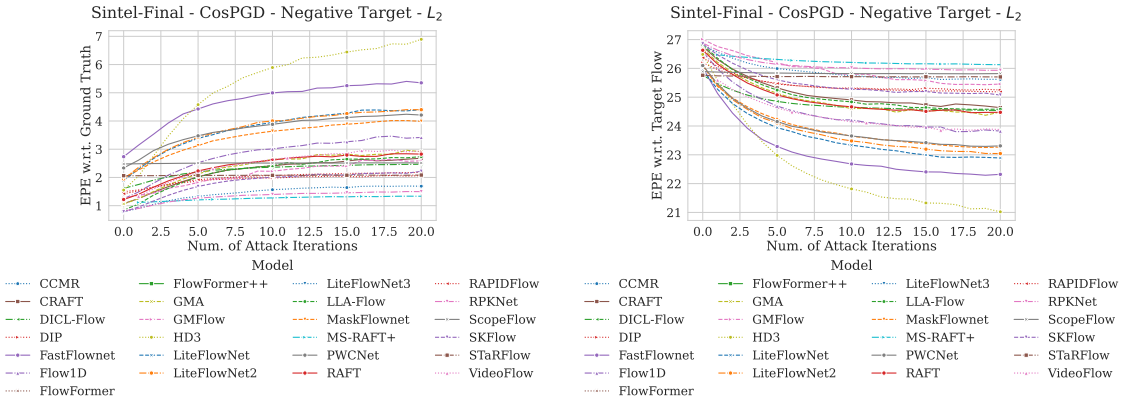

Figure 68: Evaluations for targeted CosPGD attack with target $\overrightarrow{-f}$ under ℓ_2-norm bound using the MPI Sintel (final) dataset. The attack was optimized w.r.t. the ground truth predictions.

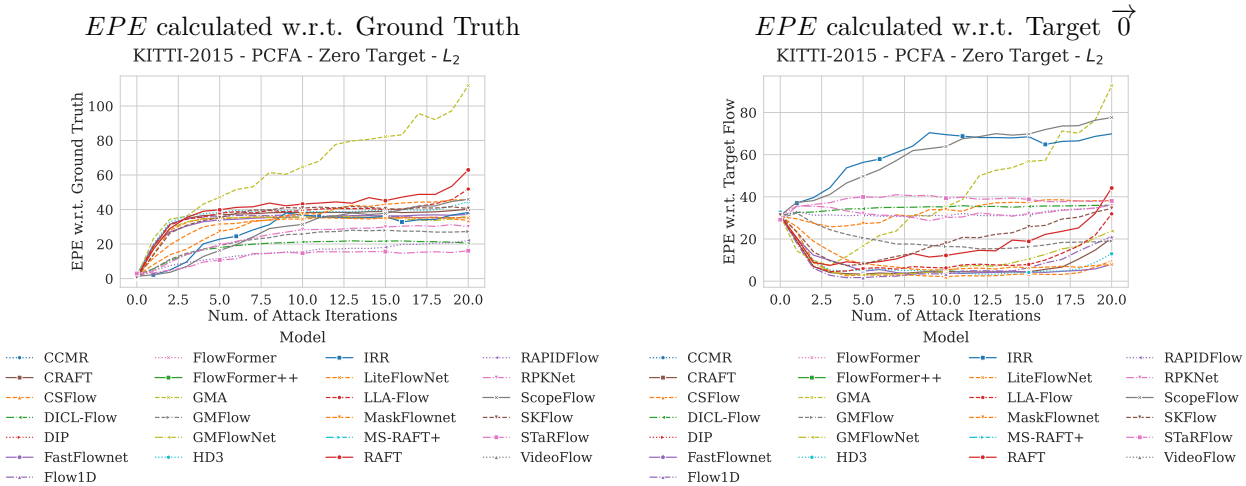

Figure 69: Evaluating all optical flow estimation methods against PCFA attack with target $\overrightarrow{0}$ over multiple attack iterations.

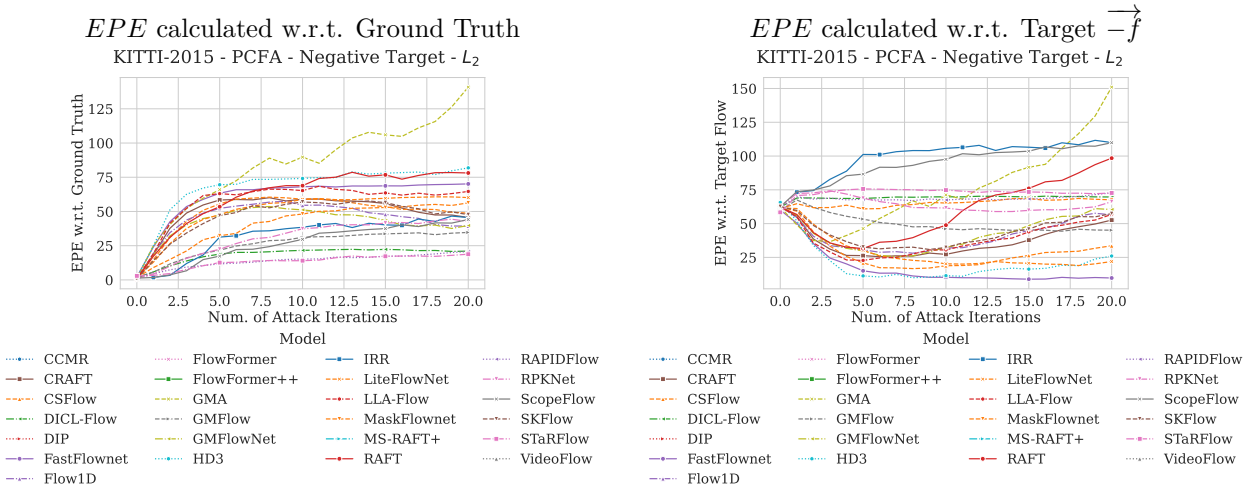

Figure 70: Evaluating all optical flow estimation methods against PCFA attack with target $-\overrightarrow{f}$ over multiple attack iterations.

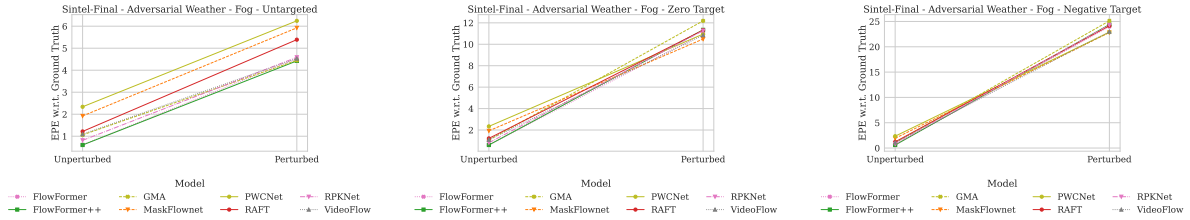

Figure 71: Evaluations for Adversarial Weather attack with Fog optimized as an non-targeted attack (left), and targeted attack with targets $\overrightarrow{0}$ (center) and $-\overrightarrow{f}$ (right).

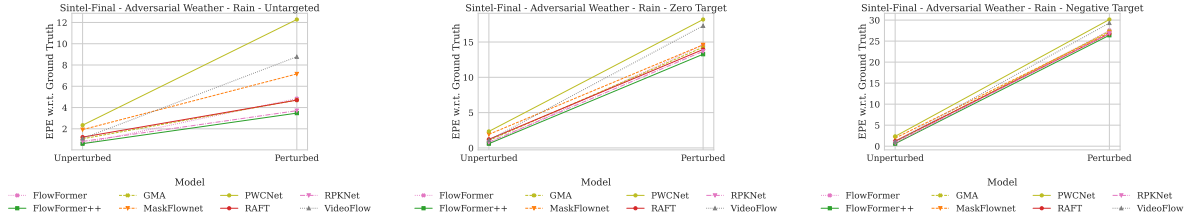

Figure 72: Evaluations for Adversarial Weather attack with Rain optimized as an non-targeted attack (left), and targeted attack with targets $\overrightarrow{0}$ (center) and $-\overrightarrow{f}$ (right).

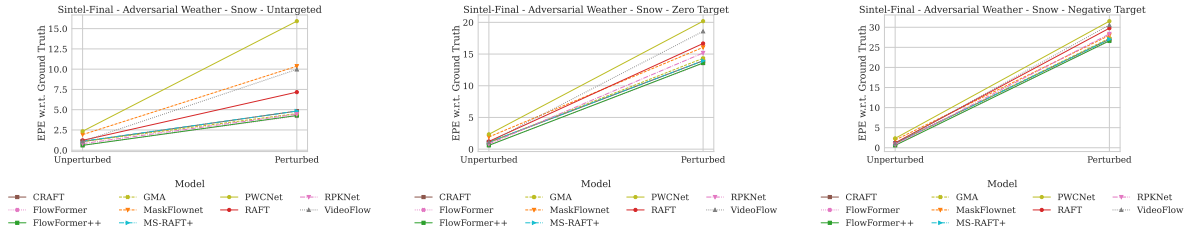

Figure 73: Evaluations for Adversarial Weather attack with Snow optimized as an non-targeted attack (left), and targeted attack with targets $\overrightarrow{0}$ (center) and $-\overrightarrow{f}$ (right).

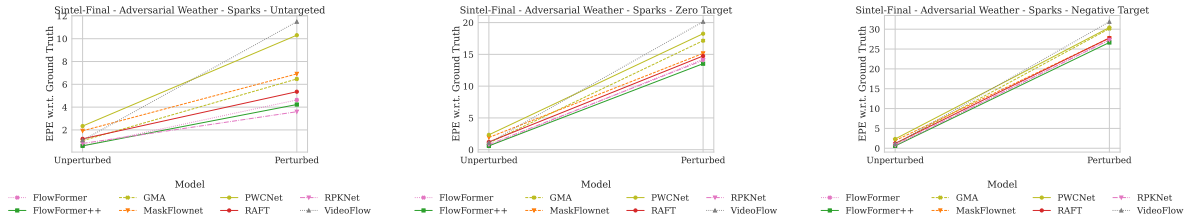

Figure 74: Evaluations for Adversarial Weather attack with Sparks optimized as an non-targeted attack (left), and targeted attack with targets $\overrightarrow{0}$ (center) and $-\overrightarrow{f}$ (right).

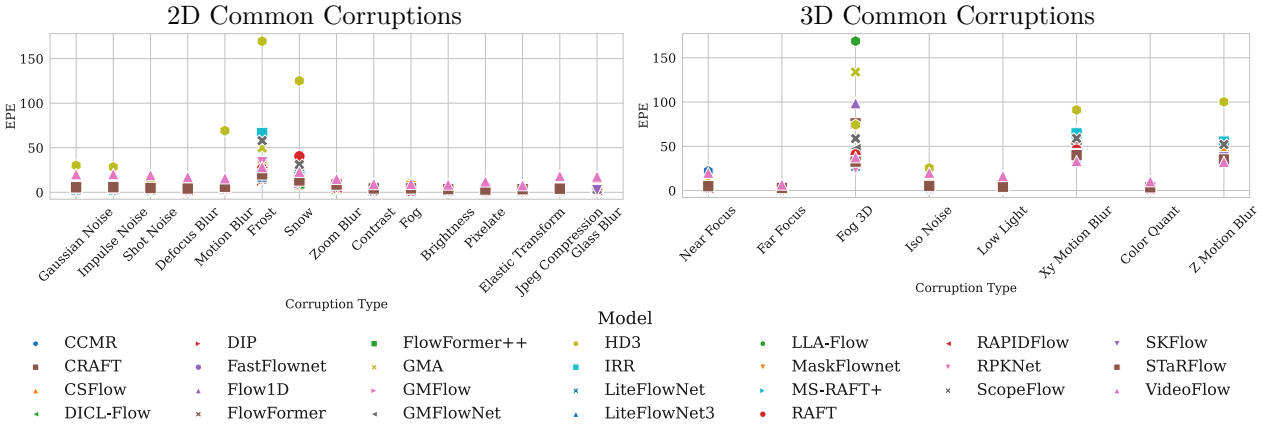

Figure 75: Performance of various optical flow estimation methods after corruptions on the KITTI2015 dataset.

Table 4: We report the mean EPE of the baseline method RAFT Teed & Deng (2020) and RAFT trained in a semi-supervised way using Flow Supervisor Im et al. (2022) and RAFT trained in a self-supervised way using AutoFlow Huang et al. (2023), and finally RAFT trained using AutoFlow and then finetuned on the KITTI2015 training dataset as 'AutoFlow Finetuned'.

2D Common Corruptions	**RAFT** Teed & Deng (2020)	**Flow Supervisor** Im et al. (2022)	**AutoFlow Pretrained** Huang et al. (2023)	**AutoFlow Finetuned** Huang et al. (2023)
Gaussian Noise	6.02	4.10	2.16	2.35
Shot Noise	4.17	2.85	2.18	2.36
Impulse Noise	6.07	3.70	2.15	2.36
Defocus Blur	2.02	2.02	2.27	2.40
Glass Blur	2.39	2.16	2.23	2.36
Motion Blur	4.08	3.92	2.29	2.43
Zoom BLur	4.81	4.74	2.20	2.38
Snow	40.42	53.31	1.82	2.60
Frost	26.51	95.53	1.93	3.04
Fog	1.22	2.99	2.28	2.43
Brightness	1.24	2.60	2.26	2.43
Contrast	1.19	1.22	2.28	2.43
Elastic Transform	1.05	1.13	2.29	2.44
Pixelate	0.79	0.86	2.28	2.44
JPEG Compression	1.94	1.89	2.13	2.41
mean Corruptions	6.93	12.20	2.18	2.46
Clean	0.64	0.73	2.29	2.44

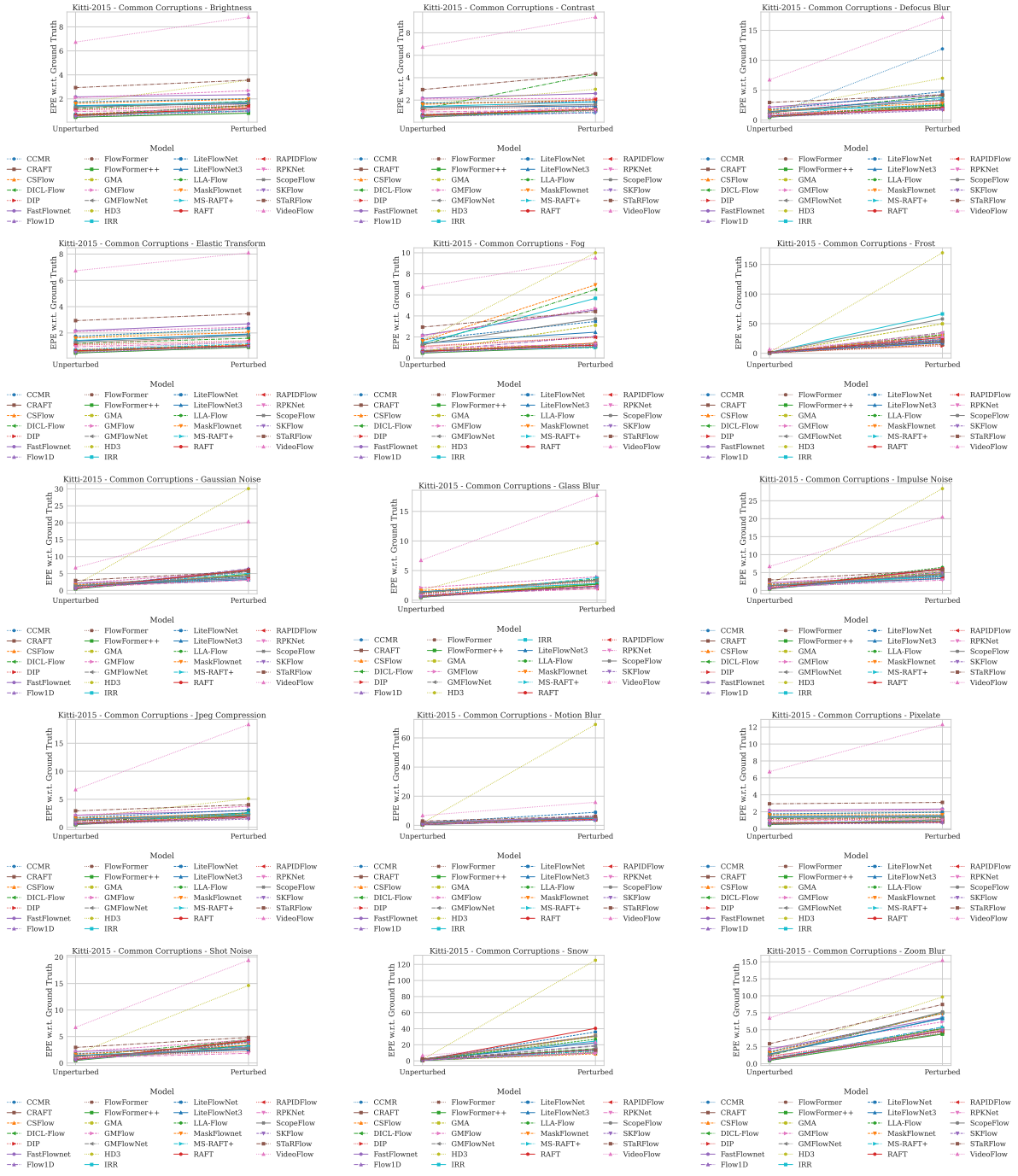

Figure 76: Evaluating optical flow estimation methods against all 2D Common Corruptions on the KITTI2015 dataset.

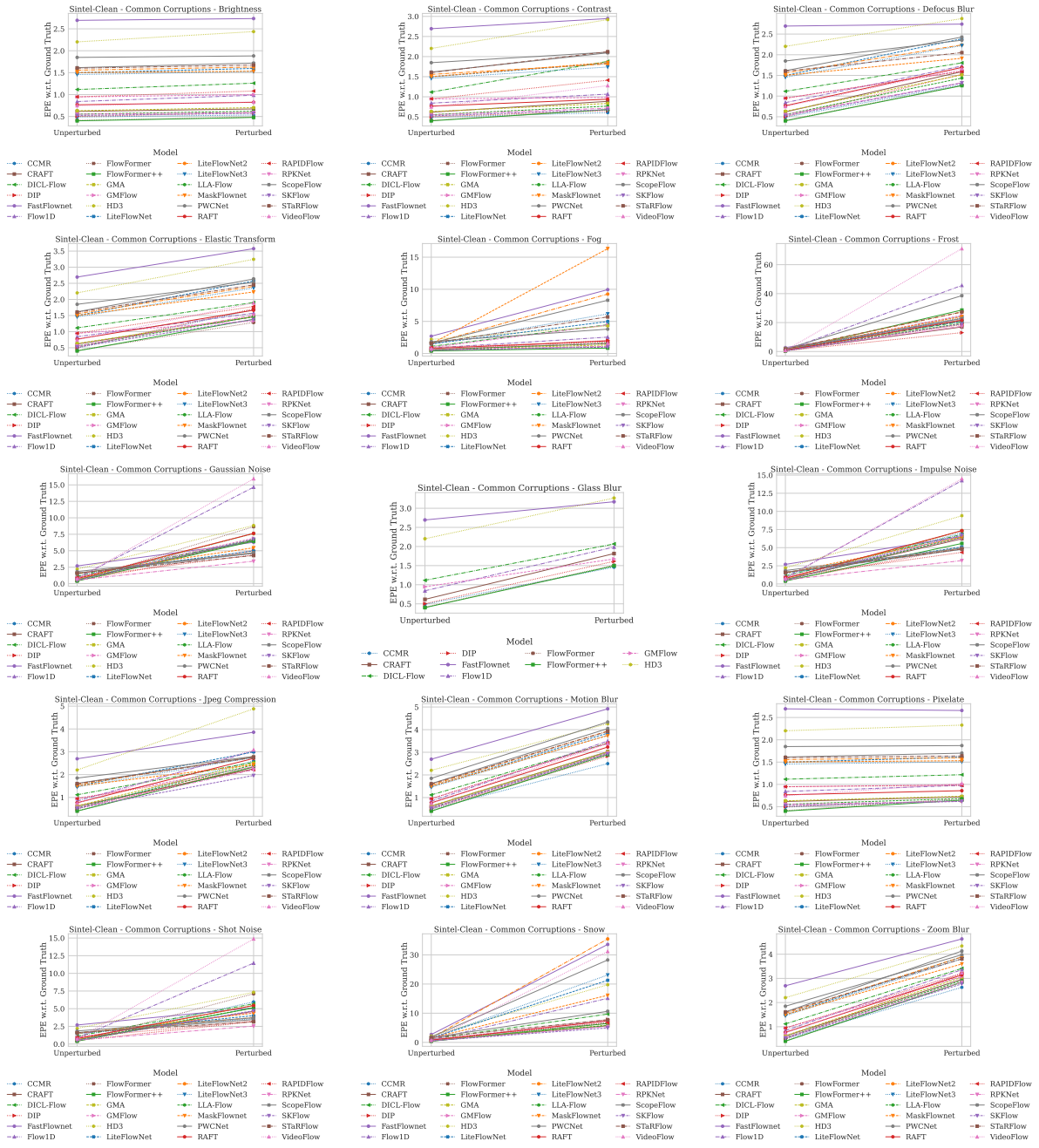

Figure 77: Evaluating optical flow estimation methods against all 2D Common Corruptions on the MPI Sintel (clean) dataset.

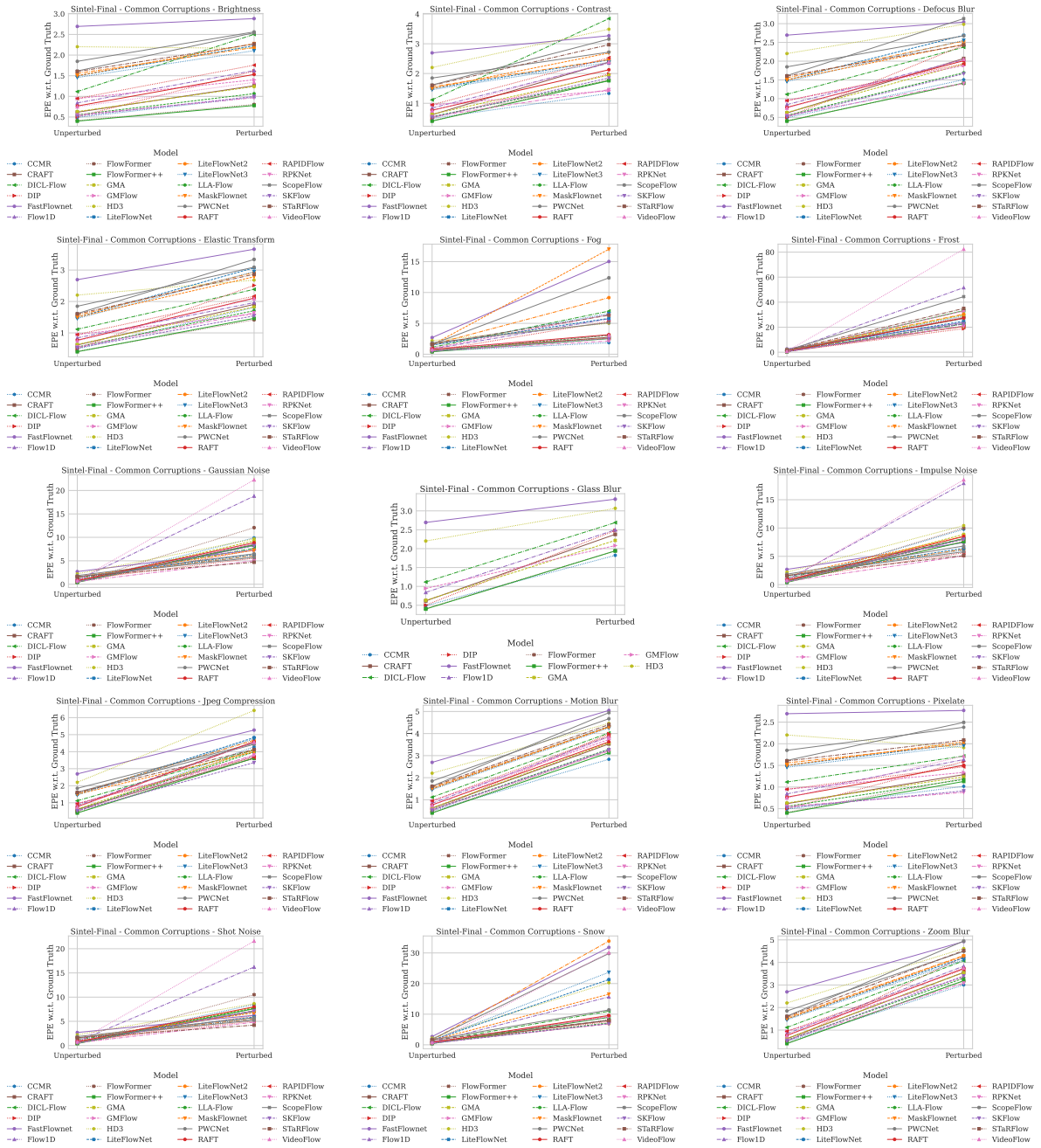

Figure 78: Evaluating optical flow estimation methods against all 2D Common Corruptions on the MPI Sintel (final) dataset.

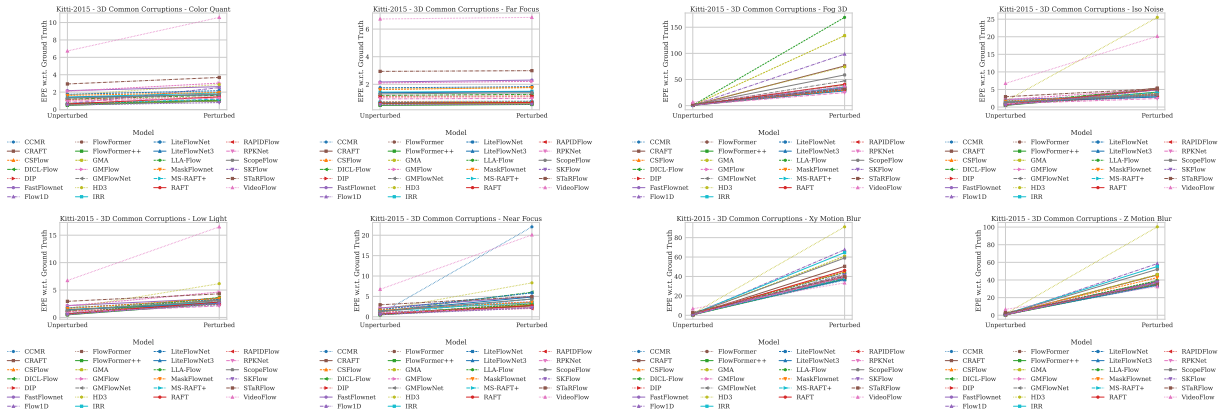

Figure 79: Evaluating optical flow estimation methods against the considered 3D Common Corruptions on the KITTI2015 dataset.

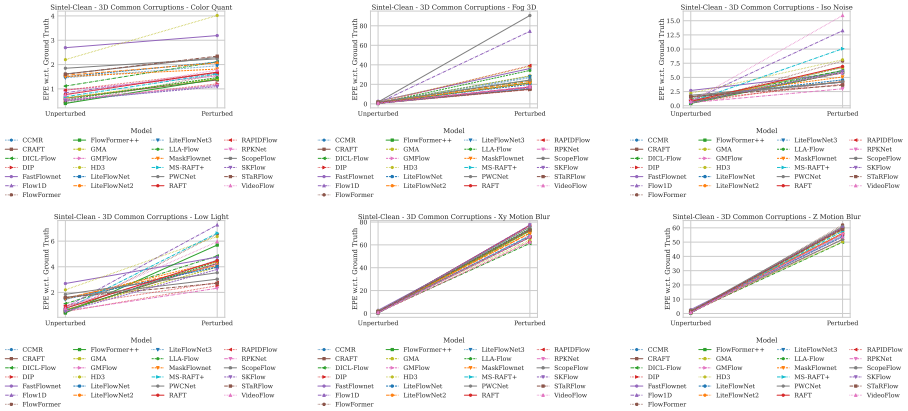

Figure 80: Evaluating optical flow estimation methods against the considered 3D Common Corruptions on the MPI Sintel (clean) dataset.

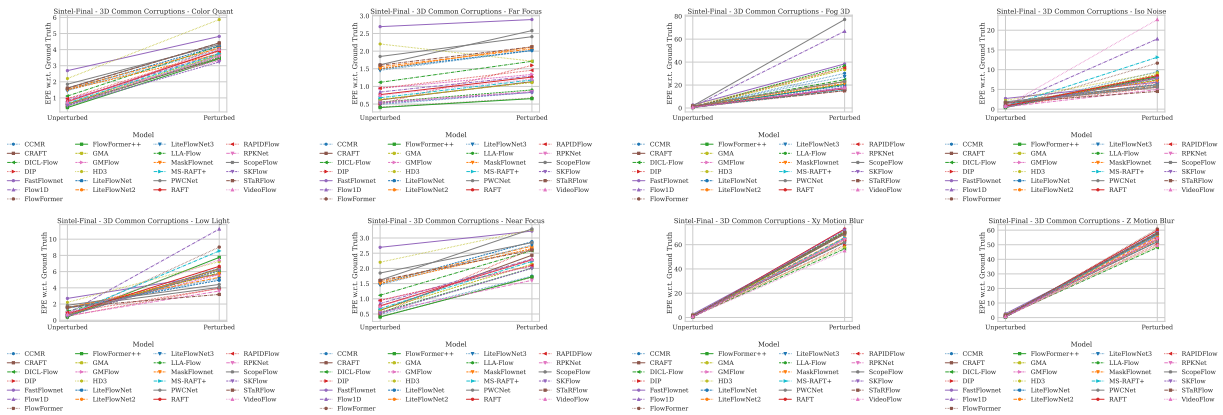

Figure 81: Evaluating optical flow estimation methods against the considered 3D Common Corruptions on the MPI Sintel (final) dataset.

FlowBench

Optical flow estimation is a crucial computer vision task often applied to safety critical real-world scenarios like autonomous driving and medical imaging. While optical flow estimation accuracy has greatly benefited from the emergence of Deep learning, learning-based methods are also known for their lack of generalization and reliability. However, reliability is paramount when optical flow methods are employed in the real world, where safety is essential. Furthermore, a deeper understanding of the robustness and reliability of learning-based optical flow estimation methods is still lacking, hindering the research community from building methods safe for real-world deployment. Thus we propose FLOWBENCH, a robustness benchmark and evaluation tool for learning-based optical flow methods. FLOWBENCH facilitates streamlined research into the reliability of optical flow methods by benchmarking their robustness to adversarial attacks and out-of-distribution samples. With FLOWBENCH, we benchmark 91 methods across 3 different datasets under 7 diverse adversarial attacks and 23 established common corruptions, making it the most comprehensive robustness analysis of optical flow methods to date. Across this wide range of methods, we consistently find that methods with state-of-the-art performance on established standard benchmarks lack reliability and generalization ability. Moreover, we find interesting correlations between performance, reliability, and generalization ability of optical flow estimation methods, under various lenses such as design choices used, number of parameters, etc. After acceptance, FLOWBENCH will be open-source and publicly available, including the weights of all tested models.

Show rows: 5 **Dataset:** KITTI2015

Leaderboard: Optical Flow Estimation

Rank	Architecture	CosPGD-EPE No...	PCFA-EPE target...	PGD-EPE Non-ta...	Checkpoint	Time_Proposed
1	IRR_PWC	2.4330115861	69.8680467474	3.8397940102	KITTI	Mar 2020
2	ScopeFlow	2.6299911237	77.6024067444	4.5666427672	KITTI	Nov 2023
3	MS-RAFT+	2.695769617	40.9803659793	5.0118829945	KITTI	Jul 2020
4	StarFlow	4.1756131017	38.06560606	5.4629693043	KITTI	Mar 2024
5	DICL	10.5310789597	35.9340447974	21.0924557686	KITTI	Jul 2021

Figure 82: A share a screenshot from our prototype website currently under works, that would help better understand the metrics. In this screenshot, the methods are ranked based on their EPE w.r.t. the ground truth flow under non-targeted CosPGD attack at 20 attack iterations under the ℓ_∞-norm bound (lower means the method is more robust) evaluated using the KITTI2015 dataset. We are currently designing it to make the numbers and column headings better visible to the users, and the users can dynamically rank these based on any of the columns.

Table 5: To ensure the reproducibility of our adversarial attack evaluations we repeat experiments in two ways: first, three different runs with the same seed, and second, one run each for three different seeds. We observe very minute variations in results in both cases which can be attributed to calculation approximations made by different libraries such as pytorch (Paszke et al., 2019). Due to the compute-hungry nature of these evaluations, we limit them to using one method: RAFT on the KITTI2015 dataset, and the attack used is CosPGD. We evaluate multiple settings: different ℓ_p-norm bounds, different attack optimization methods (optimizing w.r.t. ground truth flow and optimizing w.r.t. initial flow prediction.), and for targeted attacks, two different targets. The attack settings are consistent with the paper. Target 'None' means the attack was Non-targeted.

ℓ_p-norm bound	Target	Attack Optimized w.r.t.	EPE mean ± std	px3 error mean ± std
Three different runs on the same seed				
ℓ_∞-norm	None	Ground Truth Flow	119.504 ± 2.95E+0	0.078 ± 6.76E-3
ℓ_∞-norm	$-\overrightarrow{f}$	Ground Truth Flow	45.357 ± 4.26E-1	0.200 ± 7.84E-4
ℓ_∞-norm	$\overrightarrow{0}$	Ground Truth Flow	10.674 ± 2.74E-1	0.647 ± 1.06E-2
ℓ_2-norm	None	Ground Truth Flow	0.644 ± 2.72E-6	0.968 ± 3.38E-6
ℓ_2-norm	$-\overrightarrow{f}$	Ground Truth Flow	73.454 ± 3.12E-5	0.129 ± 2.86E-7
ℓ_2-norm	$\overrightarrow{0}$	Ground Truth Flow	36.724 ± 2.11E-5	0.170 ± 4.41E-7
ℓ_2-norm	None	Initial Flow Pred	0.643 ± 7.74E-6	0.968 ± 1.49E-6
One run each using three different seeds				
ℓ_∞-norm	None	Ground Truth Flow	119.692 ± 1.75E+0	0.077 ± 4.27E-3
ℓ_∞-norm	$-\overrightarrow{f}$	Ground Truth Flow	45.149 ± 9.16E-1	0.202 ± 1.65E-3
ℓ_∞-norm	$\overrightarrow{0}$	Ground Truth Flow	11.016 ± 4.91E-1	0.625 ± 9.90E-3
ℓ_2-norm	None	Ground Truth Flow	0.644 ± 7.46E-6	0.968 ± 6.05E-6
ℓ_2-norm	$-\overrightarrow{f}$	Ground Truth Flow	73.454 ± 1.15E-4	0.129 ± 1.85E-7
ℓ_2-norm	$\overrightarrow{0}$	Ground Truth Flow	36.724 ± 1.10E-4	0.170 ± 7.92E-7
ℓ_2-norm	None	Initial Flow Pred	0.643 ± 1.44E-4	0.968 ± 1.55E-5

Table 6: To ensure reproducibility of our Common Corruptions evaluations we repeat experiments in two ways: first, three different runs with the same seed, and second, one run each for three different seeds. We observe extremely minute variations in results which can be attributed to differences in seeds and calculation approximations made by the Python libraries. Due to the compute-hungry nature of these evaluations, we limit them to using one method: RAFT on the KITTI2015 dataset, and all the fifteen 2D Common Corruptions.

2D Common Corruption Name	EPE mean ± std	px3 error mean ± std
Three different runs on the same seed		
brightness	1.235 ± 0.000	0.935 ± 0.000
contrast	1.187 ± 0.000	0.938 ± 0.000
defocus blur	2.026 ± 0.000	0.899 ± 0.000
elastic transform	1.043 ± 0.000	0.954 ± 0.000
fog	1.221 ± 0.000	0.936 ± 0.000
frost	29.640 ± 0.000	0.383 ± 0.000
gaussian noise	5.931 ± 0.000	0.732 ± 0.000
glass blur	2.409 ± 0.000	0.861 ± 0.000
impulse noise	6.098 ± 0.220	0.736 ± 0.002
jpeg compression	1.942 ± 0.000	0.892 ± 0.000
motion blur	5.515 ± 0.000	0.549 ± 0.000
pixelate	0.785 ± 0.000	0.960 ± 0.000
shot noise	4.435 ± 0.000	0.780 ± 0.000
snow	41.974 ± 0.000	0.354 ± 0.000
zoom blur	4.808 ± 0.000	0.746 ± 0.000
One run each using three different seeds		
brightness	1.235 ± 0.000	0.935 ± 0.000
contrast	1.187 ± 0.000	0.938 ± 0.000
defocus blur	2.026 ± 0.000	0.899 ± 0.000
elastic transform	1.041 ± 0.009	0.953 ± 0.001
fog	1.282 ± 0.076	0.937 ± 0.001
frost	28.783 ± 0.827	0.391 ± 0.019
gaussian noise	5.877 ± 0.026	0.735 ± 0.001
glass blur	2.532 ± 0.105	0.859 ± 0.002
impulse noise	5.856 ± 0.067	0.737 ± 0.002
jpeg compression	1.942 ± 0.000	0.892 ± 0.000
motion blur	4.135 ± 0.141	0.565 ± 0.010
pixelate	0.785 ± 0.000	0.960 ± 0.000
shot noise	4.336 ± 0.143	0.781 ± 0.004
snow	42.984 ± 4.786	0.362 ± 0.007
zoom blur	4.808 ± 0.000	0.746 ± 0.000